Laser Induced Breakdown Spectroscopy for Microanalysis of Surfaces

by

Shyama Prasad Banerjee

A thesis submitted in partial fulfillment of the requirements for the degree of

Doctor of Philosophy

in

Photonics and Plasmas

Department of Electrical and Computer Engineering
University of Alberta

Abstract

The utilization of Laser Induced Breakdown Spectroscopy (LIBS) as a potential material characterization technique has been demonstrated through academic and industrial research in past. LIBS has been applied for lateral surface scanning of materials and in depth resolution analysis. The necessity of improving lateral and depth resolution has led to the the development of microLIBS, a regime using low energy microjoule laser pulses. Femtosecond lasers have advanced the technique by its ability to produce high finer micromachined features. The optimization of pulse energy, optics, detectors and experimental environments are required to obtain precise surface microanalysis using LIBS.

This thesis has been focused on a number of essential aspects of LIBS microanalysis. Laser ablation characteristics of materials depend on laser parameters and material properties. The single shot ablation threshold of chromium has been determined using UV femtosecond laser pulses and compared with two temperature model (TTM) predictions. The spatio-temporal evolution of the femtosecond laser induced micro-plasma plumes were characterized in the nanojoule ablation regime. The plume splitting, angular distribution of the plumes, plume lengths and plume images at threshold energies were characterized. Analytical models were used to compare plasma plume expansion and

propagation characteristics. A LIBS depth profiling technique has been studied together with deep blind hole drilling using femtosecond laser pulses. The material removal rates were measured and compared with analytical calculations. The depth sensitive region that contributes to the LIBS emission has been evaluated for a single shot depth profiling study. It has been demonstrated by experiment and TTM model calculations that the depth sensitive region is much smaller than the ablated crater depth. Thin chromium lines on silicon wafers were prepared and scanning microanalysis across these metal strips using UV femtosecond pulses were carried out. Lateral resolution of the order of a micron has been obtained using LIBS.

Preface

This thesis is an original work by Shyama Prasad Banerjee. All experiments were carried out at the University of Alberta under the guidance of Professor Robert Fedosejevs. The thesis introduction in Chapter 1, LIBS microanalysis review in Chapter 2, experimental methodologies in Chapter 3 and the conclusions in Chapter 9 were written by me and corrected by Prof. Fedosejevs.

Chapter 4 has been published as: S. P. Banerjee and R. Fedosejevs, "Single shot ablation threshold of chromium using UV femtosecond laser pulses," *Appl. Phys. A* DOI: 10.1007/s00339-014-8577-y (2014). I was responsible to design the experimental setup, carried out the experiment, analyzed the experimental data and prepared the manuscript. Professor Fedosejevs gave suggestions during the experiment, helped in interpreting the data and helped in modifying the manuscript.

Chapter 5 has been published as: S. P. Banerjee and R. Fedosejevs, "Single shot depth sensitivity using femtosecond Laser Induced Breakdown Spectroscopy," *Spectrochimica Acta Part B* 92, 34-41 (2014). I was responsible to design the experimental setup, carried out the experiment, analyzed the experimental data and prepared the manuscript. Professor Fedosejevs gave the idea of depth sensitivity in LIBS, guided during the experiment, helped in interpreting the data and helped in modifying the manuscript.

Chapter 6 has been published as: S. P. Banerjee, Z. Chen and R. Fedosejevs, "Femtosecond laser plasma plume characteristics in the nanojoule ablation regime," *J Appl. Phys.* 113, 183101 (2014). I was responsible to design the experimental setup, carried out the experiment, analyzed the experimental data and prepared the manuscript. Zhijiang Chen helped me to carry out the experiment. Professor Fedosejevs gave suggestions during the experiment, helped in interpreting the data and helped in modifying the manuscript.

Chapter 7 has been published as: S. P. Banerjee, Z. Chen, I. Utkin and R. Fedosejevs, "Detection of buried layers in silicon devices using LIBS during hole drilling with femtosecond laser pulses," *Appl. Phys. A* 111, 791-798 (2013). I was responsible to design the experimental setup, carried out the experiment, analyzed the experimental data and prepared the manuscript. Zhijiang Chen and Dr. Ilya Utkin have helped me to carry out the experiment. Professor Fedosejevs proposed the idea of this project, gave suggestions during the experiment, helped in interpreting the data and helped in modifying the manuscript.

Chapter 8 has been submitted to: S. P. Banerjee, Z. Chen and R. Fedosejevs, "High resolution scanning microanalysis on material surfaces using UV femtosecond Laser Induced Breakdown Spectroscopy," *Opt. Laser Eng.* (2014). I was responsible to design the experimental setup, carried out the experiment, analyzed the experimental data and prepared the manuscript. Zhijiang Chen helped me to carry out the experiment. Professor Fedosejevs gave the core idea about this project, gave suggestions during the experiment, helped in interpreting the data and helped in modifying the manuscript.

To my family

Acknowledgements

The thesis was only possible due to the invaluable contribution of many people around me. I would like to thank Prof. Fedosejevs for offering me the opportunity to work under his supervision and guiding me with his sparkling ideas throughout the entire course of this study. His impressive command over different research areas amazes me. I wish to thank Dr. Tsui for several discussions and for lending me the 40x objective which was very helpful. I appreciate the technical help I received from Blair Harwood. I am thankful to Dr. Ilya Utkin, Dr. Henry Tiedje and Dr. Sanjay Singh for their support in different phases of my research. The company of Dr. Yogesh Godwal was always filled with informative discussions from global events. I am grateful to Mike Taschuk for his help during the initial LIBS experiments. My sincere thanks to Zhijiang Chen for assisting me in various experiments. He is a smart researcher. Thanks to lab mates, especially Archana, Atif, Chin-Kuei, Mianzhen, Raj, Rezwana, Travis, Zia, Zahurul and all the rest for their enthusiastic support. I thank all my friends who eventually have been associated as our extended family in Edmonton. This thesis might have been faster without those never ending sumptuous potlucks, but certainly would have been less entertaining. I am also thankful to all my friends in IPR.

This long journey would not have been possible without the unconditional support of my family. I would like to express my heartiest gratitude to my father for his endless support and my mother who has been my greatest inspiration throughout my life. My special thanks go to my brother, sisters and all other family members especially my in-laws for their love and selfless support. Finally, I would like to thank my pillar of strength, my lovely wife, Barnali. Her love, sacrifice, understanding, patience, eternal support and our bundle of joy, our little princess Aheli, have made this thesis possible.

Contents

List of Tables

List of Figures

Abbreviations

AAR	Average Ablation Rate
AFM	Atomic force microscope
APD	Avalanche Photodiode
CCD	Charge Coupled Device
fs	femtosecond (10^{-15} of a second)
FWHM	Full width at half maximum
HAZ	Heat Affected Zone
ICCD	Intensified Charge Coupled Device
ICP-AES	Inductively Coupled Plasma - Atomic Emission Spectroscopy
ICP-MS	Inductively Coupled Plasma Mass Spectroscopy
LIBS	Laser Induced Breakdown Spectroscopy
LOD	Limit Of Detection
LTE	Local Thermodynamic Equillibrium
MCP	Microchannel Plate
MEMS	Micro Electro Mechanical Structure
PDA	Photodiode Array
PMT	Photomultiplier Tube
ppb	parts per billion
ppm	parts per million
ps	picosecond (10^{-12} of a second)
RMS	Root Mean Square
RSD	Relative Standard Deviation
SEM	Scanning Electron Microscope
SNR	Signal to Noise Ratio
Srad	Steradian
TTM	Two Temperature Model

Symbols

C_e	Electron heat capacity
C_l	Ion heat capacity
e	Unit charge of an electron
T_F	Fermi temperature
g	Electron-ion energy coupling constant
κ	Electron thermal conductivity
k_B	Boltzmann constant
m_e	Electron mass
n_e	Electron density
T_e	Electron temperature
T_l	Lattice temperature
ϕ_{th}	Ablation threshold energy fluence
ω_p	Plasma frequency

Chapter 1

Introduction

Lasers are an integral part of numerous applications in today's technology including science, medicine, commercial industry, information technology, electronics, communication, entertainment and in the military. The ability of laser pulses to create a laser induced plasma when focusing the light on materials provides an avenue to characterize materials by utilizing the light emission from the laser-matter interaction. The element specific emission of optical radiation gives unique spectroscopic signatures of the atoms and ions present. Thus the emission from the laser created plasma leads to the possibility for spectrochemical analysis of materials. The combination of both laser radiation and spectroscopic techniques such as Raman Spectroscopy (RS), Laser Absorption Spectroscopy (LAS), Laser Induced Fluorescence (LIF) and Laser Induced Breakdown Spectroscopy (LIBS) provides multiple techniques to identify elemental characteristics of materials. Material modification and characterization by lasers has become an increasingly useful technique for high technology manufacturing as well as analytical and medical applications.

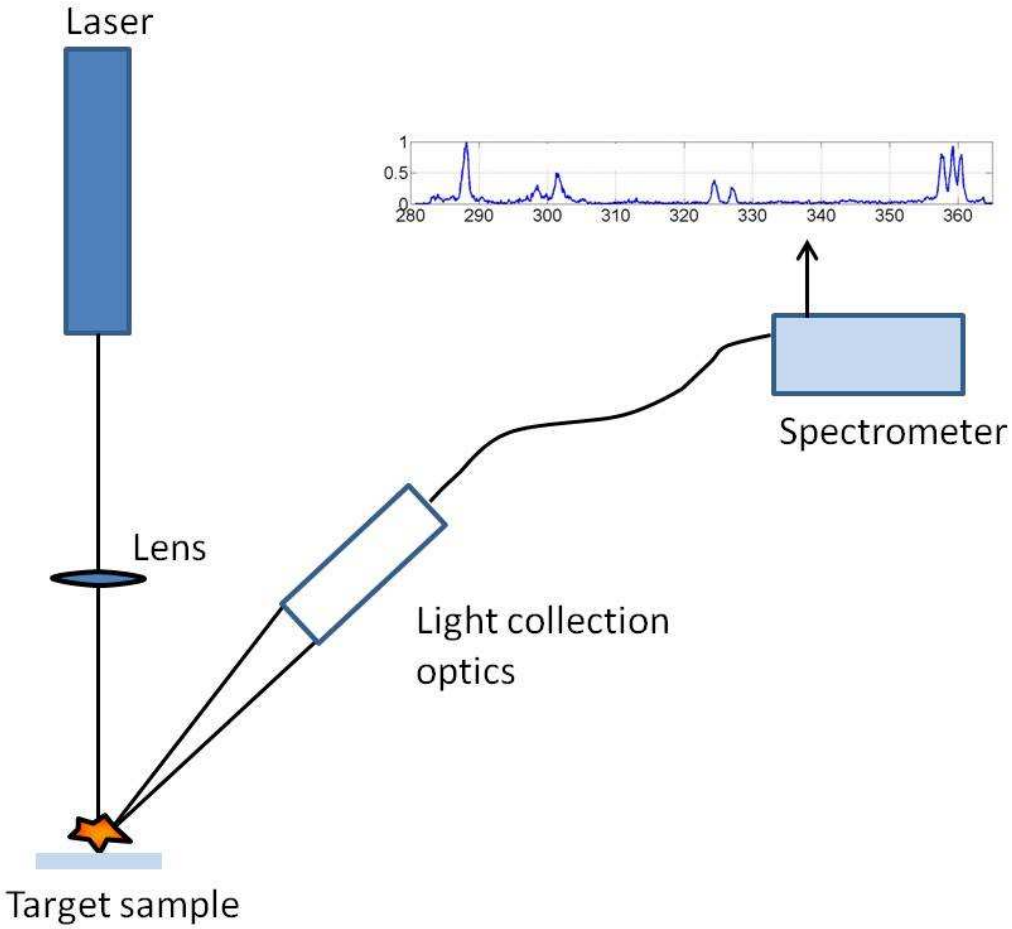

Figure 1.1: Schematic of a simple LIBS setup

1.1 LIBS Technique

LIBS [1, 2, 3, 4] employs short laser pulses to ablate a small amount of material and measure the characteristic line emission of the excited atoms and ions in the ablation plume in order to determine the atomic constituents of the target material. LIBS is also called as Laser Induced Plasma Spectroscopy (LIPS) or Laser Spark Spectroscopy (LSS). The target sample material can be in any physical state such as solid, liquid, gas, aerosol etc. A schematic diagram illustrating the LIBS process is shown in Fig. 1.1. Focused laser pulses with energy fluence above the ablation threshold create a micro-plasma on the target sample surface. The plasma plume expands in the background

gas and cools down in time. The recombination of electrons and ions during the plasma cooling process results in emission of light with spectral information of the target composition. Analysis of the obtained spectra reveals material properties. LIBS provides real time response and simultaneous multi element detection. Details of the laser plasma interaction and the processes behind LIBS are described in the next chapter.

The simplicity of LIBS makes it one of the appealing techniques in the domain of material analysis. The advantages of LIBS in comparison to other existing characterization techniques are

- **Limited or no sample preparation** : Measurements can be done without pre treatment of the target sample.

- **Applicable under different environments** : This technique can be applied under different background environments such as at different background pressures, inside water [5] and even in the extraterrestrial Mars environment where the ChemCam LIBS instrument was integrated with the NASA Mars Science Laboratory (MSL) rover 'Curiosity' [6].

- **Almost non destructive** : Spatial localization of the laser plasma provides sampling capability confined to tiny points on of the sample surface. A small amount of material is consumed during this process which makes the technique minimally-destructive and in many cases can be considered non-destructive.

- **Fast measurement speed** : Reliable measurements within a short time scale of the order of a fraction of a second.

- **Universal material sampling** : Useful for solid, liquid or gaseous samples. Laser parameters can be adjusted to produce laser induced breakdown of any sample.

- **Simultaneous detection** : Detection of multiple elements in a matrix of materials can be done within a single measurement.

- **Portability** : Essential components of a LIBS system can be made in a portable format which is one of the important advantages over other techniques.

- **Non contact stand off operation** : As this is entirely an optical technique, therefore it requires only optical access to the specimen. Remote, non-contact features of this technique can be used to build stand-off material analysis system when coupled to appropriate telescopic apparatus. These attributes have significance for use in various areas from hazardous environments such as nuclear reactors to space exploration as demonstrated by ChemCam on Mars.

This technique has been employed in numerous applications including industrial processes, environmental chemistry, biology, and cultural heritage. Applications of LIBS are summarized in Table 1.1.

Despite being one of the fastest tools for micro characterization of materials, LIBS applications are somewhat limited to date due to limits on achievable limit of detection (LOD) and somewhat poor reproducibility in different environments. The concept of limit of detection refers to the extent to which an analytical technique may detect the presence of a particular analyte in a background matrix. In general, LOD's using the LIBS technique falls in the range of parts per million (ppm) [1], whereas other established analytical techniques such as ICP-MS gives precise measurements of the order of parts per billion (ppb) [28] in most cases. The other interferences for quantitative LIBS measurements are self-absorption and matrix effects. Self-absorption occurs when the emission from the hotter region is absorbed by comparatively cooler atoms surrounding the high-temperature core of the laser plasma. The physical and chemical properties of samples with a matrix of materials can significantly af-

Field	Applications
Physical analysis	Determination of electron number density [7], temperature [7]
Spectro-chemical analysis	Surface mapping, resolution [8, 9]
	Depth profiling [10]
	LIBS imaging [11]
Environment	Air pollution [12, 13]
	Contaminants in water/soil [14]
	Industrial waste characterization [15]
Biological	Bacteria detection [16]
	biomedical applications [17, 18]
	food samples [19]
Security	Fingerprint mapping [20]
	Detection of chemical & biological threat [21]
	Forensic applications [22]
Archeological	Artworks characterization [23]
	Laser cleaning [24]
Industrial	Online process monitoring [25]
	Quality control [26]
	Coating thickness characterization [27]
Extraterrestrial	Material characterization in extraterrestrial environment [6]

Table 1.1: Applications of LIBS

fect the ablation dynamics, the plasma composition, the plasma temperature and in turn, the LIBS signal. This is known as the matrix effect. In spite of these, there are few competitors for LIBS when rapid microanalysis of metallic or non-metallic surfaces or depth profiling is the primary concern.

1.2 Thesis Overview

One of the important frontiers for LIBS is the application in the analysis of inhomogeneous mixtures of materials both laterally and in depth profiling. Micromachining of materials is a complimentary process which occurs when LIBS is carried out for microanalysis of material surfaces. The understanding of ab-

lation energy threshold of materials is required for microanalysis as the onset of the material ablation is the first step to creation of a plasma plume and optical emission from excited states. Femtosecond lasers with μJ pulse energy have become a leading tool in micromachining and their use is expanding into analysis of spectroscopic emission and its use in surface microanalysis. The focus of this thesis is to explore and optimize the application of femtosecond LIBS for microanalysis of material surfaces. The sample materials used in this thesis were mostly thin metallic films prepared by sputtering technique. A femtosecond Ti:Sapphire laser was used as the excitation source. The optimization of laser parameters was required to attain specific surface analysis specifications. The reduction of wavelength and energy of laser pulses reduces the ablation feature size at the sample surface. The utilization of UV wavelengths and suitable high numerical aperture objectives creates conditions of micro-ablation but LIBS also requires excitation of sufficient light emission and a high efficiency light collection system. The emission behavior from the laser produced plasma depends on the plasma heating and expansion characteristics. Thus the study of the plasma plume in space and time gives an insight to the complex physical phenomena after short period of the laser-matter interaction.

This thesis investigates the essential aspects of LIBS microanalysis such as determining the single shot ablation threshold of materials, plasma plume characteristics, depth profiling and lateral resolution. We have introduced LIBS as a monitoring technique for deep hole drilling and detection of buried layers. We also established a new concept of 'depth sensitivity' in the LIBS ablation by single femtosecond pulses. Several new results in depth and lateral studies in LIBS are demonstrated. The outline of the thesis with a brief overview of each of the chapters is given below.

- **Chapter 2** : This chapter gives a background review of LIBS microanalysis. The key parameters that affect the LIBS process are discussed in detail. The basics of laser-matter interaction, laser ablation and the process

of temporal evolution of spectral line emission are described. Laser micromachining, importance of femtosecond pulses in micromachining and their applications are cited. The application of LIBS in depth profiling and lateral microanalysis and their current status are reported.

- **Chapter 3** : Experimental methodologies used such as calibration techniques, optical light collection techniques and signal analysis techniques are described.

- **Chapter 4** : The single shot ablation threshold for thin chromium film using UV, femtosecond laser pulses is measured and compared to theory using a two temperature model for ultrafast laser pulse heating of the material.

- **Chapter 5** : Depth profiling using LIBS is an established technique. However in this chapter it is demonstrated that the depth sensitive region which contributes to the LIBS emission from single shot spectra is much smaller than the full ablation crater depth. A quantitative measurement of depth sensitivity is carried out and a two temperature model is used to estimate the spatial distribution of lattice temperature with depth qualitatively explaining the results.

- **Chapter 6** : A detailed study is carried out on micro plasma plume expansion with few nanojoule UV femtosecond pulses under different background pressure conditions. The spatio-temporal behavior of the plume is captured in plasma images under different conditions. The plasma plume emission length is measured under different conditions and the lifetime of plasma plume in this nanoablation regime is determined. Plume expansion and propagation are described with several models and compared with experiments.

- **Chapter 7** : This chapter investigated smart micromachining by incor-

porating the LIBS technique in the process of deep blind hole drilling using femtosecond laser pulses. The detection of buried trace metal layers under a thick silicon cover is demonstrated and an access hole to the metal through semiconductor is created. The material removal efficiency and drilling rates are measured. An analytical calculation of ablation depth per pulse is compared with the experimentally obtained value.

- **Chapter 8** : Lateral resolution using LIBS is explored. The conventional technique of using the crater size as an indicator of spatial resolution is replaced by actually scanning across known metal strip widths while observing the LIBS emission. The effective resolution using the actual scanning technique is determined.

- **Chapter 9** : The final chapter summarizes the results together with concluding remarks. The contributions of the thesis are highlighted and suggestions for future research are presented.

Chapter 2

LIBS Microanalysis : a Review

This chapter explains the complex processes behind LIBS which includes the basics of laser-matter interaction, ablation mechanism and the corresponding emission of radiation. The components of LIBS and their role in determining the process behavior are described briefly. Precise microanalysis is closely related to precise laser micromachining. The capability of femtosecond laser pulses to achieve precision material microprocessing and analysis is discussed. Recent work on the use of LIBS for microanalysis is reviewed and new approaches in LIBS are discussed.

2.1 LIBS Process Parameters

The main components of a LIBS set-up, as illustrated in Fig. 1.1, are a pulsed laser source and a spectrometer with suitably designed optical systems (laser focusing and collecting plasma emission) together with electronic control components (trigger and delay generators). The experiments are often fully computer controlled. The laser pulse energy, wavelength and beam mode quality and the properties of the target material also affect the production and characteristics of the laser induced plasma.

2.1.1 Choice of Lasers

The laser is the key component which induces plasma at the target sample surface and the choice of lasers determines the features of the plasma. Three main parameters, i.e. pulse duration, wavelength and energy per pulse are important in this scenario. A general overview of the common types of lasers used in LIBS is shown in Table 2.1 and the effect of laser parameters are discussed in subsequent sections.

Laser type	Wavelength	Pulse duration	Pulse energy
CO_2	10.6 μm	200 ns	100 mJ
Nd:YAG	1064 nm	4-10 ns	0.1-3 mJ
XeCl excimer	308 nm	20-30 ns	$\sim 10^3$ mJ
Ti:Sapphire	800 nm	20-200 fs	~ 0.5 mJ

Table 2.1: Common lasers used in the LIBS application and typical pulse parameters

The energy absorption depends on the laser wavelength used. Absorption for most materials is typically higher at shorter wavelengths and thus the ablation threshold fluence is lower and the ablation rate higher as well [29]. Ma et al. [30] have investigated the effects of laser wavelengths (UV 355 nm and IR 1064 nm) on the expansion of laser-induced plasma into one-atmosphere background argon gas. Time and space-resolved emission spectroscopy was used as a diagnostics tool to obtain plasma parameters which determined higher electron density with UV radiation. The UV generated plasma is also characterized by narrower emission lines and less intense continuum at equivalent laser photon density in comparison with the situation encountered for IR generation [31]. The fundamental mode of the Neodymium Yttrium Aluminum Garnett (Nd:YAG) laser [32] at 1064 nm and the harmonics at 532 and 266 nm are normally used. The latter part of the nanosecond laser beam reheats the laser-induced plasma which increases the plasma lifetime and intensity but also increases the background as well. Solid-state Nd:YAG lasers operated in the Q-switch mode to generate high energy laser pulses with pulse durations in the nanosecond range are the most common lasers used in LIBS experiment. The

Nd:YAG lasers are usually flashlamp pumped although diode pumped lasers are becoming more popular as they offer compactness, better pulse reproducibility and better quality factor ($M^2 < 1.3$).

Femtosecond lasers [33] with pulse duration ranging from tens of femtoseconds to few hundreds of femtoseconds are becoming more important in LIBS due to a number of advantageous features as described in the section 2.3.1. In comparison to nanosecond lasers, femtosecond coherent sources are characterized by higher irradiance and lower ablation threshold values [34]. One of the main feature of femtosecond lasers is the use of the chirped pulse amplification (CPA) technique where the low power femtosecond pulses generated by a seed laser are temporally stretched to multi picosecond widths and then amplified using an additional amplified laser. Finally, the amplified pulse is recompressed temporally down to the femtosecond pulse width scale using a grating based compressor. A Ti:Sapphire (Spectra-Physics Hurricane) laser was used to generate $\sim$ 120 fs (FWHM) pulses at 800 nm with a maximum energy of $\sim$ 600 μJ for all our studies in this thesis.

Other types of lasers can be used in LIBS, such as CO_2 or excimer lasers to work in the far IR or UV ranges, respectively. Pulsed high power fiber lasers are also very promising for LIBS related work [35]. Fiber lasers use the same rare earth active species as solid-state lasers but the active medium is embedded in an optical fiber rather than a rod, with the consequent advantage that the longer interaction length results in better mode quality and higher photon conversion efficiency [36]. Both Q-switching and modelocking techniques are used to obtain very short pulses. They are compact with very good beam quality and variable pulse widths.

Pulse energy is another important factor for ablation and plasma formation. In general, laser energy fluence (energy per unit area, J/cm^2) or irradiance (energy per unit area and time, W/cm^2) are reported instead of absolute value of pulse energy. Generally more pulse energy produces a bigger plasma with

longer lifetime and stronger emission. Overall, the plasma characteristics depend on the collective responses to the laser pulse energy, wavelength and pulse time.

2.1.2 Focusing and Light Collection System

Focusing optics are required in the laser beam path which focus the laser pulse energy into a small focal spot to exceed the threshold fluence value for creating plasma. Ideally a Gaussian shaped beam can be focused by a lens to a beam waist radius of w_0,

$$w_0 = \frac{2f\lambda}{\pi D} \tag{2.1}$$

where f is the focal length of the lens, λ is the wavelength of the laser, and D is the diameter illuminated on the lens. Lenses, microscope objectives and reflective focusing objectives (Schwarzschild type) are normally used to focus the laser beams onto the sample. The material of the lens should be chosen such that it has high transmission at the laser wavelength.

The second optical beam path used in LIBS experiments is used to guide the emission light from the plasma to the spectrometer. The efficiency of collection of light from the plasma determines the strength of the LIBS signal and thus the efficiency of the whole system. A lens arrangement that forms an image of the plasma plume at the entrance slit of a spectrometer is generally used as a light collection system. In other cases, either an optical fiber very close to the plasma location collects light or a lens is used to collect the light emitted by the plasma and then couple the light into a fiber optic coupler with a typical numerical aperture of 0.22. Telescope based optical systems are used for remote LIBS analysis to focus the laser beam and collect the radiation emitted by the sample which is located several meters away from the instrument [37].

2.1.3 Spectrometers and Detectors

Spectral detection systems utilized in LIBS experiments are a combination of a wavelength-selector unit (a narrow band-pass filter or a spectrometer) and an optical detector. The spectrometer or spectrograph diffract the light collected from the plasma emission and reveal the spectral signature. Then the light is detected by optical detectors such as a photomultiplier tube (PMT), a photodiode array (PDA), a charge-coupled device (CCD) or an intensified charge-coupled device (ICCD). The LIBS spectrum is characterized by multiple emission lines spread over the vacuum ultraviolet to near infrared region. The factors characterizing an ideal spectrometer-detector combination would be

- Wide band spectrometer with high spectral resolution allowing simultaneous measurements of different elements
- A detector with high quantum efficiency and short readout & data-acquisition time

Different types of spectrometers such as Littrow, Paschen-Runge, Echelle, and Czerny-Turner are available although the Czerny-Turner spectrograph is the most common device used by the LIBS community [38]. This spectrograph is composed of an entrance slit, two mirrors, and a diffraction grating as shown in Fig 2.1. The light enters through the slit and reaches the first mirror which collimates the light and reflects it onto the grating. The dispersed radiation by the grating is imaged by a second concave mirror to a detector plane. This spectrometer can be coupled to suitable detectors to offer time resolved measurements. The resolution as well as spectral coverage in a Czerny-Turner is lower in comparison to another popular spectrometer known as Echelle spectrometer. There is a trade off between the total bandwidth acquisition and the resolution of a Czerny-Turner spectrometer. For higher resolution the total wavelength range is narrow while a wide wavelength region can be obtained by using a suitable grating with very low spectral resolution.

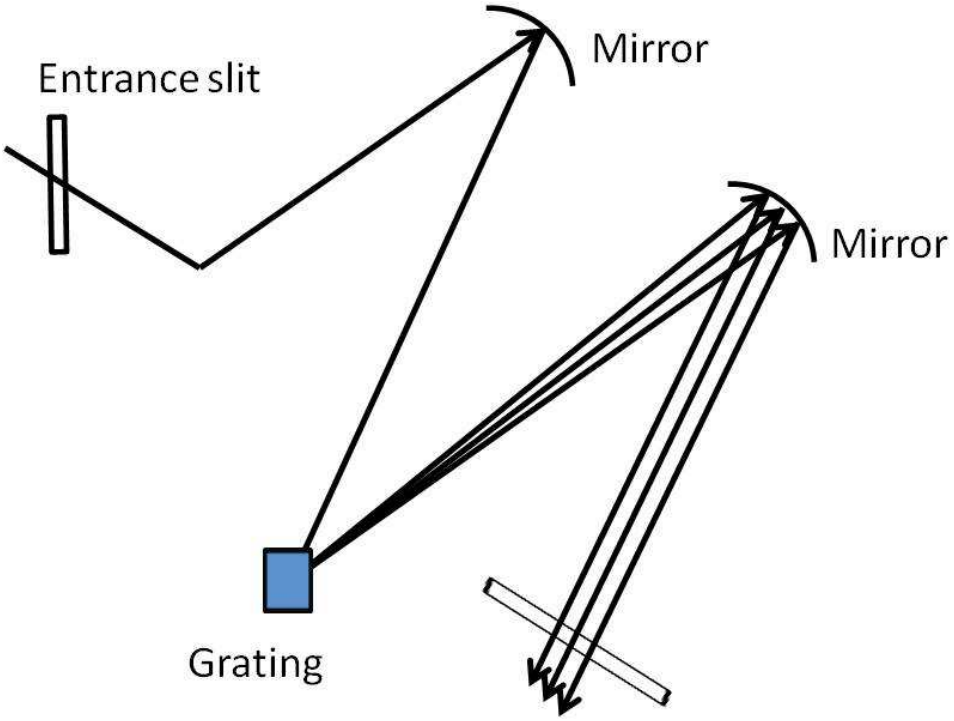

Figure 2.1: Schematic of a Czerny-Turner spectrometer

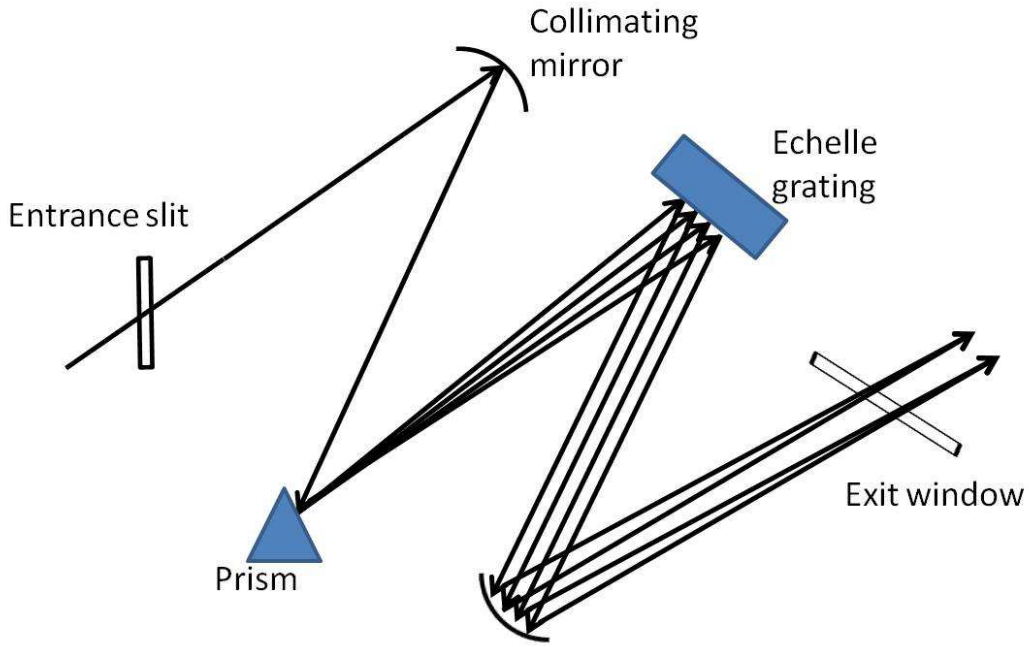

Figure 2.2: Schematic of a Echelle spectrometer

An Echelle spectrograph [39] is typically used to spread out the spectral components of collected light in both X and Y directions. These spectrographs have two dispersive elements, which are typically an echelle grating and a prism. The two dispersive elements disperse the light at right angle to one another. The prism separates the different orders of spectra and the echelle grating with large blaze angle produces large dispersion in higher diffraction orders to ensure high resolution. Therefore the dispersed light on the CCD provides spectral information in both the X and Y directions. Echelle spectrometers need a two-dimensional detector. The biggest advantage of the Echelle design is that it can provide a high resolution and large bandpass simultaneously. The bandpass provided by Echelle systems is mainly dependant on the characteristics of the Echelle grating and also the acquisition camera. Typical Echelle spectrometer covers a wide range of wavelengths from 200 nm to 1000 nm in a single shot. Echelle systems can be made very compact and are suitable for field based applications. Multi-elemental analysis of various types of samples can be efficiently carried out with an Echelle spectrometer in combination with a detector system. Haisch et al. [40] have demonstrated substantial improvement in the detection limits obtained for several elements with an Echelle system as compared with those obtained with a conventional Czerny- Turner system.

In some cased narrow bandpass optical filters coupled with photodiode as a detector are employed in LIBS spectral detection units. The filter allows only one spectral line with limited detection capability. Each spectral line determination needs one specific filter in this arrangement. Acousto-optical tunable filters (AOTF) [41] and liquid crystal tunable filters (LCTF) [42] have also been used instead of single line optical filters. Both AOTF and LCTF have a rapid tuning speed and are sometimes employed in connection with bi-dimensional detectors to form the image of the plasma at a given emission wavelength.

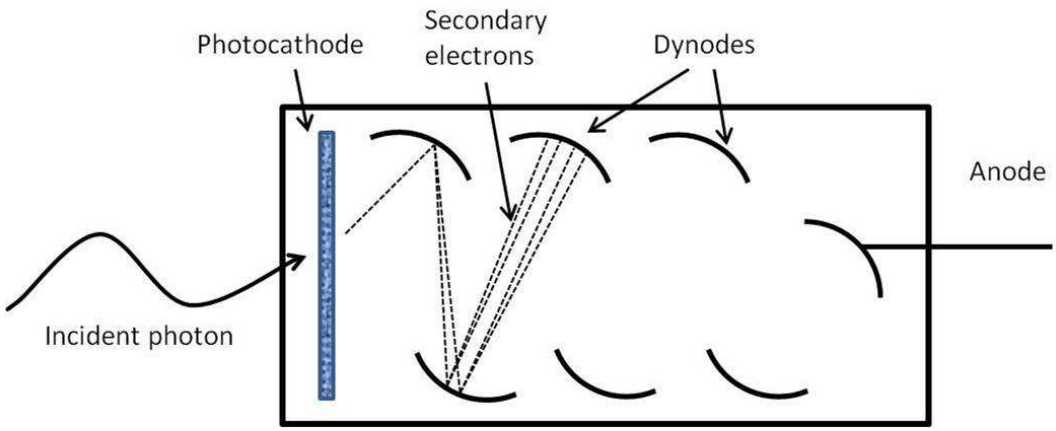

Figure 2.3: Schematic of a photomultiplier tube.

Spectrally resolved light through the exit window of a spectrometer falls on the detector system which generates electrical signal from the optical radiation. Depending on the application, different kinds of detectors are used in LIBS such as: photomultiplier tubes (PMT), photodiodes, photodiode arrays (PDA), charge coupled devices (CCD)/ Intensified CCD's (ICCD) and the streak cameras. Both PMT and avalanche photodiodes (APD) [43] can be used to measure light intensity without spectral decomposition. A PMT is composed of a vacuum tube containing a photo emissive cathode and dynodes as shown in Fig. 2.3. Electrons are generated when photons strike the cathode due to the photoelectric effect and accelerated towards dynodes by a positive potential. Additional electrons are generated after striking each dynode thus a rapid cascade amplification of electrons takes place. Photodiodes are conventional semiconductor diodes which are reverse biased where a electron-hole pair is generated after a photon of sufficient energy strikes the diode. Electrons move toward the cathode while holes migrate toward the anode and generate photocurrent whose intensity is proportional to the number of the incident photons. An APD is operated with a relatively high reverse voltage. The charge carriers are strongly accelerated in the strong internal electric field and generate secondary carriers through the avalanche process. Thus the gain or the effective amplification of the photocurrent is significant. PDA's are one dimen-

sional arrays of several discrete photodiodes. Spectrograph can be combined with PDA's to obtain one-dimensional spatial information or integrated with an intensified photodiode array (IPDA) for time-resolved measurements.

Two-dimensional spatial information can be obtained by using CCD's and ICCD's. A CCD has photosensitive elements called pixels. A two dimensional array of pixels allow an image pattern to be stored digitally keeping the pattern unaltered. A detailed description of CCD and the use of CCD's in scientific areas are given by James R. Janesick [44] in his book. A CCD is intrinsically an integrating detector of the incident light with integration time of typically 1 ms or more and thus incapable of obtaining a high speed gated time resolved spectrum. The signal to noise ratio (SNR) in LIBS depends on the time of acquisition and thus typically a gated time window for light acquisition is required. The high intensity continuum emission during the early phases of the plasma needs to be blocked and a fast gating capability is required for LIBS experiments. An ICCD, the most widely used detector for LIBS studies, improves the SNR and is better for time-resolved detection using windows of a few nanoseconds. The intensifier unit in an ICCD is composed of a photocathode, a microchannel plate (MCP) and a phosphor screen. The photocathode converts incident photons into electrons. These electrons are accelerated towards the MCP by an applied control voltage and then multiplied by a large factor inside the MCP. These electrons are further accelerated and strike the phosphor screen that converts the multiplied electrons back to photons. Finally, the photons are brought to the PDA or CCD either with an imaging lens or fiber optic coupler. The gate window functionality in a ICCD is normally obtained by pulsing the control voltage applied between the photocathode and the MCP during the desired time interval. Photoelectrons cannot reach the MCP during the period when the voltage is revered and no output from the phosphor screen will be generated. A performance comparison between spectrometer/ICCD and spectrometer/non-intensified gated CCD systems in terms of spectrochemical

analysis of four elements in aluminum alloy samples and three elements in copper alloy samples have been documented by Sabsabi et al. [45]. The only concern related to ICCD's is the price, which is much higher than CCDs.

2.1.4 Background Atmosphere

The plasma plume expands in the surrounding atmosphere in front of the target. Detailed plasma plume analysis at different background gas pressures is documented in Chap. 6. Typical ambient gases applied for LIBS to analyze solid or liquid substances are Argon, Nitrogen and atmospheric air. The plasma size, propagation speed and emission properties are related to the neutral particle density in the ambient gas. Mass ablation efficiency and the spectral light emission intensity changes with background gas pressure. At low gas pressure a less confined plume will evolve. Yalcin et al. [46] have characterized femtosecond laser produced LIBS emission as a function of background pressure. Characteristic emission lines from Al, Mg, Si and Cu elements showed significant enhancement in signal to noise ratio at a few Torr background pressure in comparison with atmospheric pressure. The enhancement was due to the larger plasma size and longer lifetime of the plasma at low pressure. Laser vaporization and excitation processes of solid samples in different gases with different pressures have been reported [47]. The ablation rate increases at lower ambient pressures. A reduction of the pressure from 1 bar to 0.1 mbar increases the ablation rate by a factor of 5 [48]. The electronic configurations of the gas species also influences the absorption features for electromagnetic radiation. It has been demonstrated that the electron temperature and density in the plasma differ significantly for Argon, air and Helium [49]. This technique has also been applied inside water environment [5] and even in the extraterrestrial Mars environment.

2.2 Laser-materials Interactions

Laser can be treated as a source of heat and energy in the complex phenomena of laser-material interaction. Lasers used for LIBS related studies have pulse widths in the fs to ns range. The interaction physics changes as one goes from femtosecond to nanosecond pulses. When the laser beam is irradiated on materials, photons are absorbed by electrons and create a non-equilibrium excited state of the energized electrons. The initial coupling of the laser radiation with most materials is through linear absorption although transparent dielectric materials with energy band gaps greater than a single photon energy require multi-photon absorption which is a nonlinear process. The probability of nonlinear absorption increases strongly with the incident laser beam intensity [50]. An n-photon transition has a probability of occurrence which varies with I^n where I is the intensity of the laser pulse. The probability of multi photon absorption process is low and thus the laser intensity, I, needs to be relatively high for the onset of such a process. These electrons are either conduction band electrons for metals or valence band electrons that are promoted by absorption of photons into the conduction band for semiconductors and dielectrics. Another important process during the timescale within the initial part of the laser pulse is avalanche ionization [51]. The free electrons in the conduction band of the material are accelerated by the laser field and the kinetic energy of some of these electrons exceed the ionization potential of bound electron. These electrons can further ionize more bound electrons via collisions. Therefore this process of impact ionization creates two free electrons. Then the emitted electron and the incident electron interact with more atoms through further impact ionization. As long as the laser field is present, this repetitive process leads to rapid exponential growth of the electron density. A schematic diagram showing the multiphoton absorption and avalanche ionization process is shown in Fig.2.4.

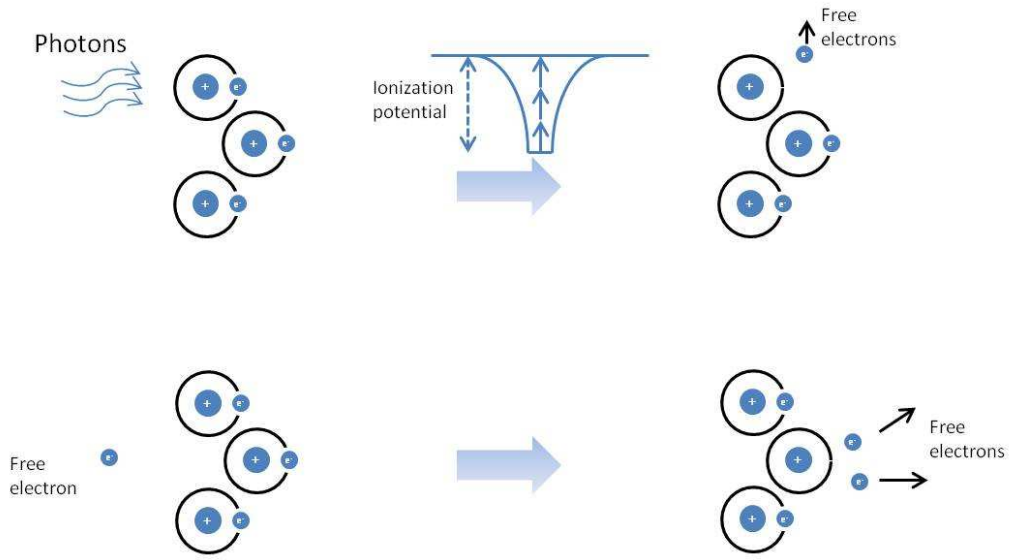

Figure 2.4: Multiphoton ionization (top) and avalanche ionization (bottom)

In the presence of free electrons, the dominant mechanism for absorption of laser light by electrons is inverse Bremsstrahlung (IB) or collisional absorption. This leads to rapid heating of the electrons in the plasma which is formed. In the case of sub-picosecond laser pulses the ions remain cold during the laser pulse interaction with materials. The electron distribution thermalizes through electron-electron interactions on a fast timescale within a few femtoseconds for ultrashort pulses [52]. The electron-ion thermalization occurs over a timescale of picoseconds or longer depending on density. For longer laser pulse duration, the electron-ion thermalization occurs within the laser pulse widths. Very high energy ballistic electrons may decouple and have slightly longer lifetimes.

2.2.1 Ablation Mechanism

The dissipation of the absorbed energy in bulk material, and the corresponding target material removal, takes place after the laser pulse finishes for ultrashort laser pulses. We have seen that a large number of electrons are liberated and some ejected from the target when the material absorbs laser light. The hot electrons then interact with the lattice through electron-phonon scattering

process and the energy transfer from the electrons to lattice occurs on on a timescale given by the electron-phonon coupling constant, which typically of the order of picosecond timescale [53]. The charge separation of electrons with the parent ions creates a strong electric field. The magnitude of the electric field depends upon electron kinetic energy and the gradient of the electron density along the normal to the target surface. This leads to electrostatic repulsion of ions in the surface layer and the movement of the ions away from the solid target escaping the binding energy of ions in the lattice in a process called coulomb explosion [54]. Therefore the surface of the target will break apart by emitting the positive particles and ablation occurs. This process of phase transformation dominates at low laser fluence conditions near ablation threshold. It has been studied through Molecular Dynamics (MD) [55] simulation and experiment [54]. R. Stoian et al. [54] have given a detailed analysis of coulomb explosion during the ultrashort pulsed laser ablation of Al_2O_3. The process is important in creating a small ablation zone, selective removal of the top target layer and nanostructuring of material surfaces. The irradiance of the laser significantly influence the ablation dynamics during laser-matter interactions. In the regime of higher excitation energies, the electron-phonon collisions takes place over a large volume. The bulk volume is super heated and the local temperature goes above the thermal vaporization point. The rapid heating leads to a metastable liquid volume that creates homogeneous nucleation of the vapor nuclei. The explosion of the vapor bubble results the ejection of molten mass from the surface. This mechanism is sometimes called the phase explosion or explosive boiling [56, 57]. The plasma dynamics and its expansion, shock wave formation and propagation, collision with background neutrals, deceleration in ambient background gas in the femtosecond laser pulse regime is discussed in Chap. 6. The trailing part of the long nanosecond laser pulses can also interact directly with the expanding plasma plume formed at the surface of the target material.

2.2.2 Emission Processes

The laser induced plasma emits light which consists of continuum emission, band emission and discrete line emission. The spectrum from a laser ablated plasma is time dependent and evolves rapidly with time. The density and temperature of the plasma are very high in the initial stages of plasma. A broad continuum spectrum is observed at the early times of plasma emission where the hot dense plasma emits light due to the free-free and free-bound transitions by the electrons in the field of an ion. This effect of continuum radiation is called Bremsstrahlung [58]. After the plasma temperature decreases and density decreases, de-excitation of the ions through various energy levels produce characteristic emission lines for each kind of element from bound-bound transitions. These discrete lines have three main features; wavelength, intensity and shape. The parameters depend on the atomic structure and the environment. Different atoms in a multi elemental plasma have different distinct energy levels which determine the wavelengths of the line emission. The intensity and shape of the emission lines depend strongly on the environment of the emitting atom. The emission intensity of a particular element will be proportional to the concentration of that element in the plasma plume. Natural broadening (due to Heisenberg's uncertainty principle) and Doppler broadening (due to thermal motion of the emitters) are important at moderate plasma density. At high plasma density, the electric field created by the moving electrons and ions perturb the atomic energy levels and broaden the emission lines. This is called Stark broadening. This broadening along with spectral line intensities can be useful to determine plasma density [59, 2]. The calculation of these parameters are valid in a local thermodynamic equilibrium (LTE) [60] environment where electron, ions and atoms in the plasma are at the same temperature. LTE is a dynamic state reached after several nanoseconds during the plasma relaxation. The plasma temperature is very high initially but fast collisional processes bring the plasma to a common temperature and approach the conditions of

LTE. These conditions are

- Electrons have a Maxwell energy distribution and all the species have the same temperature with a velocity distribution given by

$$f_M(\bar{\nu}) = \left\{ \frac{m_e}{2\pi K_B T} \right\}^{3/2} e^{-m_e \nu^2 / 2K_B T} \tag{2.2}$$

- The population of energy levels follow a Boltzmann probability distribution

$$\frac{N_m}{N_n} = \frac{g_m}{g_n} exp \left\{ -\frac{E_m - E_n}{K_B T} \right\} \tag{2.3}$$

- Species at different degrees of ionization are described by the Saha equation

$$\frac{N(Z,0) n_e}{N(Z-1,0)} = 2 \frac{g(Z,0)}{g(Z-1,0)} \left\{ \frac{m_e K_B T}{2\pi\hbar^2} \right\}^{3/2} exp \left\{ \frac{-\chi_i (Z-1,0)}{K_B T} \right\} \tag{2.4}$$

where N_n, E_n and g_n are the population, the energy and the degeneracy of quantum level n, K_B is the Boltzmann constant, T is the temperature, N(Z,0) is the ground state population density with designated ionic charge Z, n_e is the electron number density, m_e is the mass of the electron and χ_i is the ionization energy.

A simple criterion has been derived by McWhirter defining the parameter range for which the plasma is in local thermodynamic equilibrium (LTE). This criterion is defined as [1]

$$n_e \geq 1.6 \times 10^{12} T^{1/2} (\triangle E)^3 \tag{2.5}$$

where the electron density is in cm^{-3}, T is in K and $\triangle E$ is the energy of the first level above the ground state in eV.

2.3 Laser Micromachining

When a focused laser beam selectively removes materials from a target substrate to imprint a desired feature on the surface of the substrate or to create an internal feature inside the target, the process is called laser machining. Lasers with their excellent beam quality, compact size, moderate system price and easy integration have allowed high precision material processing at the micro/nano scale levels. Lasers employed for micromachining span a wide range of wavelengths (from UV to IR), pulse duration (from femtosecond to microsecond) and repetition rates (from single pulse to Megahertz). These features have allowed laser micromachining [61] to deliver high resolution in depth and lateral dimensions with significant processing speed. By controlling the incident fluence and number of laser pulses, and hence the total incident radiation, precise control over machining depths can be achieved. The process is noncontact and comparing to other mechanical machining techniques, laser machining can produce shallower heat affected zones in the working sample. Other advantages of using lasers for material processing is that they are environmentally clean, offer easy automation integration and lead to efficient material utilization. Both CW and pulsed lasers are used for micromachining processes. Laser machining requires rapid heating, melting and evaporation of the target material. The most common types of lasers used in laser-micromachining are gas, solid state, semiconductor and liquid dye. Traditionally gas and solid state lasers were the most commonly used for most industrial machining applications as given in Table 2.2.

Type	Medium	Wavelength
Gas lasers	Excimer	193-351 nm
Gas lasers	CO_2	10 μm
Solid state lasers	Nd:YAG	1064 nm

Table 2.2: Lasers most commonly used in the industry for industrial machining applications

Writing of microstructures using lasers is commonly done by either direct

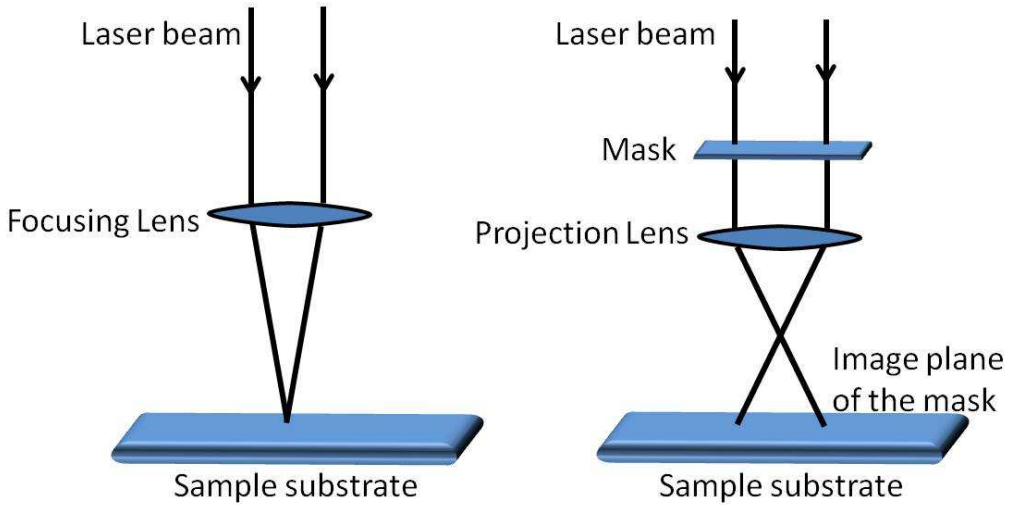

Figure 2.5: Direct laser writing and mask projection techniques

writing or mask projection techniques. These two processes are shown in Fig. 2.5. In direct write laser micromachining, the laser beam is tightly focused to a small ablation spot which can be moved across the target sample surface during machining. Typically Gaussian laser beam profiles are used for this purpose. Control of the beam movement over the surface allows the creation of 2D patterns or even 3D micro structures. The mask projection technique is similar to photolithography where transfer of all information contained in a fixed transmissive mask is imaged onto the target substrate. It uses a large area uniform intensity laser beam at the mask plane and a projection lens. Large area multi mode beams are often used for mask projection laser micromachining. The processing speed can be higher in this case although each new pattern requires a new mask.

In some applications where periodic micromachining of the substrate is needed, holographic diffraction technique involving splitting of a laser beam followed by superposition of the beams to generate interference patterns has also been adopted. The geometry of the interference patterns formed by the superposition of two or more coherent and linearly polarized beams depends on the wavelength and the angle between the beams. This type of pattern can

produce unique intensity variation on the substrate surface.

The wavelength of the incident laser light restricts the feature size on the substrate and thus, near field optical techniques are sometimes applied to obtain nanometer scale features. Scanning near-field optical microscopy (SNOM/NSOM) [62] is a microscopy technique where the separation distance between detector and substrate is smaller than the applied probe wavelength. The laser light is coupled into the fiber and emitted through the sub-wavelength aperture of the fiber tip. This technique can be used at atmospheric pressure and is able to write sub-wavelength patterns on the target surface because aperture is smaller than the diffraction limited value. The resolution of the image is limited by the size of the detector aperture and not by the wavelength of the illuminating light. Nolte et al. have demonstrated [62] 200 nm wide lines written on a chrome surface using 100 fs, 266 nm laser pulses at 1 kHz. Zorba et al. [11] have produced an ablation crater with 27 nm (FWHM) feature size using 100 fs, 400 nm laser sources. Direct creation of holes with crater diameter of 15-30 nm have been reported by Joglekar et al.[63].

The other way to downsize the laser-matter interaction region is to use AFM probe tip to concentrate laser radiation in the gap between tip and surface. An effective feature size of the order of 10 nm was demonstrated by Chimmalgi et al.[64]. The probe tip was placed a few nm from the target surface and 800 nm, 83 fs laser pulses were used at 1 kHz.

2.3.1 Femtosecond Laser Micromachining

Although the choice of laser is dependent on the specific application requirements, the nanosecond pulse regime has been used extensively in the laser-machining industry. However, a number of studies have shown that femtosecond lasers are capable of producing much smaller features without collateral damage to the surroundings because of smaller heat affected zone compared to ns pulses [65]. Typical heat diffusion time is of the order of a nanosecond and

electron-phonon coupling time in the picosecond time scale. Femtosecond laser pulses deposit energy on a time scale much shorter than both the heat transport and the electron-phonon coupling times and, therefore, the light-matter interaction process is essentially instantaneous in time. The laser induced heat affected zone is transformed from solid to vapor phase then to plasma state on the picosecond timescale. The depth of the heat affected zone (HAZ) is proportional to the square root of the pulse duration and thus is quite a bit larger for nanosecond pulses. The width of the HAZ also depends on the target material properties, laser energy fluence and pulse repetition rate. The ablated mass removed from the target depends on the deposited energy per pulse. In general, μJ and mJ pulse energies are employed for femtosecond and nanosecond laser ablation, respectively. The laser induced plasma expands and interacts with the incoming laser beam in nanosecond pulses, whereas no post plasma heating is obtained for femtosecond pulses. For materials with high thermal diffusivity such as metals, femtosecond laser pulses are used for precise pattern fabrication.

The most common lasers used today for micromachining are solid-state ultrafast lasers, with gain media such as;

- Titanium doped sapphire (Ti:Sapphire)
- Ytterbium doped yttrium aluminum garnet (Yb:YAG)
- Ytterbium doped potassium yttrium tungstate (Yb:KYW)
- Ytterbium doped potassium gadolinium tungstate (Yb:KGW)

Focusing the output of a femtosecond pulsed laser often makes possible exceptionally high quality machining for a wide variety of materials including transparent solids, ceramics, metals and polymers. To obtain nano scale features on the substrate different approaches such as near field focusing optics, ultraviolet wavelengths and short wavelength free electron laser sources have also been applied.

2.3.2 Effect of Background Environment

Laser ablation produces a strong expanding shock wave which carries the debris particles outwards from the ablation spot during expansion. In the process of stagnation and cooling, the rarefied region behind the shock front is filled with returning gas, which then carries the debris back to the surface. The accumulation of debris during laser micromachining [66], which is one of the drawback in this process, can be reduced by using suitable background environment for micromachining such as at a low background gas pressure, gas assist nozzle and liquid environment. At lower background gas pressure, the expansion radius of the shock wave in the ablation plume is much larger and therefore, the ablated mass will be deposited over a larger area as the shock wave collapses. At low background pressure, the amount of redeposition of the ejected particles from the ablated crater is reduced substantially and the size of recast layer is reduced as well. Singh et. al. [67] have demonstrated the effect of ambient air pressure on debris redeposition during laser ablation of glass. They have shown that the debris redeposited onto the target surface leads to a rough surface at higher ambient pressure. Much cleaner and smoother debris morphology was observed at low background pressure ($\sim$ 11 Torr). The measured debris field radii were found to be proportional to the inverse cube root of the ambient air pressure.

In some cases laser energy is delivered to the cutting zone assisted with a coaxial gas flow [68], that can be either oxygen (O_2), air, or an inert gas depending upon materials and the machining requirements. This method can be used for both on-axis (perpendicular to surface) and off-axis (angled to surface) cutting. The process is simple and easy to implement using a co-axial gas nozzle integrated into the focusing optics. Such a coaxial gas nozzle blows the unwanted molten material away and the desired features are produced using this continual cycle of melt ejection.

The other option to reduce the heat affected zone and ablated materials is

by micromachining in liquid environment. The thermodynamics and kinetic properties of the laser-induced plasma plume are different in liquid from those in vacuum or gas environments due to the confinement of the plasma plume by the liquid. The plasma plume lifetime is shorter in liquids compared to air [69]. Ablation under water and ethanol showed cleaner surfaces and less debris re-deposition compared to ablation in air[70]. Femtosecond laser induced periodical surface structures with liquid assist have been reported by Jiao et. al. [71]. They have found that ethanol environment produced cleaner surface ripples with a period of 450 nm when using 775 nm, 200 fs laser pulses. Patel et. al. [72] have compared craters and nanostructures of brass and Aluminum in water and air environment. They have shown that the ablation process is more efficient in water than air and depends on the thermal properties of the materials.

2.3.3 Applications

Laser micromachining and especially femtosecond laser micromachining has several applications in different areas such as;

- **Micro and nano patterning of materials** - Material processing with submicron resolution and fabrication of micro parts at high speed has been one of the important applications of this process. Typical applications include engraving, micro-drilling, micro-milling, cutting, structuring, as well as marking. 2D nanostructures and complicated 3D patterning [73] of microstructures were demonstrated. The fabrication of micro-electro mechanical systems (MEMS) components using laser techniques is growing rapidly.

- **Micro-fluidic transport systems and fluid mixing devices** - Laser drilling has found wide application in the manufacture of fluid injector nozzles in the automotive industry. In printing applications, ink-jets are

laser fabricated. “Lab on a chip” systems for cellular biology, biosensors are all now laser manufactured. 3D microfluidic components with arbitrary geometries are also fabricated in glass substrates by femtosecond laser direct writing [74].

- **Medical & Biotechnology** - Laser applications in these areas include microchannels in polymers, machining thermally sensitive materials (laser micro dissection, cleaning, sterilization, fabrication of implants, correction of corona, dermatology, surgery etc.). Process optimization of precision medical device manufacturing was discussed by Chen et al. [75]. Ablation of molecular structures in living cells using low-repetition rate, low-energy femtosecond laser pulses has also been reported [76]

- **Fabrication of optical devices** - It has been demonstrated using machining of micro-lenses or diffractive optical elements in optical materials with a high surface finish. Optical devices used for on-chip sensing or for display panel enhancements. Fabrication of an optical sensor through femtosecond laser micromachining was demonstrated [77]. The sensor was suitable for all-optical sensing of displacements, vibrations, and accelerations with minimum temperature dependence and immunity to external electromagnetic fields. Machining of optical waveguides in bulk glasses or silica for circuits and other telecommunications devices. Microstructuring of optical fibers with femtosecond laser pulses has been demonstrated by Sohn et al.[78]. These mircomachined optical fibers were used for long period fiber gratings and cladding mode mirrors.

- **Micro welding** - Effective welding of miniature parts with high yield requires techniques for holding the parts in contact with a controlled force and applying a highly localized heat source to the weld area. The localized heating associated with a focused laser beam is ideal for welding of miniature metal and plastic components. Recent results and trends in

ultrashort laser welding and joining are reported [79].

- **Thin film masks** - Structuring and repair of photolithographic masks [80] is a major application area.

- **Laser cleaning** - Cleaning of surfaces from contamination layers is a growing area of application. Surface smoothing and selective machining of multi-layer devices without affecting particular layers can be carried out. Oxide layer removal [81] is another specific area.

- **Micromachining in solar cell productions** - Laser used in a number of applications in solar cell production including: edge isolation, selective ablation, grooving and structuring on thin film (Si, Cadmium Telluride(CdTe), Copper Indium Selenide(CIS)/Copper Indium Gallium Selenide(CIGS)) as well as mono/polycrystalline solar cells. Development of a high energy and high average power femtosecond fiber amplifier tailored for thin film CIGS solar cell scribing has been demonstrated [82].

- **Chemical analysis of materials** - Several laser based chemical analysis techniques for material characterization have been developed such as thermal lens spectrometry [83], laser enhanced ionization spectrometry [84], laser photoacoustic spectrometry [85], Laser Induced Breakdown Spectroscopy (LIBS) [2], Laser Ablation Inductive Coupled Plasma Mass Spectroscopy (LA-ICP-MS)[86], laser based Raman [87]/fluorescence [88]/infrared [89] spectroscopy which can be used for contaminants and impurity analysis for environmental monitoring, forensics chemical analysis, medical and pharmaceutical analysis etc.

2.4 LIBS as a Tool for Microanalysis

The applications of LIBS has already been summarized in Table 1.1. One important goal of LIBS is to achieve quantitative chemical analysis at the atomic

level in order to identify relative amounts of different elements in the sample by analyzing laser induced spectra. The key step is to create an optimum environment for obtaining LIBS spectra and proper identification of the emission spectra. Considering that the overall mass removed per laser pulse is in the sub-microgram level, LIBS is classified as a micro-invasive technique. The probe volume on the target material with LIBS is small and even smaller precise micromachining can be done with femtosecond pulses as described in previous section. Femtosecond lasers are more efficient for creation of very small micro-plasmas. Suitable light detection from the micro-plasma could lead to simultaneous elemental characterization of the material. This can be termed as LIBS microanalysis of materials. The laser pulse energy determines the extent of the heat diffusion in the material and in turn, the spatial scale of material analysis. Therefore probing of smaller sample spots for microanalysis applications requires much lower pulse energies, often in the range of few microjoules. This extension of LIBS for microanalysis is microLIBS (μLIBS) [90]. Key characteristic quantities of importance for quantitative LIBS are the signal to noise ratio (SNR) and the limit of detection (LOD) [91]. A small discussion on SNR is given in Chap. 5.3 and LOD is well documented in LIBS literature [92, 93, 94, 9]. LOD of a LIBS setup is determined by varying the concentration of an element of interest and recording the emission levels using Eq. 2.6,

$$LOD = \frac{3\sigma_B}{S} \tag{2.6}$$

where σ_B is the standard deviation of the variation in the background noise and S is the sensitivity of the system to the analyte [90].

During the past decades, the potential of LIBS as a surface characterization tool for lateral scanning of compositional distribution and depth-profiling have been demonstrated. In comparison to other analytical techniques, LIBS offer sampling flexibility in combination with a fairly good lateral resolution, depth

resolution and high sensitivity for trace impurity characterization. An overview of depth and lateral resolution for LIBS microanalysis is given below.

2.4.1 Depth Resolution

Depth profile analysis determines the depth location of different elemental constituents in a multi layered target by analyzing LIBS spectra from successive laser pulses delivered at the same point and recorded individually. In general a larger focal spot is chosen for depth profiling to ensure sufficient photons from the plasma light when using a very shallow depth of ablation per shot. The laser beam profile is an essential component in determining the quality of the depth resolution during the ablation process. Both Gaussian and flat-top profiles are used. However the flat-top profiles are better in order to generate a relatively flat bottom hole and the ability to work a uniform low ablation rate. An important concept in this domain is the average ablation rate (AAR) which is described in detail in Chap. 5. Chap. 7 demonstrates the efficiency of LIBS depth profiling using these two types of pulse shapes. LIBS and especially fs-LIBS has been shown to be able to perform depth profile analysis over the last decade. There are many application areas which could utilize this technique for quantification of layered material structures.

In the 1980's, Y. Talmi [95] obtained a depth profile of an electrical capacitor with a silver conducting layer. They have used a ruby laser pulse (694 nm, 0.6 - 1.2 J) focused through a 40X objective (0.5 N.A.) to successively ablate the material during depth profiling. A silicon intensified vidicon detector was used to acquire the spectrum from each laser shot. The ablation crater depth from the first lase shot was 12 μm. Lorenzen et al. [96] have used repetitive laser pulses on TiN coated metallic substrates and a time-gated photodiode array detector to obtain ablation depth per pulse of 0.1 μm. They have obtained the thickness profile of TiN on the sample surface with coating thicknesses of $\sim$ 1 to 5 μm. Anderson et al. [97] have reported quantitative depth profiling

studies using LIBS. A Zn/Ni coating between 2.7 and 7.2 μm thick on a steel substrate was analyzed. The influence of experimental parameters on emission signatures was examined. A micron order resolution was reported. Laserna and coworkers have done substantial LIBS depth profiling related work since 1997 [98, 99, 100, 101, 102, 103, 10]. They have resolved complex depth profiles of electrolytically deposited brass samples [98], used XeCl excimer laser laser pulses (28 ns FWHM) to obtain a depth resolution of 8 nm per pulse [99] and compared the results to Glow Discharge Optical Emission Spectroscopy (GD-OES). The minimum ablation rate was reported by them as < 2 nm per pulse [102]. The effect of incidence angle of the laser pulses with respect to the normal of the sample surface has been examined and an angle resolved LIBS depth profiling was demonstrated. For angle-resolved experiments, samples were mounted on an X-Y-θ linear-rotary positioning stage so that the angle of incidence of the laser could be adjusted from 0^o to 60^o with respect to the normal to the sample surface. Plasma emission was collected at 45^o with respect to the incident beam regardless of the sample angle. The crater depth was significantly reduced by changing the incidence angle. Coated materials (Sn-coated steels and Cr-coated samples) were used as targets. The comparison with GD-OES was excellent. They also demonstrated the capabilities of LIBS for depth profile analysis of phosphorus doping in silicon using Nd:YAG at 532 nm [101] and depth resolved analysis at reduced pressure [100]. The role of irradiance in LIBS depth profiling and optimum depth resolution conditions are discussed by Mateo et al. [103]. Hakkanen et al. [104] have investigated microscopic variations of pigments at different depths in a double-coated paper using LIBS in order to ascertain the quality of papers. They used an ArF excimer laser (193 nm, 10 ns, 10 mJ).

Although nanosecond pulses were used in the beginning of LIBS depth profiling, the use of ultrashort femtosecond pulses has become popular for depth analysis after the advent of femtosecond lasers. Margetic et al. [105] have used

femtosecond laser (775 nm, 170 fs, 0.5 mJ) pulses for depth profiling of Cu-Ag and TiN-TiAlN multi-layers on silicon and iron substrates. The experiment was performed in the pressure range 10 to 1000 mbar. The ablation rate was 10 to 30 nm per pulse depending on the energy fluence from 0.6 to 1.51 J/cm^2. Galmed et al. [106] have evaluated the ability of fs-LIBS to carry out depth profiling of a Ti thin film of thickness 213 nm deposited on a silicon (100) substrate before and after thermal annealing. An average ablation rate of 15 nm per pulse was achieved. The depth profiling was compared to a theoretical simulation model with good agreement. A recent study [107] on the comparison of the performances of nanosecond and femtosecond LIBS for depth profiling of bronze samples has shown the effectiveness of fs pulses over ns pulses. Zorba et al. [108] have used frequency tripled (343 nm) diode pumped Ytterbium laser pulses (500 fs) as the irradiation source to study chemical composition of the solid electrolyte interphase (SEI) layer in Lithium-ion batteries with a high depth resolution. They were able to probe compositional variations within the SEI layer with 7 nm resolution.

The group of Anglos et al. have used LIBS depth profiling to study archaeological, historical and artwork objects. A recent review by them [109] on laser spectroscopies for elemental and molecular analysis in art and archaeology has been focused on different laser assisted analytic techniques. They measured the thickness of protective coatings on historic metal objects using nanosecond and femtosecond LIBS depth profiling [110]. Femtosecond pulses at 248 nm resulted in more controlled laser ablation etching as expected. They have combined LIBS with optical coherence tomography (OCT) to enable depth-resolved multilayer pigment identification in paintings [111], combined white light interferometry for multi-layer depth profiling [112] and combined with Raman spectroscopy for pigment analysis [113]. In the domain of LIBS depth profiling on cultural heritage objects, a few other examples are: Depth profiling of Roman wall paintings from the archeological area of Pompeii [114],

characterization of iron age pottery from eastern Turkey [115], depth profile of gold coated archeological decorative copper objects [116] and stratigraphic characterization of multilayered painted surfaces [117] etc.

Noll and coworker have demonstrated various industrial applications of LIBS depth profiling. They reported online continuous monitoring of the Al depth profile of the hot-dip galvanized sheet steel using LIBS [25]. The method was tested on rotating sheet steel disks moving at a speed of up to 1 m/s. They also have demonstrated online coating thickness measurement and depth profiling of zinc coated sheet steel by LIBS [27]. They used a Nd:YAG laser at 1064 nm in a collinear double pulse mode to achieve an ablation depth in the range of the coating thickness of about 10 μm. They applied single laser bursts to one distinct position on a moving target and obtained depth information by controlling the crater depth (by changing the burst energy in small increments). The LIBS signal was measured for every single laser burst. The achieved thickness resolution was estimated to about 400 nm for coating thicknesses of electrolytic galvanized sheet steel in the range of 3.2 to 11.2 μm.

The potential of multi pulse LIBS arrangement for depth characterization of electrolytically galvanized steel has been presented by Cabalín et al. [10]. They used bursts of 11 laser pulses with inter-pulse delay of 7.4 μs. The ablation efficiency was increased 10-fold on iron and 22.5-fold on zinc with respect to dual pulse or single pulse excitation. The application of LIBS to Mars exploration is a proof of the robustness and diversity of LIBS. The ChemCam instrument which is a LIBS stand-off sensing instrument, was integrated with the NASAs 2011 MSL(Mars Science Laboratory) rover named Curiosity. A recent publication has analyzed the depth profile data from the recent measurements by ChemCam at Gale crater in Mars [118]. They have shown that the martian rock Bathurst-Inlet has a decreasing signal from Li with depth over the 30 shot profile. Depth profile analysis of CIGS (copper indium gallium di-selenide) solar cell structures using a LIBS system have been described by Bol'shakov et

al. [119]. The energy of nanosecond laser pulses (532 nm) was adjusted so that the first 7 pulses removed the top 1.5 μm CIGS layer. The relative intensities of the spectral lines at different ablation depths were characterized. They also have compared LIBS and LA-ICP-MS techniques in this report.

2.4.2 Lateral Surface Resolution

One of the important advantages of the LIBS technique is the capability to determine spatial distribution of the compositional element constituents on the target surface with a resolution limited by the laser focusing capability and the efficient light collection from the laser ablated plasma. The resolution of surface micro-analysis was previously determined by measuring the ablation spot size on the sample surface or the ablation hole diameter (FWHM, in some cases). Instead, the actual lateral surface resolution should infer from the smallest distance within which elements can be resolved as will be described in Chap. 8. In the context of finding lateral resolution, the minimum focal spot diameter to which a Gaussian beam can be focused with a single optical element is a function of the input beam parameters and was shown in Eqn. 2.1. Shorter wavelength laser pulses with a high numerical aperture lens can be focused down to obtain small spot diameters on the sample surface and produce better lateral resolution. In the real situation with a practical Gaussian beam the irradiance at the focal point is reduced by a factor M^2 [120](beam quality factor) with respect to the case of an ideal Gaussian beam profile. A number of factors can degrade the lateral resolution include thermal diffusion length with the sample, lateral expansion of the ablation plume and the re-deposition of ablated material in the crater rim and nearby surface. Under optimal circumstances it is possible to obtain craters that are not much larger than the diameter of the beam spot. In the case of scanning microanalysis, a transverse motion of the focused laser beam across the sample surface enables a linescan across the surface. The element line intensities of the laser-induced

plasma can then be plotted to give the transverse composition of the surface in micro scale.

Geersten et al. [92] were one of the first to report the evaluation of laser ablation optical emission spectrometry for elemental microanalysis in solids. They characterized Al-alloy samples using nanosecond laser pulses (6 ns (FWHM), 35-40 μJ) and obtained a lateral resolution of typically 6 - 8 μm. They have pointed out that the homogeneity of different precipitates in a commercially available Al-alloy was in the range of 5 - 10 μm which was a main difficulty in microanalysis. Kim et al. [121] scanned a solid sample with a 10 μm crater resolution. Häkkänen et al. [104] have analyzed material distributions in paper and paper coatings in order to characterize the quality of paper. Surface analysis of photovoltaic cells using a pulsed N_2 laser at 337.1 nm and 1 mJ pulse energy produced lateral spatial resolution of 30 μm [122]. Laserna et al. [123, 124, 125] have analyzed the distribution of elements through LIBS in studies of carbon impurities in photonic-grade silicon and of distributions of metals in automobile catalytic converters but the resolution was of the order of several 10's of microns. They also used a line-shaped laser focus and an imaging spectrometer to scan the laser line across a stainless steel sample surface. The estimated spatial resolution along the laser line was 17.4 μm [126].

Cravetchi et al. [127, 8, 9] have evaluated the potential of the LIBS for microanalysis of aluminum alloys. In their LIBS configuration the laser beam was focused onto the sample using a microscope objective (10X, N.A. = 0.25) which also collected the plasma emission as well. The detection of chemical composition of particles less than 10 μm in size in an Al alloy was demonstrated with sub-10 μJ nanosecond laser pulses at 266 nm [127]. The single shot laser ablation on Aluminum target could differentiate emission spectra corresponding to the constituents of each precipitate. LIBS scanning was used to distinguish the precipitates (Cu,Fe,Mn, Al,Mg) formed on the sample surface from the normal surface and to quantify the precipitates. Taschuk et al. [20]

demonstrated that μLIBS can be utilized for detection and mapping of latent fingerprints using 130 fs, 85 μJ pulses at 400 nm. R. Noll and coworkers have worked towards industrial applicability of surface resolution of LIBS. The alloy of interest in most of their work was steel due to its wide industrial applications. Direct analysis of liquid steel reduces processing times effectively. They have demonstrated online surface mapping on steel with a spatial resolution of $<$ 15 μm using LIBS [26]. This technique was applied for production control and quality assurance in the steel industry. The repetition rates used for scanning LIBS mostly are limited by the detector read-out time (or the laser repetition frequency) which is normally less than 60 Hz. In the domain of μLIBS with multi-KHz repetition rate fiber or microchip lasers and a detector system that operates in the KHz regime would make a compact and portable LIBS device with very fast scanning capabilities. The other limitation in that case would be expansion and dissipation rate for high-speed LIBS with single-pulse evaluation and the temporal behavior of the line emission of the laser-induced plasma. In μLIBS, the element-specific emission extends over a period of about few μs or less and thus, the process can be repeated at several 10's of kHz provided the translation stage moves according to that speed. So far, the combination of a PaschenRunge spectrometer with PMT detectors have achieved the highest ever measuring frequencies for LIBS at 1 kHz [128] with single pulse evaluation. The lateral resolution achieved for steel samples was better than 20 μm. They used the tightly focused beam of a diode-pumped Q-switched Nd:YAG laser as the excitation source. A detailed review on 'LIBS for Chemical Mapping of Material' was published by Piñon et al. [129].

Femtosecond LIBS for Ca^{2+} analysis of biological samples with high spatial resolution has been studied by Assion et al. [130]. Menut et al. [131] have reported a micro-LIBS device that offers 3 μm spatial resolution to the micro-chemical structures for both conductive and nonconductive samples. Wessel et. al. [132] have applied this technique for 2D mapping of micro cracks on TiAl

alloy surfaces. They obtained spatial resolution of ∼2 μm by accumulating 10 single shot spectra from each ablated spot. Their fs-LIBS setup with a 50X objective would provide a useful tool for examining three-dimensional crack propagation.

An approach adopted in this context was to enhance the optical emission via double pulse LIBS. Y. Lu et. al. [133] have reported spectral emission from a crater in the few micron scale (< 2 μm) using a combination of UV-fs UV-ns double pulse LIBS in an orthogonal configuration. They showed that double-pulse configuration can enhance the spectral emission intensity by roughly 360 times as compared to a single-fs laser pulse LIBS of silicon. J. Mildner et. al. [134] have used femtosecond double pulses to achieve LIBS signal from ablation craters with hole diameters of 650±150 nm. A maximum signal enhancement of about five was achieved at an inter pulse delay of around 800 ps. The other approach to enhance the capability of lateral resolution would be using near-field scanning optical microscopy (NSOM) with LIBS as the size of the probed volume can be further decreased by the application of near-field techniques [62]. Kossakovski and Beauchamp [135] used NSOM with LIBS to achieve spatially resolved chemical images with topographical information. Ablation craters with diameters as small as 200 nm were obtained but without any analytical signal. The potential use of this type of LIBS has been demonstrated but the contamination of the probe by ejected species from the plasma remains a problem in the analysis at various surface locations. The collection of limited number of photons from a SNOM produced plasma is also a challenge for this LIBS technique.

Russo and his group has demonstrated numerous advances in minimizing the lateral resolution using LIBS. They used 400 nm femtosecond laser pulses on Cr thin film to achieve ∼650 nm FWHM crater diameter with detectable LIBS signals [136]. The smallest ever reported single pulse ablated crater diameter width (FWHM) with a measurable LIBS signature was 450 nm [137].

The atomic emission of sodium (Na) and potassium (K) dopants in transparent dielectric Mica matrices was studied in this experiment. Under optimal conditions, the ablated Na mass measured was as low as 220×10^{-18} g at atmospheric pressure.

2.4.3 New Approaches in LIBS

Several approaches have been proposed to improve the analytical performance of the LIBS technique regardless the nature of the sample, such as work under a low background pressure [46] or using two successive laser pulses (dual pulse LIBS) [138, 139]. Yalcin et al. [46] have demonstrated that at the optimum delay time integrated signal intensity of AlI lines show $\sim$ 67 times enhancement at 4 Torr of background pressure in comparison to ambient atmosphere. In terms of sensitivity, the most promising approach seems to be the LA-LIF approach, which combines laser ablation with laser-induced fluorescence (LIF). In this technique plasma is generated by laser ablation and then the atoms of the element of interest in the target material are re-excited by using a second laser pulse tuned to a specific wavelength, corresponding to a strong absorption line of that element. This LA-LIF technique has demonstrated very high detection sensitivity. Lui et al. [140] have demonstrated that 3σ limit of detection of 35 ± 7 ppb could be obtained for quantitative lead (pb) measurement in water by using 10,000 laser shots.

The poor sensitivity of normal LIBS is due to the characteristics of the emission processes during the ablation process. A strong background continuum is created after the plasma plume formation which does not show features of the atomic emission of interest. Emission lines emerge after the plasma starts to cool down with a substantial time delay of 10's of nanoseconds to microseconds depending on the laser pulse energy. To overcome these issues, dual-pulse LIBS have been proposed, in which the expanded plasma plume is reheated by a second laser pulse with a suitable inter-pulse delay in the range of nanoseconds

[141] to several microseconds [142]. The resulting LOD is typically improved by an order of magnitude. Two different geometric configurations are used in general, collinear and orthogonal. The two laser beams propagate along the same axis in the collinear case whereas they propagate in a perpendicular directions for the case of orthogonal geometry. Angel et al. [138] have reported nearly 40 times enhancement of signal using dual pulse LIBS with respect to single pulse LIBS. They have used two Q-switched Nd:YAG lasers (7 ns, 1064 nm, 100 mJ) in a near-collinear geometry with copper as the target sample.

LIBS has also been combined with other characterization techniques such as Raman spectroscopy. The elemental composition of the target are obtained from LIBS, whereas Raman provides information about the vibrational and rotational energy levels the of molecules. Both of these relatively non destructive laser assisted material characterization techniques can be integrated in one set up. Weins et al. [143] have reported joint analysis by LIBS and Raman techniques at stand-off distances. Remote LIBS and Raman spectroscopy spectra were taken together on a number of mineral samples including sulfates, carbonates and silicates at a distance of 8.3 meter using a frequency doubled Nd:YAG laser.

Another approach to achieving higher sensitivities with LIBS is to concentrate the analyte to be measured prior to carrying out the LIBS probing. In the past the results from a few such sample concentration techniques have been reported. These include the pre-concentration of analytes on a variety of porous substrates, such as paper [144], membranes [145], wood sampling sticks [146], carbon disks and bamboo charcoal. In addition, electrolytic methods can be used to concentrate the metal cations from the aqueous sample to the surface of a metal [147].

Chemometrics, a statistical method, has been emerging as an effective tool in the LIBS community to interpret LIBS data. The use of partial least-squares regression (PLS) and pattern recognition through principle component analysis

(PCA) could improve sample differentiation significantly. Hahn and Omenetto [148] have described the chemometric approach of LIBS in a recent review paper.

2.5 Summary

There has been steady progress over the past decade in the development of LIBS for lateral and depth microanalysis. There is a trade off between the minimum achievable feature size on material surfaces obtained by laser pulses and the corresponding LIBS emission. The capability of reducing the crater size while still giving a detectable LIBS emission signal and an enhancement of the lateral resolution is continually improving over time. The optimization of parameters involved in a LIBS experiment is required to obtain maximum efficiency in surface microanalysis. Depth profiling using LIBS has been demonstrated in the nanometer range as well but this technique has not been able to replace the other established material characterization techniques yet due to its poor detection limit. Several directions are being pursued to reduce the detection limit for LIBS. The processing time, compactness and stand off capability of the LIBS technique make it make it an attractive alternative to other techniques. Further research is still required in order to fully understand the complex laser-matter interaction processes and time and space dependent emission processes. An overview of the important parameters for LIBS, ablation characteristics and emission characteristics in laser-plasma interaction processes has been given in this chapter.

Chapter 3

Experimental Methodologies

In this chapter the background details of the experimental setups and methodologies used in the various experiments will be described. The LIBS experimental setup was modified as needed for each of the particular experiments as explained in different chapters. The basic components of a LIBS system and a few configurations have been described in section 2.1. The other characterization tools used in this thesis were a scanning electron microscope (SEM), optical profilometer and atomic force microscope (AFM). A brief description of these tools and the experimental methodologies applied such as calibration techniques, optical optimization and LIBS signal analysis are outlined in this chapter.

3.1 Characterization Tools

An SEM (Zeiss, Leo 1340) was extensively used during the course of this thesis. Surface images of ablated spots were characterized by this equipment. The instrument has tilt positioning stage with 5 axis controls (X, Y, Z, rotational and tilt stage). The tilt stage controls were used for obtaining images such as cross sectional views of the ablation holes as shown in Fig. 7.11. The resolution of the system was $\sim$ 100 nm. The Zygo optical profilometer is a

non-contact, non-destructive white light optical profilometer for 3-D surface metrology and topography measurements. The depth profile measurements were carried out using this instrument. The thickness of the sputtered metal layers were also measured by this equipment. The vertical resolution of Zygo is 0.1 nm and thus we could measure 7.5 nm thick copper layer as shown in Fig. 5.2. A NanoWizard II AFM (JPK) was used for precise surface analysis such as measuring micron size ablation spots as shown in Fig. 6.2.

3.2 Calibration Techniques

Laser pulse energy calibration, temporal calibration of the gate windows and grating wavelength calibrations are discussed in this section.

3.2.1 Pulse Energy Calibration

Laser pulse energy is one of the important parameters that controls the breakdown, plasma heating, ablation and in turn, the LIBS process. The actual energy delivered to the sample target location together with the spatial distribution was needed to define the material ablation threshold. LIBS spectral emission generally increases as pulse energy increases for a specific setup. The laser output energy varies within a few percent and we have generally used several different pulse energy values in any one experimental campaign. Therefore, an online monitoring system of laser pulse energy for each pulses was required. This was carried out by using calibrated photodiodes monitoring the laser pulses. Two different kinds of photodiodes, EG&G FND100 (silicon) and Hamamatsu R1193U (vacuum), were used in our experiment for 800 nm and 266 nm cases respectively for this purpose. We have used a glass or fused silica wedge to reflect a fraction of the oncoming laser beam to fall on the photodiode. An energy monitor was placed at the target location to measure the pulse energies for calibration purposes. A Spectra Physics Model 407A power meter

was used as an energy monitor. A set of data with varying incident laser pulse energies and corresponding photodiode peak voltages were collected. The calibration plot between pulse energy value at the target versus photodiode signal should be linear. The nonlinearity, if any, comes from exceeding the saturation value of any of the detectors. Fig. 3.1 shows one of the calibration measurements during the experiments. The calibration factor i.e. how much energy delivered at the sample corresponds to how much voltages at the photodiode, was obtained for every single measurements. The calibration factor calculated

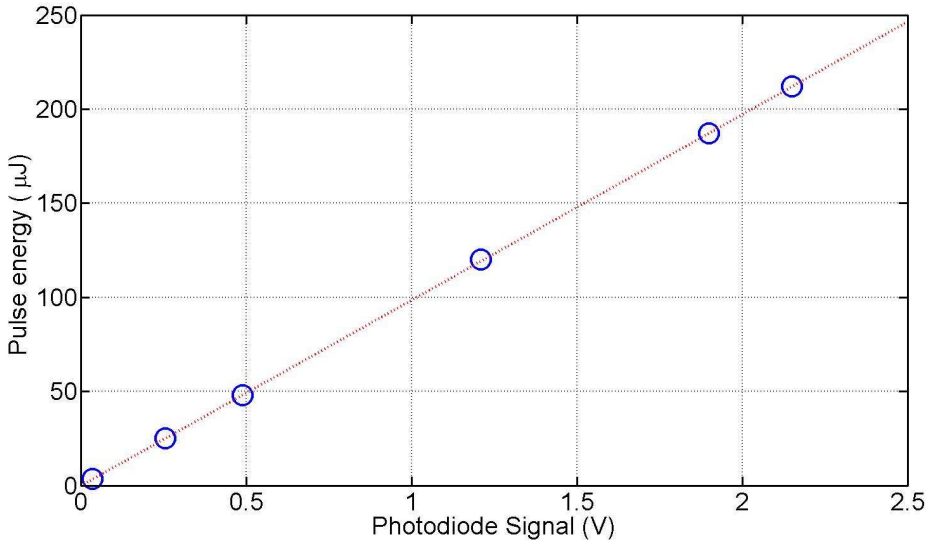

Figure 3.1: Laser pulse energy calibration with a photodiode and an energy monitor.

from the slope of the graph is 98.7 μJ/V. The photodiode voltages for the individual incident laser pulses were monitored and the energy deposited for each laser shot was calculated using the calibration factor.

The lower limit of measuring the pulse energy with our power meter was $\sim$ 1μJ. In some of our experiments, we have worked with pulse energies in the range of few 10's of nJ. We have used a cross calibration technique for this purpose. A combination of a Hamamatsu R1193U UV photodiode (PD1) and a filter was calibrated in the microjoule energy range with an energy monitor first. Then the filter attenuation factor at that laser wavelength was determined.

Thus we can calculate the photodiode (PD1) calibration factor without the filter giving very high sensitivity. Then the calibrated photodiode (PD1) was kept at the target location and another photodiode (PD2) was placed to collect the reflected light from the wedge. The laser pulse energy was reduced to the nanojoule range and the photodiodes were calibrated to each other by measuring at several energy values. The calibration curves of PD1 & power meter and PD2 & PD1 finally gave the calibration of PD2 versus pulse energy on target. The final energy calibrations are accurate to ± 2% for the direct calibrations and ± 6% for the two step calibrations.

3.2.2 Temporal Calibration

The time of arrival of laser pulse at the target location is important as LIBS generally employs a gated window after the laser pulse to acquire the signal when the emission acquisition is optimum and to block the initial continuum emission. In the case of laser pulses with several μJ energy, a gate delay of few 10's of ns is required. The gate window becomes even shorter in the nanojoule regime as the plasma lifetime is reduced substantially.

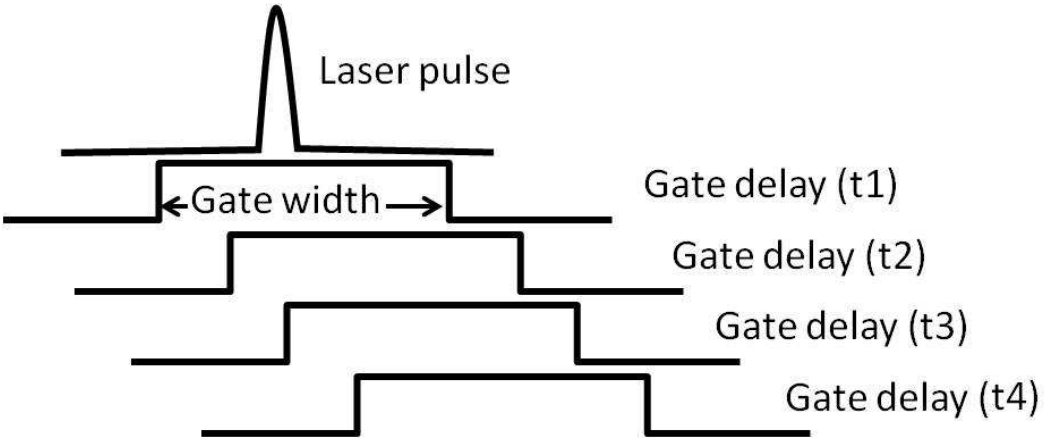

Figure 3.2: Schematic of the variation of gate delay with a fixed gate width for temporal calibration.

In order to set the gate delay we have used a barium sulphate coated plate to scatter the incident unfocused laser light, collected a fraction of the light

and sent it to the ICCD detector. Then we opened the gate for $\sim$ 1 µs and varied the gate delay with a ns step size in a kinetic series mode till the laser pulse disappeared within the time window. A schematic of the variation of gate delay with a fixed gate width is showing in Fig. 3.2. The laser pulse is well within the range of the gate width till gate delay t3 but it is out of the range at t4. Keeping the step size of the gate delay very small, we can precisely obtain the laser pulse arrival. Fig. 3.3 shows the plot of integrated spectral signal versus the gate delay. We used 800 nm femtosecond laser pulses and tuned the grating to capture the laser wavelength. The gate width was 1µs and 30 single shots were taken with 1 ns steps in gate delay between shots. Laser pulse was present till 9 ns which indicates the delay time for the laser pulse to hit the target and prompt emission to be observed in our experimental setup. The temporal calibration was accurate to the order of $\pm$ 1 ns.

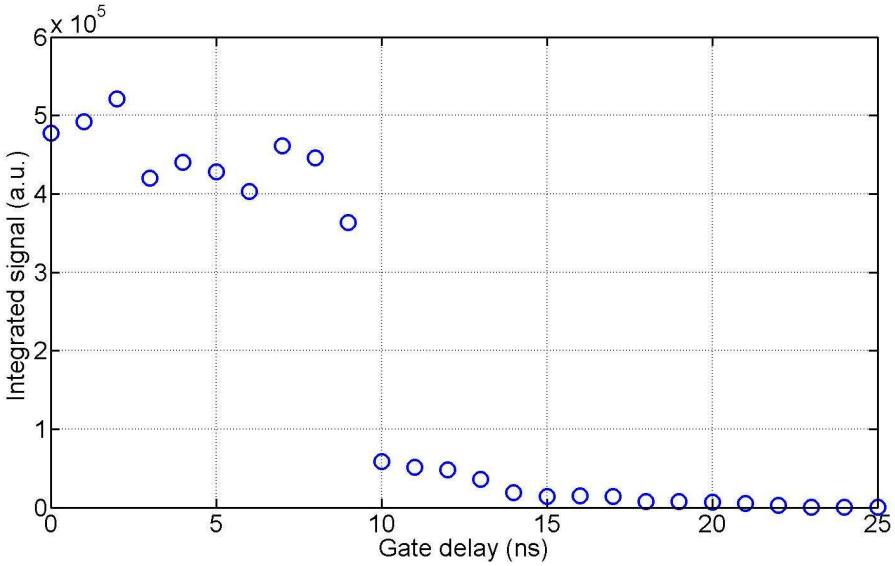

Figure 3.3: Temporal calibration of the laser pulse arrival.

3.2.3 Grating Wavelength Calibrations

The imaging spectrometer (Oriel MS260i) that has been used for this thesis provides an option to choose any of the three gratings installed inside. A

central wavelength can be chosen through the hand controller attached to the spectrometer. The dispersed light from the grating is analyzed at the ICCD. Depending on the spectral resolution needed for any experiment, the gratings could be selected accordingly. We have 150 lines/mm, 1200 lines/mm and 2400 lines/mm grating in our spectrograph. In order to analyze the spectral signal, the wavelength calibrations with respect to a known calibration standard is required in analytical spectroscopy. We have used an Hg lamp (Oriel 6035) to obtain the wavelength calibration. Sansonetti et al. [149] have calibrated the Hg lamp in detail and we have taken those wavelengths values as references. Fig. 3.4 shows the calibration measurement with grating (150 lines/mm) as a function of channel numbers versus wavelengths. The cental wavelength used in this case was 303 nm.

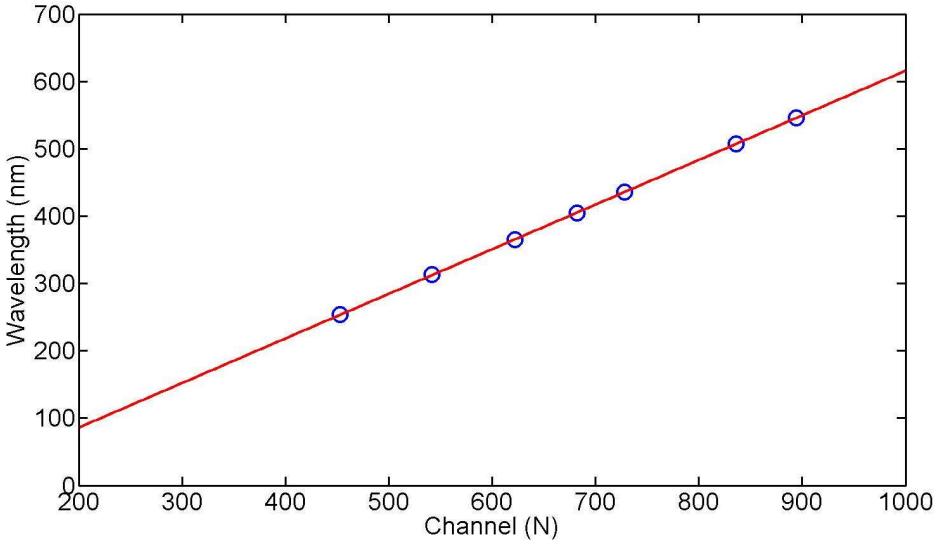

Figure 3.4: Wavelength calibration for the 150 lines/mm grating with central wavelength 303 nm.

Seven Hg line wavelengths with corresponding channels numbers were plotted and a linear fit to the data set was obtained. The calibration equation from the fitted line was λ = (-46.70±0.22) nm + (662.8±0.32 pm) . $N_{channel}$. The same calibration procedure was repeated for the other gratings used for measurements. The resulting wavelength calibration is thus accurate to the

order of ± 0.5 nm for the 150 lines/mm grating. We have mostly used the grating with 1200 lines/mm for which the wavelength calibration was accurate to ± 0.1 nm.

3.3 Focal Position Optimization

In order to focus the laser light on target we have used focusing optics (lens, reflective objective, microscope objective) with different working distances such as a 10X (N.A. 0.28) Mitutoyo objective which has a working distance of 33.5 mm and a 40X (N.A. 0.8) UV Partec objective which has a working distance of only 0.8 mm. The working distance is the distance between target plane and the exit face of the focusing optics. Maximum energy fluence and minimum focal spot area can be obtained if the sample is at the focal position. Therefore, focal position alignment is one the critical optimization steps especially in experiments where we need sub-micron focal spot widths. Two methods were used during focal position optimization.

3.3.1 Optimization Using Emission Signal Intensity

The emission signal from the laser induced plasma will be maximum at the maximum energy fluence. We have changed the focusing optics position with respect to the target and obtained the emission spectrum with single shot laser pulses. The position of the peak signal intensity was taken as the best focal position. The sample was kept at the focal position during the period of an experiment. We have also used an imaging system to image the target surface by keeping the sample at the focal position and tracked whether the target was at focus for all measurements. The accuracy of determining and maintaining the target at the focal position was ± 10 μm for the 10X objective.

3.3.2 Optimization Using Pulse Energy & Sample Control

We have worked with very low pulse energies and very small working distance objectives. Optimization using the emission signal intensities at low laser pulse energies was always difficult as the signal levels were very low. Therefore, in these cases we have opted for a different approach. We used sufficient pulse energy in a burst mode to create an ablation mark on the sample by varying the sample position and observing the image of the surface. Then we decreased the pulse energy to a minimum value where no ablation on the target surface was visible. In this procedure we had to scan through areas of target positions. The imaging optic was then fixed at the position of the minimum ablation threshold energy. We took a number of single shots by sweeping the target plane several microns on either side of the focal plane. The images were analyzed using an SEM and we verified the focal spot position by checking the minimum focal spot diameter. An optical viewing system imaging the target surface through the laser focusing optic was essential in this case to keep the target sample at focus from shot to shot during the measurements. The accuracy of final axial positioning at best focus was estimated to be $\pm$ 0.5 μm for the 40X UV objective.

3.4 Focal Spot Measurements

In the course of the experiments, focal spots measurements were required for analyzing the focusing optics as well as determining energy fluence. An image of the focal spot was obtained by using a higher numerical aperture value objective as an imaging objective to produce a magnified spot image and a camera that can capture the image. The energy density entering to the CCD should be smaller than the saturation limit of the camera. A schematic of the arrangement is shown in Fig. 3.5.

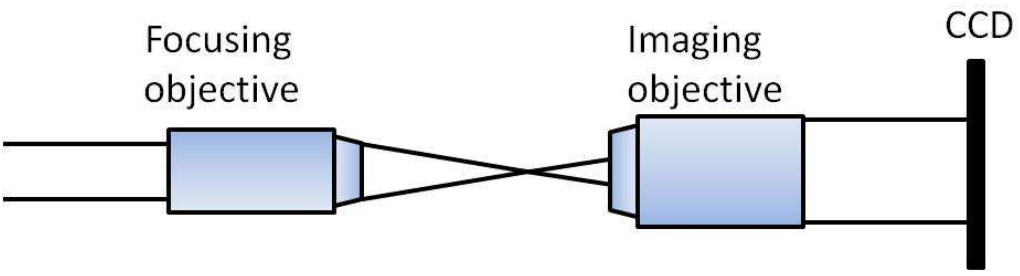

Figure 3.5: A schematic of the focal spot imaging setup.

In most of our experiments we have used Chameleon USB 2.0 camera (Point Grey Research). The effective pixel size of the image on the CCD was calibrated and the final focal spot profile was obtained. The pixels were calibrated by imaging patterns with known widths and sizes. An example of a focal spot measurement is shown in Fig. 3.6. We have used a 10X Mitutoyo objective to focus the 800 nm laser pulses and imaged with a 50X objective in this case. This objective was used for experiments described in Chap. 7.

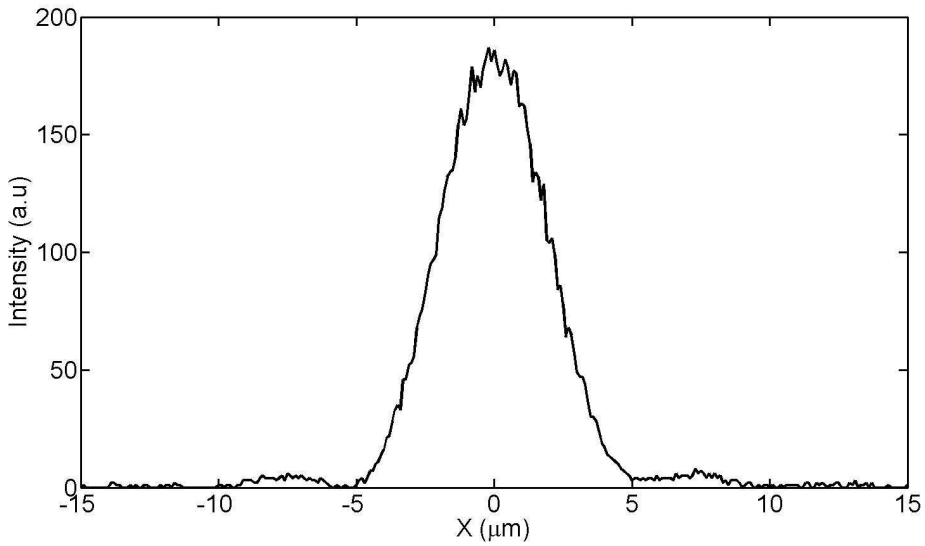

Figure 3.6: Focal spot intensity profile obtained with a 10X objective and imaged with a 50X objective. The FWHM of the spot is 4.7 μm.

3.5 Plasma Imaging

The optimum use of the plasma light in measuring the emission spectrum requires effective plasma imaging onto the entrance slit of the spectrometer. The size of the plasma depends on the laser pulse energy and background conditions. We have used two off-axis parabolic mirrors to image the plasma at the entrance slit as shown in Fig. 3.7. The plasma image was scanned axially across the entrance slit and corresponding emission intensity of the target species was recorded. The slit size are normally smaller than the plasma size and the peak emission position of the scan was chosen for the experiments.

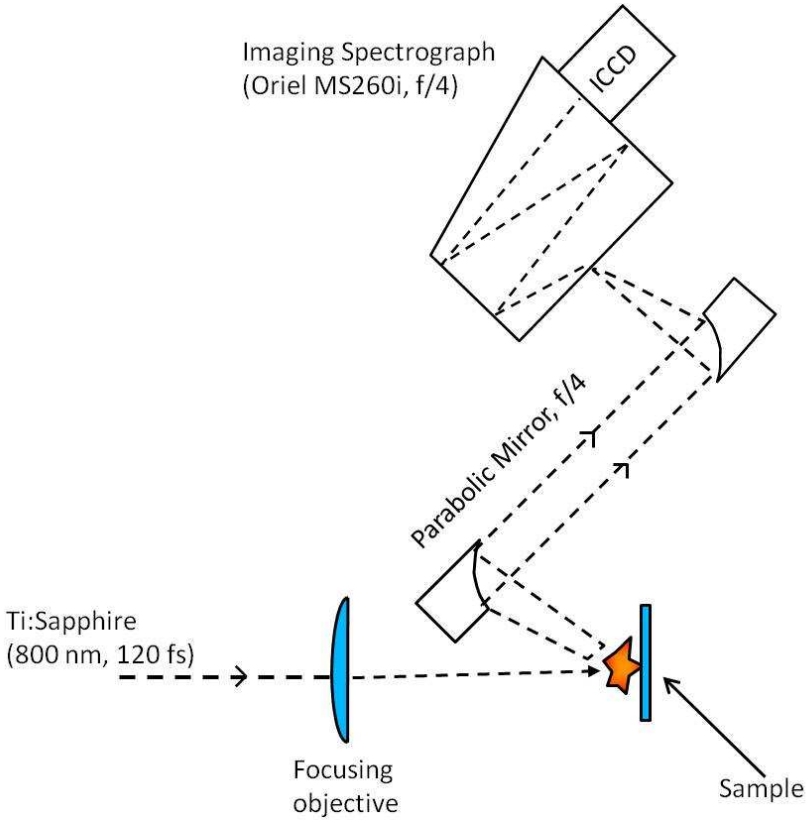

Figure 3.7: Schematic diagram of one of the experimental setups used for plasma imaging.

Another technique was to image the plasma directly onto the ICCD while keeping the wavelength selection at $\lambda = 0$ on the wavelength controller. The grating was basically used as a mirror at zero order and we obtained the direct

image of the plasma. The entrance slit width was normally set at maximum width to capture the whole plasma at the CCD. The plasma image was placed at the center of the slit and then the slit widths were chosen according to the demand of the experiment. For very low pulse energy experiments, we normally have kept the slit wider in order to obtain better signal strengths.

Images of the plasma plumes in the nanojoule ablation regime described in Chap. 6 were obtained directly at the ICCD with the help of a 10X objective. The pixel calibration at the ICCD were carried out by imaging the sample edge and moving the edge with known horizontal displacements. Thus we obtained images of the edge at different pixel locations and calculated the effective pixel imaging dimension for that experiment.

3.6 Analyzing LIBS Signal

Analysis of the LIBS spectrum is required to extract the qualitative and quantitative information from the data obtained. The technique used to subtract the background and assess the background noise for a given spectral line is illustrated in Fig. 3.8. The first order correction of the LIBS signal was to subtract the background. The background noise comes from the detector system as well as the continuum emission at the time of acquisition of the emission signal. Signal to noise ratio (SNR) determines a quantitative value that defines the relative strength of a given LIBS signal versus the noise floor as explained in Chap. 5.3. Optimum, i.e. the largest value, of the SNR is found by the optimization of gate delay while measuring the SNR for a given emission line. In order to acquire the single shot instrument background, we usually took a shot while blocking the laser path so that no plasma was formed and obtained the signal with unaltered experimental settings. This background signal was then subtracted from the single shot LIBS signal. In order to represent a particular spectral line height, we have normally subtracted an average of

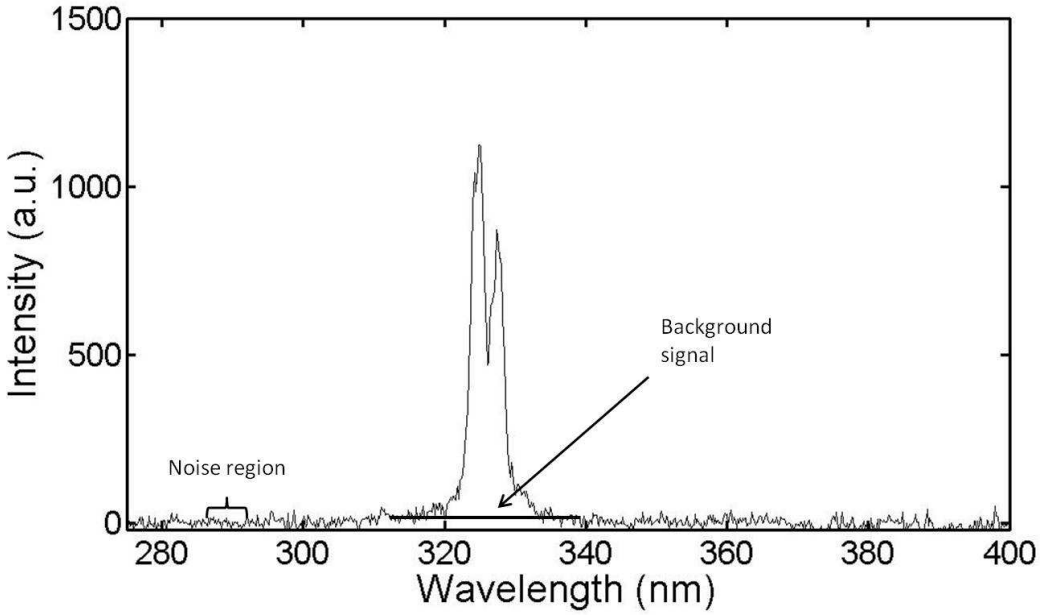

Figure 3.8: Outline of the signal analysis technique.

the nearby continuum emission regions of both sides of the line. This was valid when there was no other spectral line near the line of our interest. The strength of a given emission line was then given by the integrated area under the peak after background subtraction.

Chapter 4

Single Shot Ablation Threshold of Chromium Using UV Femtosecond Laser Pulses*

The single shot ablation threshold for thin chromium film was studied using 266 nm, femtosecond laser pulses. The ablation threshold was determined by measuring the ablation crater diameters as a function of incident laser pulse energy. Absorption of 266 nm light on the chromium film was also measured under our experimental conditions and the absorbed energy single shot ablation threshold fluence was 46±5 mJ/cm^2. The experimental ablation threshold fluence value was compared to time dependent heat flow calculations based on the two temperature model for ultrafast laser pulses. The model predicts a value of 31.6 mJ/cm^2 which is qualitatively consistent with the experimentally obtained value, given the simplicity of the model.

* The main results of this chapter have been published in Ref. [150]. They are reproduced here with permission.

4.1 Introduction

Precise ablation on the sub-micron spatial scale can be achieved by combination of femtosecond laser pulses in the UV wavelength range [151] with tightly focused beams. Information on ablation thresholds for metals and semiconductors is very important in this regime, defining the onset of changes in the target surface morphology. Chromium is a useful material for its high hardness, corrosion resistance, relatively high melting point and ease in coating onto surfaces. It is used for surface coating [152], lithography [73], MEMS [153] and other applications. Chromium is often used in nanotechnology as adhesion layer for gold on dielectric substrates. Chromium thin films have also been used in studies of Laser Induced Breakdown Spectroscopy (LIBS) [154, 155] and for producing submicron craters [136]. For all such applications it is important to understand the ablation process and have an accurate value for ablation threshold fluence. For chromium, the existing reports on ablation threshold fluence are somewhat limited and also are somewhat discrepant. S. Nolte et al. [62] have given the measured laser threshold fluence for 100 nm chromium layers on quartz substrates as 70 mJ/cm^2. This was determined in conjunction with their work on nanostructure formation with a scanning near field optical microscope using 100 fs, 260 nm laser pulses. However, no details are given of how this was measured or the accuracy of the measurement. Using the values of the refractive index $n = 0.86$ and the extinction coefficient $k = 2.17$ [156] at 260 nm, we get absorption value of 42% at normal incidence. Therefore one would estimate an absorbed ablation threshold fluence of 29 mJ/cm^2. J. Kim and S. Na [157] have estimated the ablation threshold laser fluence for 200 nm to 500 nm chromium films as 60 mJ/cm^2 with 220 fs (FWHM) laser pulses operating at 800 nm. At 800 nm the expected reflectivity of pure chromium would be 63% and thus the corresponding absorbed threshold ablation fluence would be 22 mJ/cm^2. This would be lower than that reported by Nolte et al.

[62] but in neither case was the actual measured reflectivity of the sample given. Generally, thin films will have higher absorption than the expected pure metal value for a given wavelength due to minor impurities and imperfections in the coating process and thus the real absorbed threshold fuences could be higher than these estimated values. Working in the UV wavelength [158, 159, 160] range enables much smaller sub micron focal spots and at the same time leads to enhanced absorption of laser pulse energy on most target materials including chromium. Such conditions would be optimal for carrying out high precision material processing or micromachining with ultrafast lasers. Therefore it is important to investigate the ablation threshold in detail for chromium films using UV, femtosecond laser pulses. Characteristics of micro-plasma plumes generated by UV, femtosecond laser pulses in the ablation threshold regime with thin chromium film as the target sample have been reported earlier [161]. In the current investigation we study the ablation threshold fluence of chromium thin film using single shot 266 nm, femtosecond laser pulses. In order to obtain the absorbed energy threshold fluence we also measured the actual absorption coefficient of the thin films at 266 nm. A two temperature model using similar parameters as in the experiment was then used to calculate the expected absorbed ablation threshold fluence and compared to the measured value.

4.2 Experimental

The experimental setup used for this experiment is shown in Fig. 4.1. A Ti:Sapphire (Spectra-Physics Hurricane) laser was used for our study to generate $\sim$ 120 fs (FWHM, assuming a Gaussian pulse shape) pulses at 800 nm with the maximum energy $\sim$ 600 μJ. We have used a half-wave plate and a Glan polarizer to control the output laser pulse energy. Part of the main pulse was then frequency doubled to 400nm by using a BiBO (Bismuth Borate) nonlinear crystal. The maximum pulse energy obtained for the 400 nm pulse was

$\sim$ 120 μJ. We generated a frequency tripled laser pulse of 266 nm by the use of an additional BBO (Beta Barium Borate) crystal through mixing of the 800 nm and 400 nm pulses under phase matched conditions. The pulse width of the final 266 nm laser pulse was estimated to be 170 fs (FWHM). The output from the third harmonic crystal (BBO) contains contributions from the source 800 nm pulses and the second harmonic 400 nm pulses. Dichroic mirrors and spatial filtering of the final pulse was employed to get rid of unwanted wavelength contributions in the beam and transmit only the main peak of the 266 nm pulse. We have used a quartz lens of focal length 1 meter to focus the beam through a 40 μm diameter pinhole and another 1 meter quartz lens to recollimate to give a parallel beam. The incoming 266 nm beam had a spatial diameter of 6.3 mm ($1/e^2$ intensity diameter) which would give a diffraction limited spot of 54 μm ($1/e^2$ intensity diameter) at the pinhole. Contributions from the 800 nm and 400 nm radiation were filtered out by using nine 266 nm mirrors at 45 degrees in the laser path. For this experiment we measured the diameter of the ablation crater as a function of laser pulse energy. The beam was focused onto the target sample using a plano convex fused silica lens with 10 cm focal length. Energy delivered to the sample was calibrated using a photodiode cross calibrated against a Spectra Physics model 407A power meter and monitored for every setting of pulse energy in the experiment. The targets were mounted in a commercial 2-D computer controlled precision micropositioning linear translation stage (Physik Instrument M-111.1DG PI stage) which translated perpendicular to the laser axis. A CCD camera (Point Grey Chameleon USB camera) in conjunction with an f = 15 cm achromatic lens viewing through the laser focusing lens was used as a sample viewing system to make sure that the sample surface was at the focus of the input beam. We have used a thin uniform layer of chromium (500 nm) that was deposited on top of a premium Silicon wafer as our target sample. We have prepared the sample using a planar magnetron sputtering system. The diameter of the ablated spots

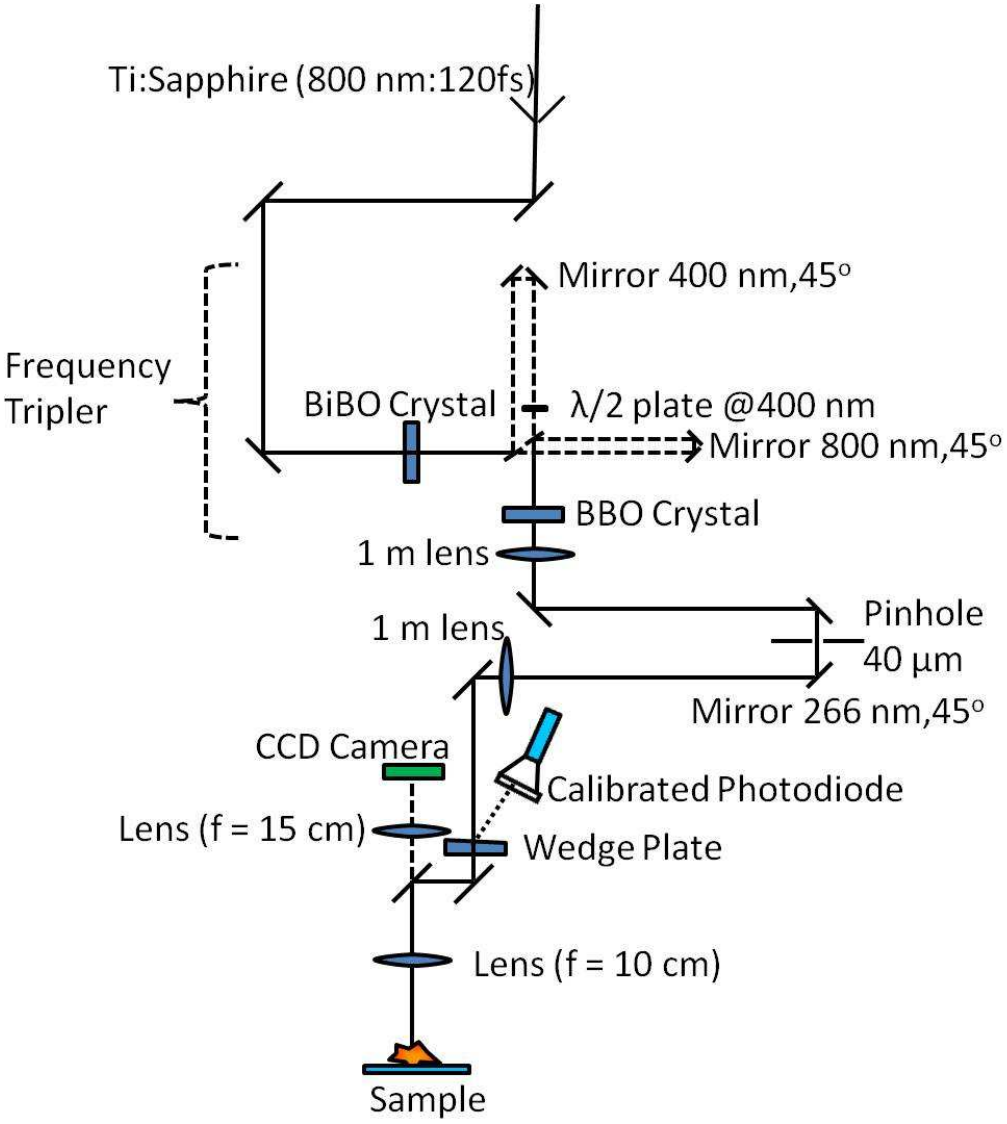

Figure 4.1: Schematic of the experimental setup

was characterized using a Scanning Electron Microscope (SEM) and white light optical profilometer (ZYGO).

4.3 Determination of Single-shot Ablation Threshold for Chromium

The single shot ablation threshold of chromium has not been investigated in detail in the femtosecond laser pulse regime for the case of UV wavelengths. The technique we have adopted to determine ablation threshold has been used by various authors in past [162, 163] which depends on the measurement of Gaussian beam spot sizes [164] at various energy fluences. For a Gaussian beam profile it can be shown [164] that

$$D^2 = 2{\omega_0}^2 ln\left(\frac{\phi_{pk}}{\phi_{th}}\right) \tag{4.1}$$

where D is ablated crater spot diameter, ω_0 is the e-folding electric field amplitude beam radius for a Gaussian beam spot, ϕ_{pk} is the peak energy fluence and ϕ_{th} is the threshold energy fluence where surface morphology of the target sample changes. Fig. 4.2 shows a typical image of the single shot ablated spot region and the measured diameter for the ablation spot using laser pulse energy of 0.56 μJ. We have taken the outer diameter of the crater as D for our calculation. Thus, ablation in this case is indicated by the first onset of single shot surface damage. Ablation diameter increases with laser pulse energy.

We have measured ablation spot sizes from high to low values of laser pulse energy by means of SEM and ZYGO profilometer measurements. We have taken three sets of data at each energy for calculating the experimental error. Fig. 4.3 shows a plot of squared diameter of the ablation spot versus the logarithm of the applied laser pulse energy for our experiment. The ratio of fluences in Eq. 4.1 can be replaced by the corresponding laser pulse energy

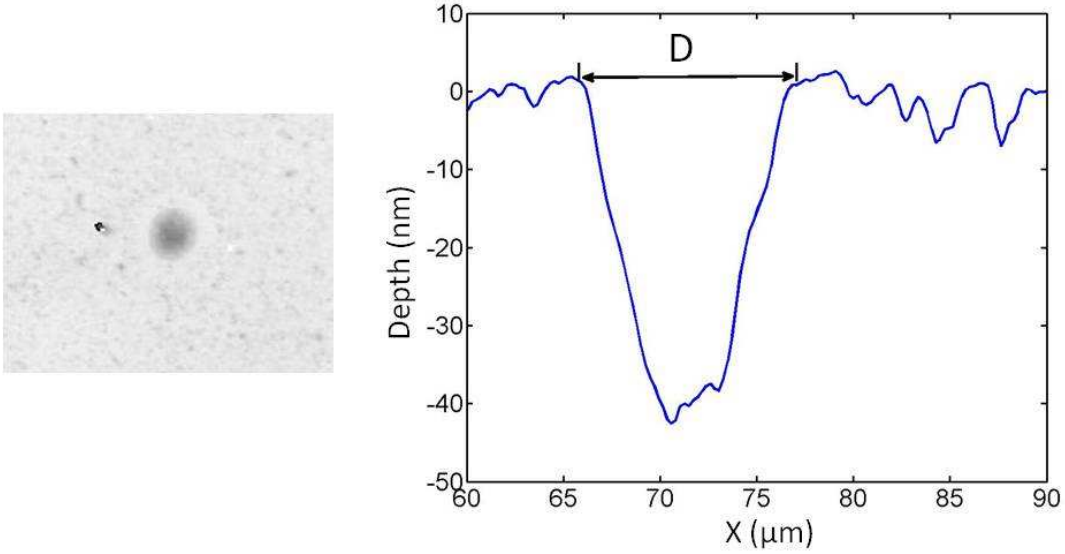

Figure 4.2: Typical single shot ablation crater with laser pulse energy 0.56 μJ. Image of the ablated surface (left) and cross sectional view of the ablation hole (right).

values and we can make a linear fit to the data-set. The slope of the linear fit gives the value of the Gaussian beam waist size, ω_0, and the pulse energy value at $D^2 = 0$ gives the threshold ablation energy, E_{th}. The ablation threshold fluence, ϕ_{th}, can then be calculated using

$$\phi_{th} = \frac{2E_{th}}{\pi {\omega_0}^2} \tag{4.2}$$

The measured single shot ablation threshold fluence was 77±8 mJ/cm^2.

4.3.1 Reflectivity Measurements

Knowledge of reflectivity of the target material at the incident laser pulse wavelength is important in order to calculate the absorbed single shot ablation threshold fluence for a given material. The theoretical absorption of a pure chromium surface at 266 nm is 0.41 [156]. However a coated thin film will normally have a different effective value of absorption depending on the coating procedures. Two different measurements, specular and total scattered reflectivity of the thin Cr film were carried out. The experimental setup used

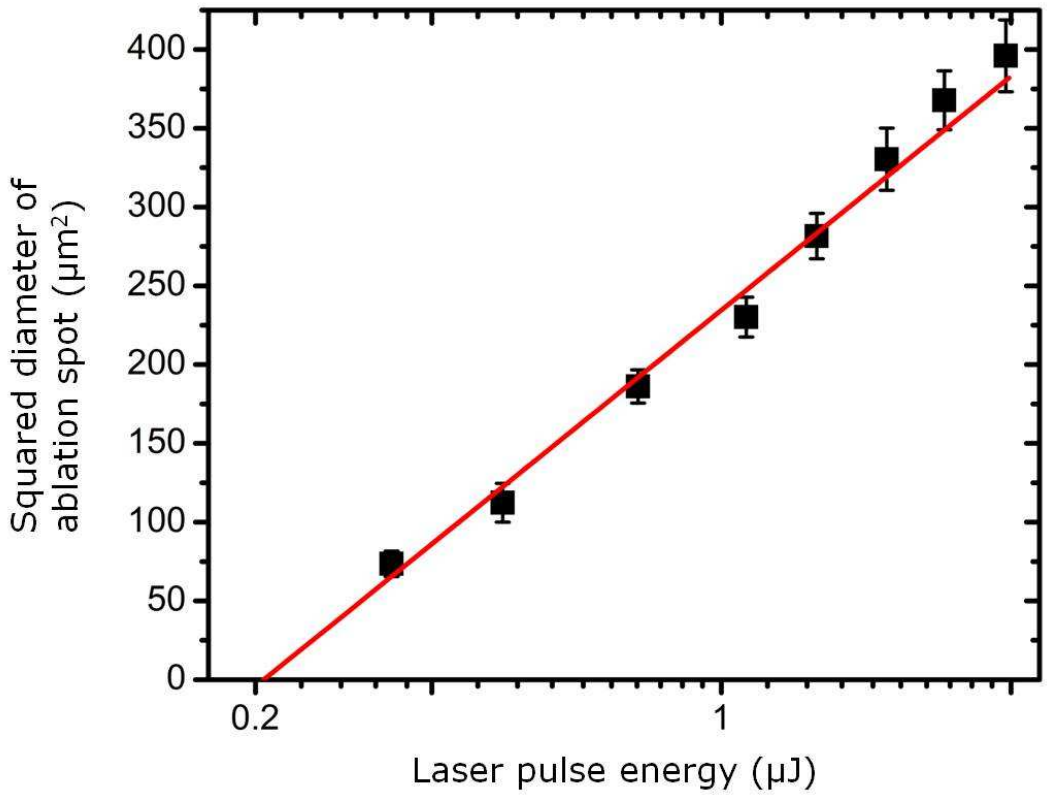

Figure 4.3: Squared ablation diameter versus laser pulse energy for the laser produced craters. The straight line curve is fit to the data using a weighted least square fit.

for specular reflectivity measurement is shown in Fig. 4.4(a). An unfocused 266 nm very low fluence laser beam was used as the illumination source. The percentage of reflection from the quartz slide and attenuation factor of the UV filter was measured for the laser beam used. The sample was kept at an angle of 3^o with respect to the oncoming laser beam path. A calibration curve was generated between the detector (D1) and the incident energy at the position of the sample by placing the powermeter instead of the sample and calibrating with different values of input pulse energy. The reflectivity was measured by placing the sample in position and measuring specular reflected power along with input energy measured by detector D1. The reflectivity was $\sim$40%. In order to account for the scattering losses, the scattered power was measured as per the configuration shown in Fig. 4.4(b).

The photocathode area of both the photodiodes (D1 and D2) were known. Scattered signals at different angles (θ) were recorded. A fitted curve for θ = 0 to 90^o was calculated and all the scattered radiation was integrated over a 2π solid angle to give the scattered light fraction. The scattering losses were of the order of fraction of a percent which was added to the direct specular measurement and thus, the 500 nm chromium film gave a measured total reflectance of 0.40$\pm$.02. Therefore, the measured absorption for our chromium film at 266 nm was 0.60$\pm$.02. The final absorbed single shot ablation threshold fluence value was thus 46$\pm$5 mJ/cm^2 incorporating this measured reflectance value.

4.3.2 Discussions

The ablation threshold value depends on the laser parameters [165, 166], the properties of the material being investigated and to some extent the exact property measured to define the ablation threshold. Formation of laser induced plasma at the surface of the material requires that the incident absorbed energy fluence exceeds the ablation threshold which can be written in a simple form

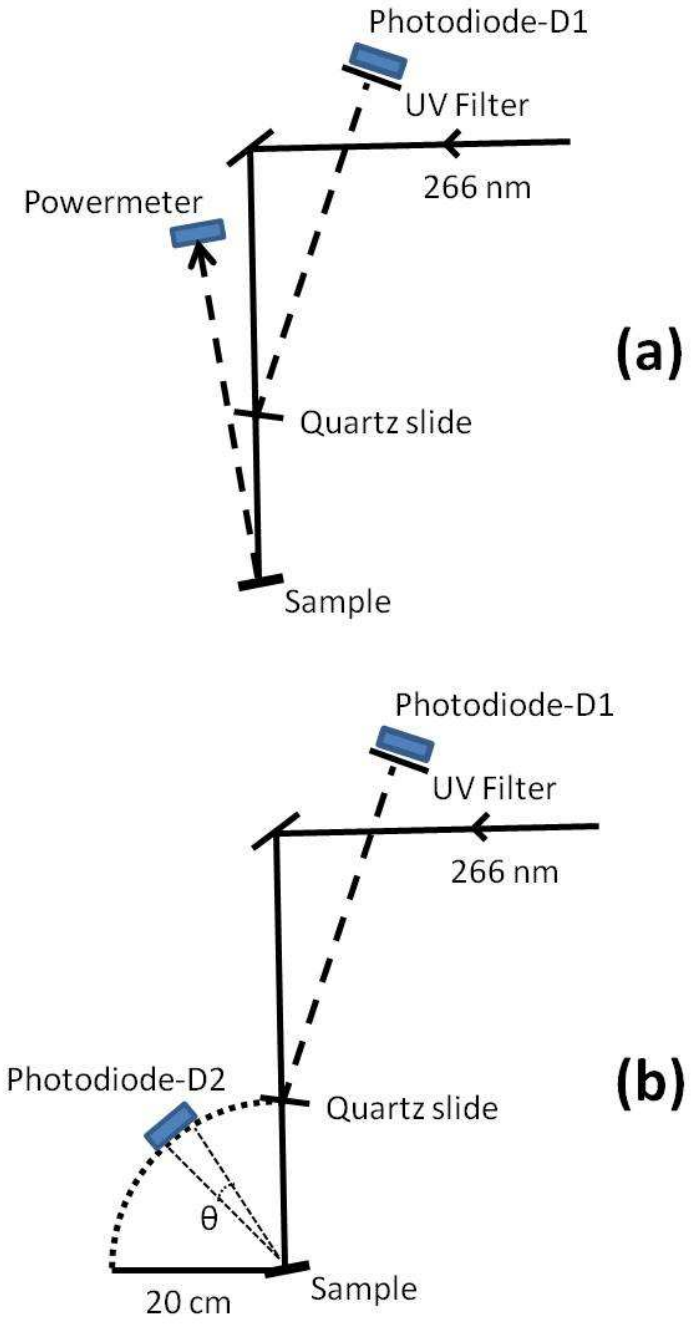

Figure 4.4: Experimental setup measuring the total scattered reflectivity from a sputtered chromium surface with laser wavelength at 266 nm.

[167] as

$$\phi_{th} = \rho L_v a^{1/2} {t_e}^{1/2} \tag{4.3}$$

where ρ is the sample density, L_v the latent heat of vaporization of the target, a is the thermal diffusivity of the target and t_e is the laser pulse width. This equation shows femtosecond laser pulses have much smaller threshold fluence than pico/nanosecond laser pulses and thus are more effective for precise material ablation. This Eq. 4.3 is valid when the diffusion length is greater than the skin depth. The extinction co-efficient of chromium at 266 nm is 2.24 [168]. Thus the skin depth can be calculated as 9.45 nm whereas the diffusion length is $\sim$ 2 nm within the 170 fs pulse duration. Therefore the term $a^{1/2}{t_e}^{1/2}$ can be replaced by the skin depth value our laser wavelength. If we insert values of this skin depth, $\rho = 7.1$ g/cm^3 and $L_v = 6580$ J/g for chromium [169], we get $\phi_{th} = 44$ mJ/cm^2. This ablation threshold value for chromium is comparable with our experimentally obtained value.

Several methods have been reported by different authors for the determination of ablation threshold fluence for materials. Measurement of laser-induced ablation of aluminum films was demonstrated using simultaneous observation of optical diffraction and acoustic signals [170]. A probe beam deflection technique has been used by Petzoldt et al. [171] to find ablation thresholds for different metals. One of the common method to determine ablation have been by measuring the depth ablated per pulse, d, given by,

$$d = \frac{1}{\alpha} ln \left(\frac{\phi}{\phi_{th}} \right) \tag{4.4}$$

By knowing the effective penetration depth $\frac{1}{\alpha}$, incident peak energy fluence (ϕ) can be plotted against the ablation rate (d) and an extrapolation method can be used to find ablation threshold fluence ϕ_{th} [172, 173]. This method applies to cases where crater depth from multiple laser pulses are measured and ablation depth per pulse is calculated. In the procedure to calculate the abla-

tion threshold value from ablation rate studies, reflectance of the target surface changes for successive shots as the surface morphology changes with each laser pulse. Absorption of laser pulse increases as the surface roughens from successive shots and there is incubation of damage.It is known that multi-shot damage thresholds decrease with the number of shots due to the incubation of microscopic damage in the material structure [162, 174, 175]. Our measurement of threshold energy fluence value was obtained from single laser shots on fresh surfaces and therefore, the absorption co-efficient for the sample at 266 nm is expected to be close to that of the original surface though a small change might be expected as the electron distribution function heats up before ablation occurs. In general, we expect to obtain a higher ablation threshold value when compared to multi-shot damage threshold.

4.4 Two Temperature Model

Interactions between femtosecond laser pulses with metals and the corresponding material heating phenomena have been successfully studied quite often using a one dimensional two temperature model (TTM)[176, 177, 178, 179]. In order to calculate the expected ablation threshold fluence for chromium, we have used the two temperature model. Properties and mechanisms inside the material can be modeled on a small spatial and temporal scale by TTM. This model predicts the temporal and spatial evolution of the electron temperature (T_e) and the lattice temperature (T_l) by solving a coupled set of one dimensional differential equations,

$$\begin{aligned} C_e\frac{\partial T_e}{\partial t} &= \frac{\partial}{\partial z}\left(\kappa(T_e,T_l)\frac{\partial T_e}{\partial z}\right) - g(T_e - T_l) + S(z,t) \\ C_l\frac{\partial T_l}{\partial t} &= g(T_e - T_l) \end{aligned} \tag{4.5}$$

where C_e and C_l are the electron and lattice heat capacities, $\kappa(T_e, T_l)$ is the

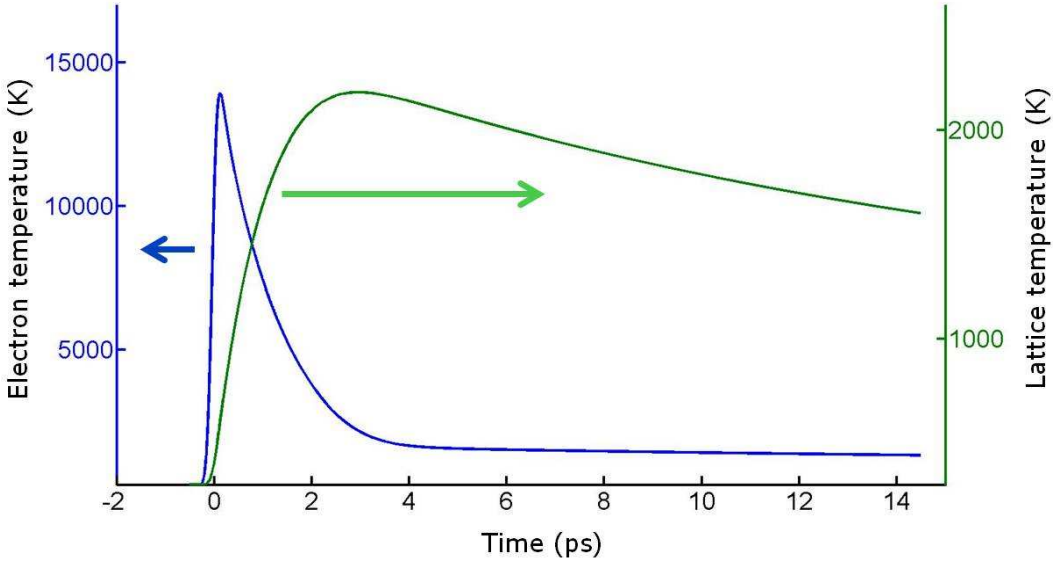

Figure 4.5: Electron and lattice temperatures versus time showing the peak electron and lattice temperatures using the two temperature model for an absorbed laser fluence of 31.6 mJ/cm^2.

electron thermal conductivity, g is the electron-phonon coupling co-efficient and S is the laser heating source function. The Z axis is taken as the normal to the surface plane. The heat diffusion of the electron subsystem is much faster. Therefore, thermal conductivity of the lattice is absent as it is negligible in comparison to electron thermal conductivity.

The melting point of chromium is 2180 K. We have integrated this model in time for different absorbed laser pulse energy fluences for a 170 fs (FWHM) Gaussian temporal profile pulse and obtained the peak lattice temperature at the surface of the chromium target material. The absorbed laser fluence at the threshold for ablation is obtained for the value that heats the surface to the melting temperature of 2180 K. From the TTM calculation a value of 31.6 mJ/cm^2 was obtained where the lattice temperature crosses the melting point. For these calculations values of $C_e = \gamma T_e$ where γ is the Sommerfeld parameter (γ = 194 J/[m^3 K^2] [180]) , C_l = 3.23 $\times$ 10^6 J/[m^3 K] [169], g = 4.2 $\times$ 10^{17} W/[m^{3}K] [181] have been used. The electron thermal conductivity $\kappa(T_e, T_l)$ value was calculated using the general solution provided by Animisov

et al.[182]

$$\kappa(T_e, T_l) = \chi \frac{(\theta_e^2 + 0.16)^{5/4}(\theta_e^2 + 0.44)\theta_e}{(\theta_e^2 + 0.092)^{1/2}(\theta_e^2 + \eta\theta_l)} \tag{4.6}$$

where $\theta_e = k_B T_e/T_F$, $\theta_L = k_B T_l/T_F$, $T_F = 8.01\times10^4$ K is the Fermi temperature, and χ and η are fitting parameters, which are 300 W/[mK] and 0.2 respectively for chromium [157, 183]. This expression is valid for a wide range of electron and ion temperatures.

The purpose of the numerical simulation was to estimate the absorbed laser pulse energy fluence value which would result in a surface temperature of the chromium sample of 2180 K. Fig. 4.5 shows the electron temperature and surface lattice temperature over a period of 15 ps from the onset of the laser pulse for this case. The peak of the electron temperature was 13917 K. The peak lattice temperature 2180.5 K, slightly over the melting temperature of chromium, was reached at 2.95 ps. The electron and lattice temperatures equilibrate at this time. The peak absorbed fluence in this case was 31.6 mJ/cm^2 which defines the absorbed ablation threshold fluence for chromium.

If we compare our experimentally obtained single-shot ablation threshold value of 46$\pm$5 mJ/cm^2 with the value obtained from the TTM, we see that there is approximate agreement. The discrepancy between these two values could possibly be due several factors. One might be that the pulse duration is longer than the 170 fs assumed. We have run the TTM code for 300 fs (FWHM) and 500 fs (FWHM) laser pulse width. The results show negligible variation in peak lattice temperature with a 300 fs pulse duration. Fig. 4.6 shows the electron and lattice temperature variation with time using 500 fs (FWHM) laser pulse duration. The peak of the lattice temperature is 2136 K using the same 31.6 mJ/cm^2 absorbed energy fluence. We need absorbed fluence of 32.2 mJ/cm^2 to reach the melting temperature of chromium. Therefore, the pulse duration does not play a major role in modifying the ablation threshold value. We have varied the electron-phonon coupling co-efficient value g from 4$\times$ 10^{17} to 4.4$\times$ 10^{17} to

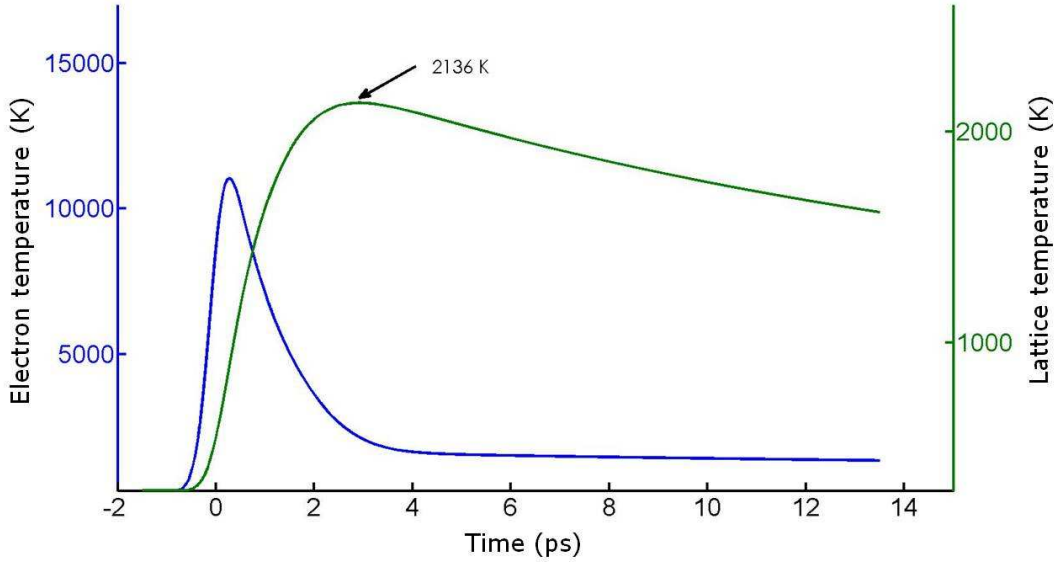

Figure 4.6: Electron and lattice temperatures versus time showing the peak electron and lattice temperatures using the two temperature model for an absorbed laser fluence of 31.6 mJ/cm^2 and 500 fs (FWHM) laser pulse width.

see the effect of g on the variation of peak lattice temperature. The absorbed ablation threshold value changes from 32.2 mJ/cm^2 to 31 mJ/cm^2 respectively in order to keep the surface temperature of chromium at 2180 K. Therefore a much lower value of g than the widely reported value for chromium ($4\times$ 10^{17} W/[m^{3}K]) would be required to change the theoretically obtained absorbed ablation threshold value. The electron distribution function generated could also play a role. If the electrons are ballistic with a range of several nm then they would penetrate more deeply into the solid surface leading to the coupling to more solid lattice material and an increase in the predicted ablation threshold. Another possible contribution is due in part to the failure to include the time dependent change in absorption of the metal during the laser pulse due to the heated electron distribution function. It is known that absorption changes as a function of laser intensity even in the sub threshold regime and tends to approach a value of 50% [184] for different materials. Kirkwood et al. [185] have measured the reflectivity of thin film copper surfaces as a function of increasing fluence. The variation of reflectivity in the range of 100 mJ/cm^2 to 500 mJ/cm^2

is within 5%. Thus, if our measured reflectivity was modified by 5%, we get the minimum absorbed ablation threshold value of 42 mJ/cm^2. Thus it could be that the effective absorption decreases and the calculated absorbed energy is lower than the above estimate which was based on the initial low temperature reflectivity of the surface. Clearly a more detailed analysis with an improved numerical model would be required to resolve this final difference.

4.5 Conclusions

The single shot ablation threshold for a 500 nm Chromium thin film has been studied. The variation of ablation spot diameter has been measured as a function of laser pulse energy and a logarithmic curve fit has been used to determine the ablation threshold. The measured threshold irradiance fluence was 77±8 mJ/cm^2 for 170 fs, 266 nm laser pulses. The absorption co-efficient for the actual target sample at 266 nm has also been measured and used to calculate the absorbed threshold fluence giving an absorbed single-shot ablation threshold fluence for chromium of 46±5 mJ/cm^2. A two temperature model simulation using similar parameters as used in the experiment predicted an absorbed ablation threshold of 31.6 mJ/cm^2 which is comparable to but lower than the experimental value. This discrepancy may be due in part to the changing reflectivity of the sample during the laser pulse which would lead to a correction to the measured value.

Chapter 5

LIBS Single Shot Depth Sensitivity*

It has been observed in the past that the depth and volume that contribute substantially to spectral emission is less than the total ablation crater volume[90, 186] and therefore the scaling of depth sensitivity with laser pulse energy is different than the scaling of ablation depth with energy. In addition, very few photons are emitted compared to atoms ablated for energies of 100 nJ to 100 μJ (120 fs pulse length) i.e the emission efficiency is much less than unity [90]. We expect that highly excited atoms near the surface will emit more strongly than the bulk of ablated atoms. Therefore, the upper layer of the ablated target material forms the bulk of the plasma that emits the spectra. The material below is ablated and forms a crater but contributes much less to the LIBS spectra. Such a non uniform response was observed previously in the detection and mapping of latent fingerprints by LIBS where the thin layer of finger oil blocked the emission from a silicon substrate even though the ablation crater penetrated well into the silicon substrate[20]. The depth dependence of LIBS emission determines the emission response for a given constituent within the

* The main results of this chapter have been published in Ref. [155]. They are reproduced here with permission

ablated depth of one laser shot. In the current experiment different layered targets on silicon wafer substrates were ablated at laser energies from 1 μJ to 100 μJ to determine the depth sensitivity of the LIBS emission or the depth dependence of LIBS emission within a single laser shot. The results demonstrated in this chapter were published in Ref. [155].

5.1 Introduction

Depth profiling using LIBS can reveal the interfaces between different materials at different depths in a layered sample as discussed in Chap. 2.4.1. Multi layer coatings of different material and thicknesses are used in microelectronics industry and it is important to know the location of interfaces between different materials i.e. the depth profile.

Most depth profile mapping of the elemental constituents in LIBS literature assumes a constant rate of material removal per laser pulse and uniform material ablation with each laser pulse. General practice in the determination of depth resolution is to calculate the Average Ablation Rate (AAR)[99, 105, 110, 116, 187] in terms of μm/pulse or nm/pulse i.e. the thickness of the layer divided by the total number of pulses required to reach the bottom of the layer. This AAR is then used to define depth resolution. Depth resolution, $\triangle$z [103], can be defined as the depth range where the signal intensity changes from 16 to 84%, given by

$$\triangle z = N_s \times AAR \tag{5.1}$$

where N_s is the number of laser shots needed to go from 84% to 16% of the normalized signal intensity. This depth resolution gives an estimate of the capability of a LIBS system to resolve transitions in material composition of buried layers for a particular layered sample for a given set of material and laser parameters. The transition of emitted spectra from one layer to another

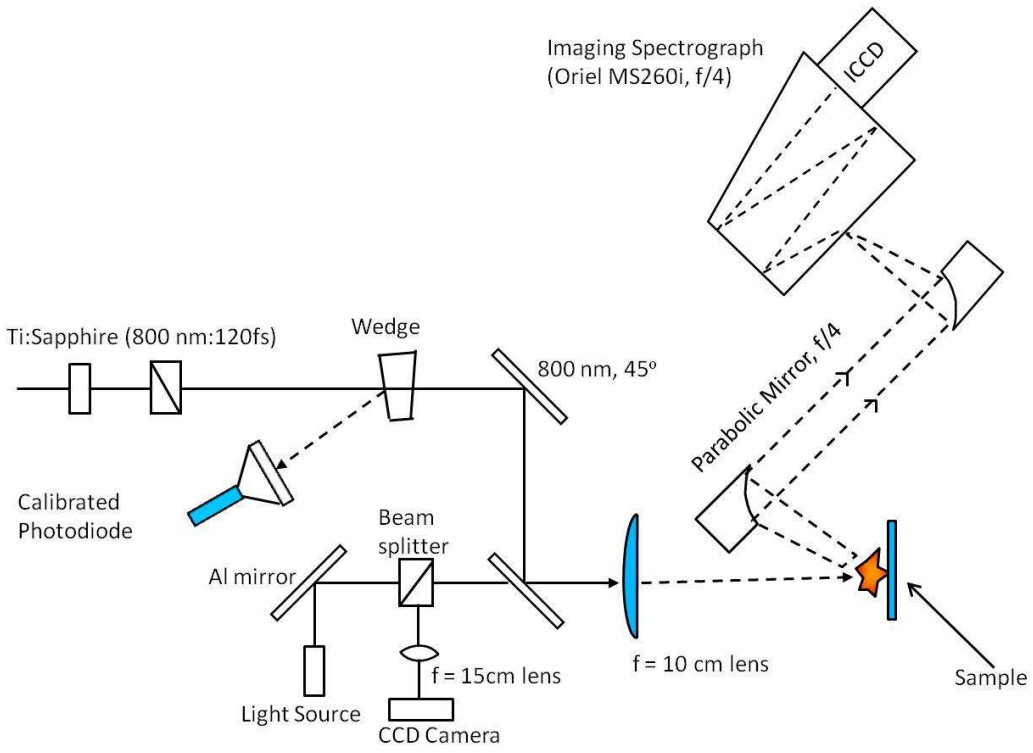

Figure 5.1: Schematic layout of the experimental setup

typically happens over the range of a μm or more [103, 116] for a metallic sample with sharp interfaces. Mixing of layers of different materials because of melting and resolidification during a multiple shot depth profiling also leads to reduced resolution for profiling buried features. Although it is possible to achieve a very shallow ablation depth per pulse such as $\leq$2 nm/pulse[102] the emitted spectra changes slowly over several laser shots and thus the depth resolution can be many times the ablation depth per pulse. For single laser shot ablation the question arises whether the observed spectrum reflects the average composition of all the material ablated or whether materials close to the top surface contribute more to the emission.

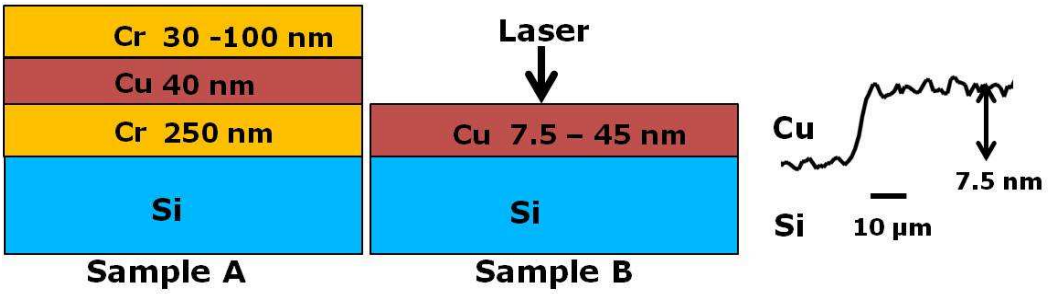

Figure 5.2: Sample A, sample B and ZYGO profilometer lineout scan of sample B at the edge of the 7.5 nm Cu layer on top of the Si wafer

5.2 Experimental

The experimental setup is shown in Fig. 5.1. The maximum energy employed at the target was $\sim$ 200 µJ. The laser pulse had a Gaussian spatial profile and was focused on the sample surface using a 10 cm focal length lens. The laser spot diameter was 13 µm (FWHM). A target-viewing system consisting of a CCD camera and an f = 15 cm achromatic lens viewing through the same focusing objective that focuses the laser beam was used for target visualization and positioning. The LIBS plasma emission was imaged 1:1 onto the spectrometer (Oriel MS260i) entrance slit with a pair of aluminum coated f/4 off-axis parabolic mirrors. A grating with 1200 lines/mm and a 300 µm entrance slit were used for the experiments reported. Spectra were recorded using a gated intensified CCD camera (Andor iStar ICCD). Focal position alignment and alignment of the plasma imaging optics were checked and adjusted for each experiment to confirm similar experimental background conditions. The targets were mounted on a precise XYZ positioning stage. To improve the signal to noise ratio and minimize the effect of laser pulse energy variation, we have taken the average of a large data set (300 shots) for each experiment. To capture all the plasma emission, the image intensifier gate width was set at 1 µs. Optimum gate delay at peak Signal to Noise Ratio (SNR) was evaluated for different pulse energies as described later. Each laser shot was taken on a fresh part of the target surface.

Two different layered samples have been used in this experiment. The first sample, A, was a Cr/Cu/Cr layered target on a silicon wafer with a 40 nm Cu tracer layer buried at different depths (30 nm and 100 nm). The second sample, B, was prepared with a Cu layer on top of a silicon wafer with different Cu layer thicknesses (7.5 nm, 15 nm, 45 nm). Fig. 5.2 shows the schematic of these two samples used in our experiment. Thin uniform layer of materials (Cu/Cr) were deposited using a planar magnetron sputtering technique. Crater diameter and morphology were measured using a ZYGO profilometer (ZYGO New View 5000) and scanning-electron microscopy. Fig. 5.2 shows the typical target sample surface roughness of very thin 7.5 nm Cu layer on top of Si wafer measured by a ZYGO optical profilometer. It shows that the average Cu layer height is ∼7.5 nm. All experiments were conducted at ambient atmospheric air pressure.

5.3 Results and Discussion

To substantiate the effective depth that takes part in the process of spectral emission from the laser produced plasma, we have taken several single laser shot measurements on a single target sample type with pulse energy varying from 1 to 100 μJ and the corresponding depth profile measured using an optical profilometer. Optimization of gate time is important in LIBS experiments as signal and noise levels change according to the timing of acquisition. By varying the gate delay we can optimize the exact time when we have maximum signal to noise ratio (SNR). This varies with laser pulse energy and is critical in low energy cases as optimum delay times fall into the nanosecond range in μLIBS[90]. Therefore, the optimum gate delay time has been evaluated and employed for particular probe experiments at different energies. SNR[9] has been calculated as,

$$SNR = \left(\frac{\Sigma_{i=1}^{N} I(\lambda_n)}{\sigma_{bgsc}\sqrt{N}} \right) \tag{5.2}$$

Where $I(\lambda_n)$ is the background corrected spectrally resolved signal intensity of the emission in wavelength channel λ_n, σ_{bgsc} is the single channel background noise which was measured by calculating the standard deviation of a spectrally quiet region away from the peak for a background corrected signal and N is the number of channels which are summed for the emission line. The SNR is dependent on the emission characteristics of the elements as well as the target matrix. Fig. 5.3(a) shows the measured variation of SNR with gate delay for laser pulse energies between 40 μJ and 90 μJ for Cr and Cu. Each SNR data point is an average of three single shot SNR measurements for this figure. We have used sample A for this experiment with a 30 nm top layer of Cr. A gate width of 1μs was always used to ensure that all emission was collected. At higher energies such as 90 μJ, the optimum gate delay for Cr and Cu are approximately equal but the optimum gate delay for Cr is larger than Cu as the laser pulse energy decreases to 40 μJ. It is observed that optimum gate delay increases with laser pulse energy[9]. This is attributed to the fact that the plasma volume is smaller at lower pulse energy and the temperature decays faster due to the increased surface to volume ratio[188]. Therefore we see that plasma generated at a higher energy takes more time to expand to the optimum conditions of temperature and density for plasma emission. As our prime concern is to detect buried Cu signal under the Cr layer efficiently, we use the calculated optimum gate delay for Cu at any particular energy for our experiments. Fig. 5.3(b) shows the plot of the delay times used vs pulse energy for Cu detection. The optimum gate delays for different pulse energy were determined by the delay times which gave the peak SNR for Cu at that energy.

Next, we have taken samples with different Cr cover thickness and applied different laser pulse energies to obtain information on the intensity of the Cu signals buried at different depths in those samples. We have integrated the Cu signals (324.75 nm and 327.39 nm) from the spectra obtained for the different

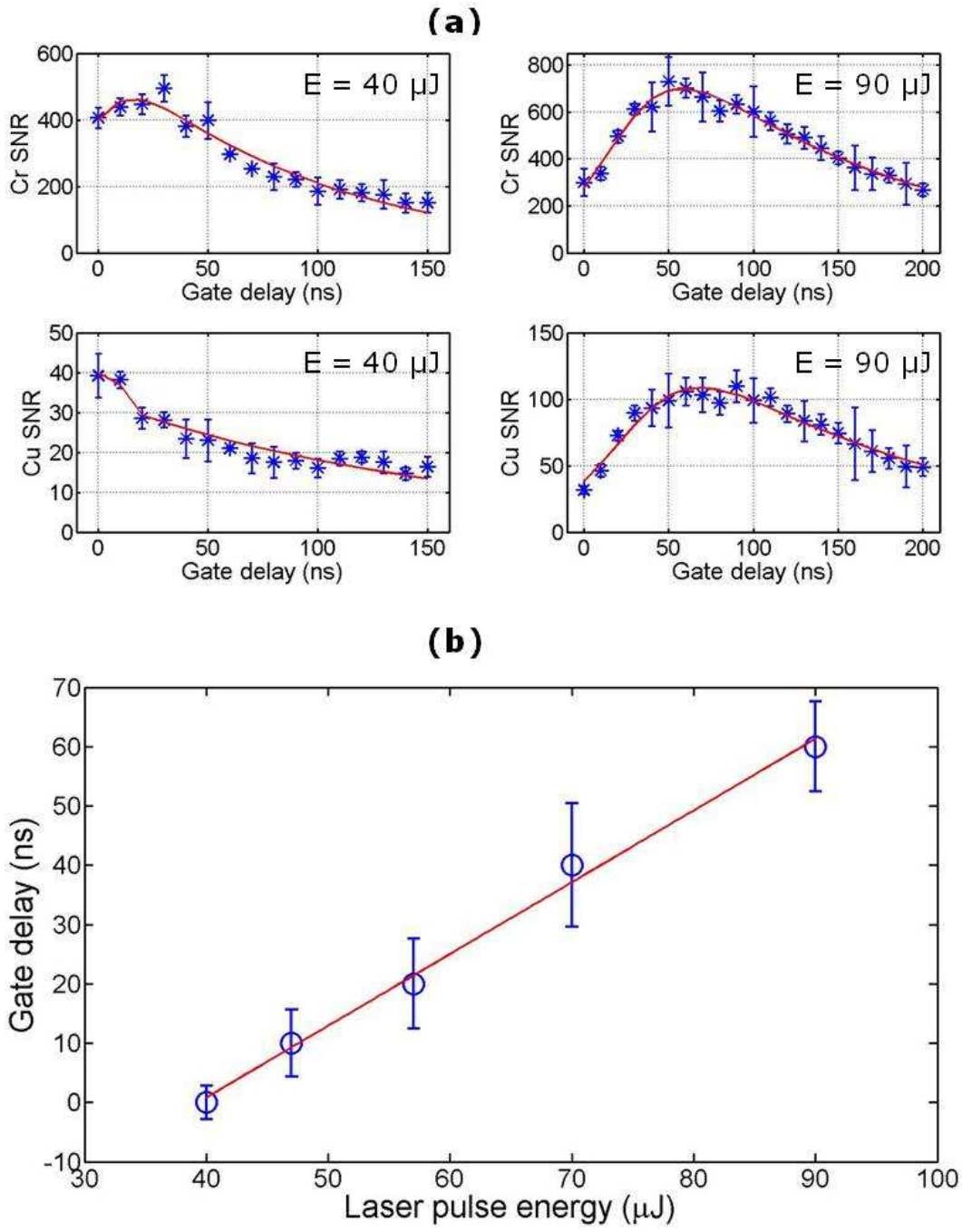

Figure 5.3: (a) Variation of SNR with gate delay for laser pulse energies of 40μJ to 90μJ for Cr and Cu using sample A (30 nm Cr/40 nm Cu/250 nm Cr) and (b) delay times to obtain the peak SNR value for Cu versus laser pulse energy.

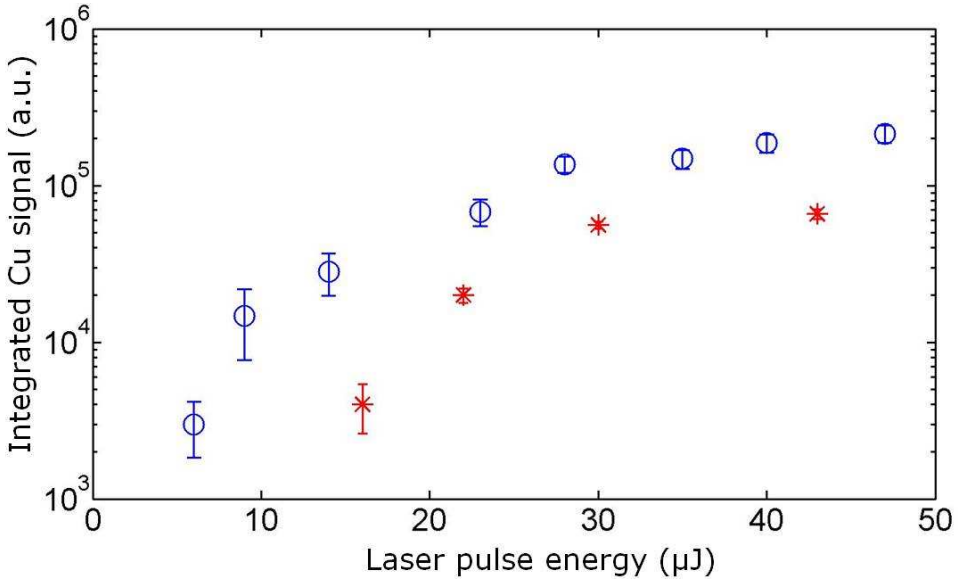

Figure 5.4: Integrated Cu signals for different Cr cover layer thickness ('○' 30 nm, '∗' 100 nm) as a function of laser pulse energy

target samples at different incident laser pulse energy. As target samples have the Cu layer buried at different depths, it is expected that we will observe a stronger Cu signature for a target having the Cu layer closer to the surface. Fig. 5.4 shows the results of two different target samples where the Cu is buried at depths of 30 nm and 100 nm. We have applied laser pulse energies from 5 μJ to 60 μJ for this experiment. The integrated Cu signals have been plotted as a function of laser pulse energies. It is observed that the thicker cover Cr layer requires more energy to excite emission from the hidden Cu layer. The signal becomes less as the layer is deeper for any given energy as expected.

In the case of a 30 nm top Cr layer, the buried Cu layer contributes a much stronger signal in comparison to the thicker top layer sample. This observation reveals that the spectral contribution from a buried layer changes significantly as we go deeper for a single shot spectra. The onset of copper emission spectra changes as well. We have seen that Cu emission started at 6 μJ for the case of 30 nm top Cr layer, whereas, Cu emission starts at 16 μJ for the sample with 100 nm top Cr layer. We also can say that plasma emission volume is dominated by the upper part of the target sample surface. Materials situated

at deeper depths contribute less to the plasma emission. This argument can be established by investigating the sensitive depth region which acts as the source of the emitted spectra. We have chosen 30 nm top Cr cover layered sample to work with for this case. A low energy crater profile with small depth is easy to characterize with profilometric measurements. Craters from laser pulse energies greater than ∼20 μJ had rough bottom profile due to melting and resolidification and thus were difficult to measure. Laser pulse energies varying from 1 μJ to 10 μJ were sufficient to create crater depths of up to 90 nm and we could easily reach the buried Cu layer for the thinner sample. We measured the threshold energy value where we observed the onset of Cu spectral signature and measured the corresponding depth profile. The strength of the Cu signals (324.75 nm and 327.39 nm) at different laser pulse energies were studied. At a very low pulse energy of ∼1.5 μJ the crater depth was only 14 nm. This obviously has not penetrated the top 30 nm Cr layer. As we increase our pulse energy the crater depth increases and penetrates through the top Cr layer to enter into the Cu region. Fig. 5.5 shows the case where we applied pulse energies of 3.5 μJ and 6 μJ. With 3.5 μJ incident pulse energy we did not see any Cu signal from the emission spectra but Cr signal was present as shown in Fig. 5.5(a). Profilometric measurement shows that the ablation crater depth was 55 nm for this case. Appearance of Cu signal started at 6 μJ pulse energy and the corresponding ablation crater depth was 67 nm as shown in Fig. 5.5(b). Hwang et al.[136] have carried out similar experiments to study femtosecond laser-induced plasma characteristics with thin Cr surface layers. In our case with 3.5 μJ laser pulse energy, the relevant energy fluence is 1.8 J/cm^2. The crater depth of ∼ 55 nm at this fluence matches closely with the reported single shot laser ablated crater depth of ∼76 nm for an energy fluence of ∼1.6 J/cm^2[136] in their case.

In order to find out why we do not see any Cu signal although the crater profile shows Cu has been ablated during the ablation process, we can examine

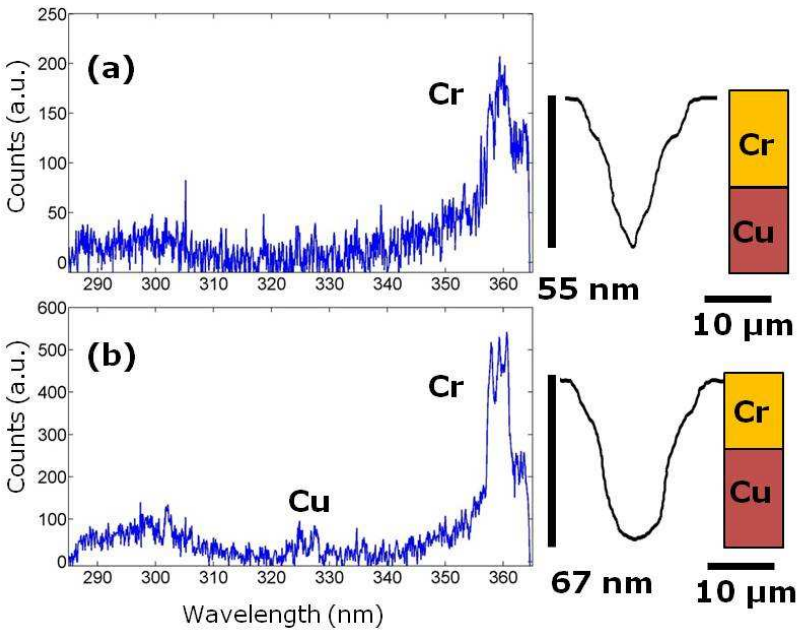

Figure 5.5: Spectra and depth profile for the sample A (30 nm Cr on 40 nm Cu tracer layer) at 3.5 μJ (a) and 6 μJ (b) pulse energy.

how many ablated atoms take part in the process of emitting photons. It has been shown earlier by Taschuk[90] that less than 1 atom in 10^5 emits photon at laser pulse energies $\sim$ 100 nJ and it increases to $\sim$1 atom in 10^3 for pulse energies of 100 μJ. Thus the number of atoms leaving the target in an excited state are far less than those leaving the target as neutrals, liquid droplets or solid fragments. The distribution of these emitted atoms in the ablated volume is important to define depth sensitivity. Quantification of the emitted Cu photons was carried out at different pulse energies. We have calculated the number of Cu photons per Srad liberated from the volume using the following relation,

$$\Phi = \left(\frac{N_{counts}}{R \times T \times QE \times \Omega} \right) \tag{5.3}$$

where Φ is defined as the Cu photons per Srad per shot, N_{counts} is the integrated spectral data counts for the Cu lines (324.75 nm and 327.39 nm), R is the responsivity[189] of the ICCD in counts per photon, T is the transmission

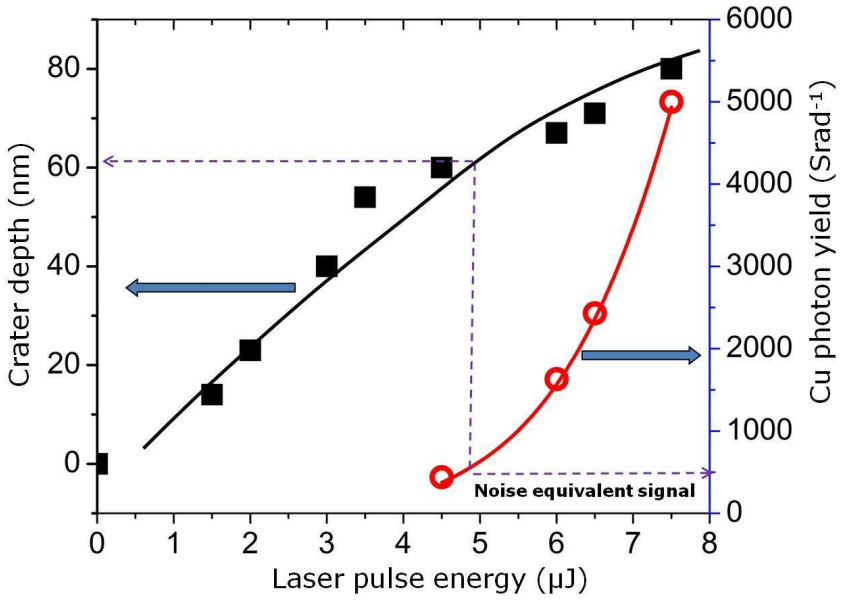

Figure 5.6: Characteristics of depth dependence in LIBS emission using sample A. Variation of crater depth and Cu photon yield per Srad versus laser pulse energy is shown.

factor of the optical elements used, QE is the Quantum efficiency of the detector and Ω is the solid angle defined by the f/4 parabolic collection mirror. Fig. 5.6 shows the depth dependence of LIBS emission where we have varied the energy from 1 μJ to 7.5 μJ using the 30 nm Cr cover layer sample and plotted the corresponding crater depth and the Cu photon yield (Srad^{-1}).

The noise equivalent signal in the Cu photon yield was calculated as ∼ 500 photons/Srad which is 3σ equivalent noise signal of the detector system. Therefore we can say that we can detect Cu atoms effectively from the buried layer when the total Cu photon count exceeds 500 photons/Srad. This corresponds to the threshold energy value of ∼5 μJ which relates to an ablation depth of 62 nm as shown in Fig. 5.6. This shows that although the ablation crater reached the Cu layer earlier (at an energy of ∼2.5 μJ for the 30 nm depth), the Cu photons only appear for a crater depth of ∼62 nm. Novotný et al.[187] have reported depth profiling analysis of Zn coated Steel samples using 100 mJ, Nd:YAG laser pulses over a relatively large focal spot area of 750 μm in diameter. The ablation rates for a 10 μm thick Zn overcoated samples at at-

mospheric pressure were 49 nm/pulse from the LIBS spectral analysis and and 40 nm/pulse from the optical profilometer analysis, respectively. Therefore 250 shots were needed to drill through the top 10 μm Zn coating to reach the buried Fe layer by monitoring the profilometer depth profie, whereas, ∼200 shots were needed by using LIBS spectra to reach the same buried layer. Therefore in their case the multiple shot depth profile essentially says that LIBS spectra from the buried layer is visible although the actual crater depth is less. This, in turn, reflects the mechanism of melting and resolidification during multiple shot laser ablation on one location. Our case of single shot femtosecond laser ablation and detection of buried layer reveals that buried layer is exposed from the profilometer analysis although LIBS spectra from the buried layer only shows up for higher laser energy pulses. As shown in Fig. 5.5, a crater depth of 55 nm for our sample A, Cu atoms at depths from 30 nm to 55 nm have been ablated along with the top 30 nm Cr layer. The excitation energies of the observed chromium lines are 3.46 eV, 3.45 eV and 3.44 eV for the 357.8 nm, 359.3 nm and 360.5 nm emission lines respectively. The copper emission lines at 324.75 nm and 327.40 nm have excitation energy levels of 3.83 eV and 3.79 eV. As the energy levels for the observed transition of these two metals are close (differing only by 11%), the relative number of Cr atoms excited in the upper upper state should be similar to the number of Cu excited atoms if the heating is isotropic throughout the full crater depth. The temperature gradient in the depth profile leads to preferential excitation of the species in the upper part of the ablation crater to form the emission plasma.

In the next experiment we worked with sample B where we have Cu coated targets on silicon wafers with different top Cu layer thicknesses (7.5 nm, 15 nm, 45 nm). Different laser pulse energies were applied on the Cu side of the sample and the single shot spectrum for each laser shot was evaluated. Si is the buried layer in this case and the appearance of Si signal (288.15 nm) determine the LIBS depth sensitivity. Fig. 5.7 shows the 300 single shot average spectra

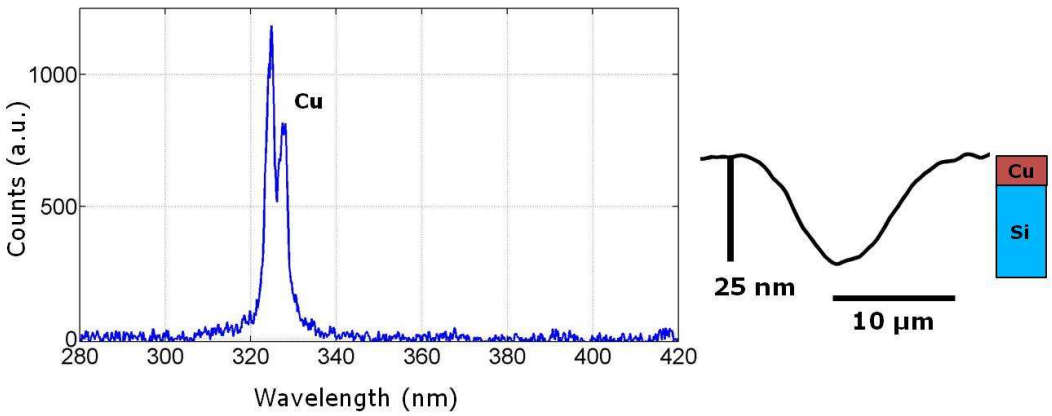

Figure 5.7: Spectra and depth profile for the sample B (7.5 nm Cu on Si) at 3 μJ energy.

and the corresponding single shot depth profile for the sample (7.5 nm Cu on Si) at 3 μJ energy. The measured crater depth was 25 nm. It confirms that although we have penetrated through the Si substrate, we do not see any Si spectra at 288.15 nm from the emitted plasma.

Spectra at different pulse energies between 10 μJ and 50 μJ (300 shots averaged, 1 μs gate width, slit width 300 μm) with target sample B have been obtained. Data for five pulse energies (15, 20, 25, 30 and 35 μJ) are shown in Fig. 5.8. We have also carried out similar measurements at the same laser pulse energies with a pure silicon wafer as a target sample keeping all the experimental parameters unchanged. The pure Si wafer can be visualized as a target sample with zero Cu thickness on top of Si.

The emission versus copper layer thickness is plotted in Fig. 5.8 showing that a thicker cover layer requires more energy to excite emission in the buried layer and the silicon emission becomes less as the layer is deeper for any given energy. The emission has been normalized to the emission for 35 μJ on pure Si wafer.

In order to give a quantitative definition of depth sensitivity, we have calculated the Cu layer depth where the Si emission falls to 1/e from its pure Si value at different energies by fitting exponential decay curves to the measured data presented in Fig. 5.8. The resultant values are plotted versus laser pulse

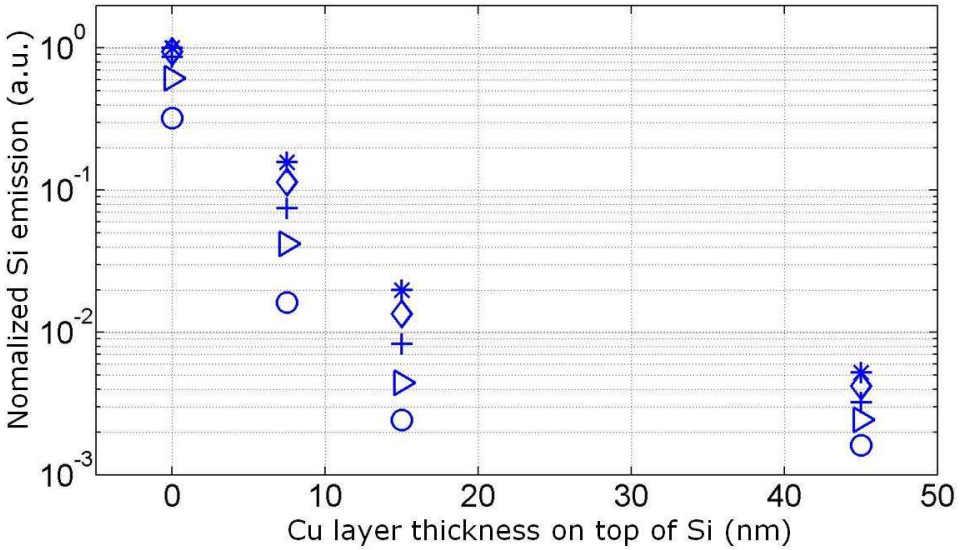

Figure 5.8: Normalized Si photon emission versus Cu layer thickness on top of the Si substrate. Laser pulse energies were '∗' 35 µJ, '◇' 30 µJ, '+' 25 µJ, '▷' 20 µJ and '○' 15 µJ. Normalized to emission for 35 µJ on pure Si

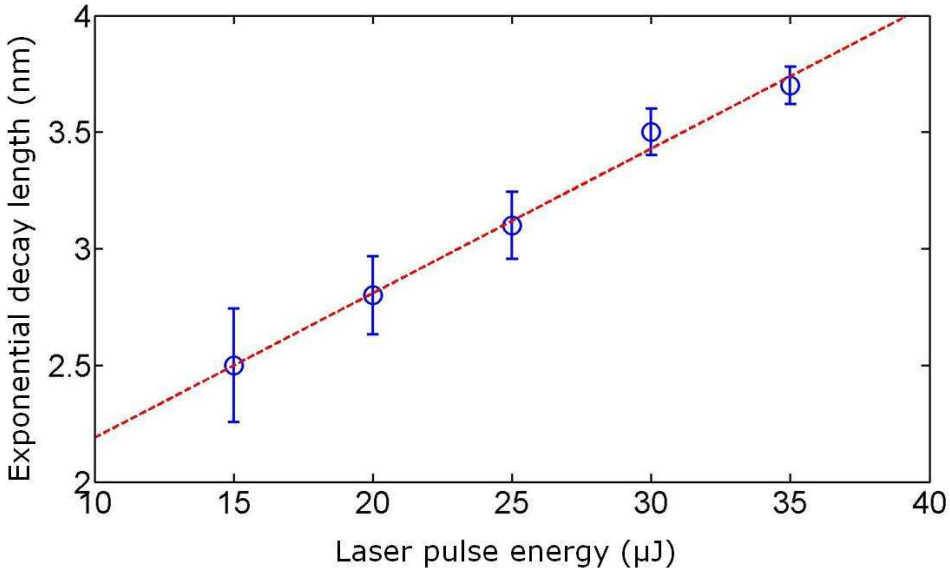

Figure 5.9: Depth sensitivity at different laser pulse energies for sample B.

energy in Fig. 5.9. The results indicate a depth sensitivity of few nanometers over a wide energy range. At 35 μJ the depth sensitivity is only 3.7 nm which means that any material at depths greater than ∼3.7 nm will not be effectively observed by using a single laser pulse of that energy. At 15 μJ the actual crater depth was ∼300 nm but our calculated depth sensitive region was only 2.5 nm. This again points toward the fact that a thin upper portion of the plasma takes part in emission during laser ablation. The laser ablation process depends on laser parameters and the characteristics of the target sample as well. Therefore, the present experimental results represent the sensitive depth region for ablation of copper and chromium target samples used in this experiment.

5.4 Plasma Ablation Model

There are several plasma ablation models which can predict plasma conditions and temperature profiles versus depth.

We have used the two temperature model(TTM) that has been described in Chap. 4.4 to predict the axial temperature profile into the depth of the target material. Our samples consisted of Cr and Cu upper layers. For simplicity we have assumed the target as a Cu metal instead of a sandwiched Cr-Cu layer and predict the depth temperature profile for the single shot laser pulse energy of 3.5 μJ. This qualitatively represents the case shown Fig. 5.5(a) where we have plotted the crater depth profile and corresponding emission spectra for an energy of 3.5 μJ. The measured focal spot diameter ($1/e^2$) for our experimental set-up was 22 μm. Therefore the corresponding peak laser fluence on the sample surface was 1.84 J/cm^2 given by $2E_{pulse}/(\pi\omega_0^2)$ where ω_0 is the $1/e^2$ Gaussian beam radius. Experimentally measured reflectivity of 800 nm laser pulses from a Cu surface at peak incident energy fluence of 1.84 J/cm^2 was found to be ∼ 88%[185]. Therefore we have taken optical absorption at 800 nm for copper metal in our case as 12%. So the absorbed laser fluence for

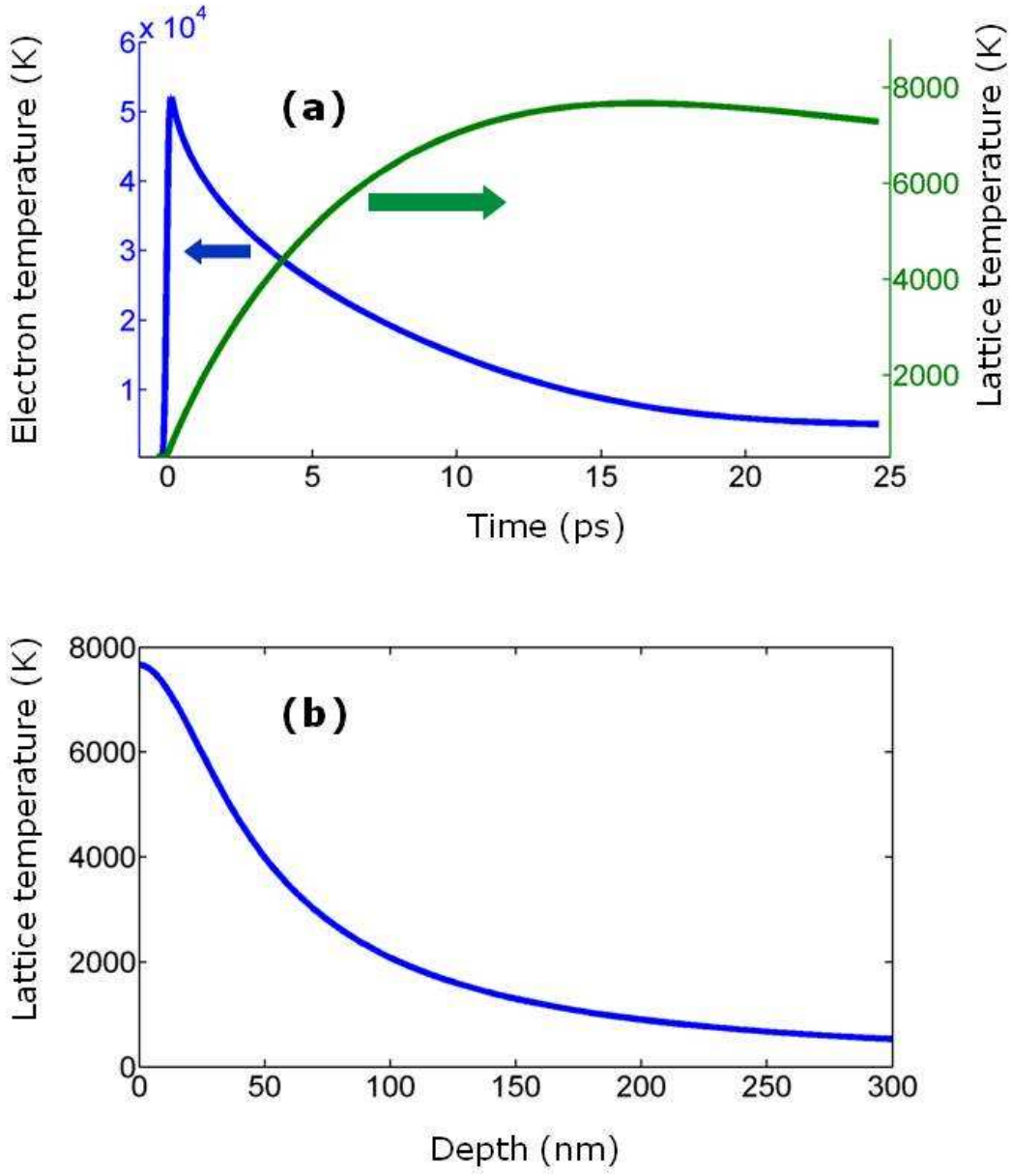

Figure 5.10: Electron and lattice temperatures versus time (a) showing the peak electron and lattice temperatures using the two temperature model with absorbed laser fluence of 0.22 J/cm^2, and the lattice temperature profile into the Cu target at the time of the peak lattice temperature (b).

TTM calculation was 0.22 J/cm^2. For these calculations values of $C_e = \gamma T_e$ where γ is the Sommerfeld parameter (γ = 98.1 J/[m^3 K^2][180]) , C_l = 3.44 $\times$ 10^6 J/[m^3 K][169], $g = 1 \times 10^{17}$ W/[m^{3}K][190, 162] have been used. The electron thermal conductivity $\kappa(T_e, T_l)$ value was calculated using the general solution provided by Eq. 4.6 where $\theta_e = k_B T_e/T_F$, $\theta_L = k_B T_l/T_F$, T_F is the Fermi temperature, and χ and η are fitting parameters, which are 377 W/[m.K] and 0.139 respectively for copper[183]. This expression is valid for a wide range of electron and ion temperatures. Fig. 5.10(a) shows the electron temperature and surface lattice temperature over a period of 25 ps from the onset of the laser pulse. The peak of the electron temperature was 52107 K. The peak of the lattice temperature of 7661 K was reached at 16.36 ps. The electron and lattice temperatures equilibrate at this time. The upper excitation energy levels for Cu emission lines 324.75 nm and 327.40 nm are 3.82 eV and 3.79 eV respectively. The maximum lattice temperature obtained from the TTM model is much less than 3.82 eV ($\sim$44302 K) which indicates very little excitation of emission would occur at this time. The lattice temperature profile into the Cu target at the time of the peak lattice temperature is shown in Fig. 5.10(b). The surface temperature of 7661 K can be taken as the maximum plasma temperature. This temperature decreases rapidly as we go deeper into the target material suggesting no plasma formation after tens of nanometers of depth. The top few nm where the temperature is very high early in time takes part in plasma formation. But the lower temperature region penetrates more deeply leading to a deeper ablation depth. The melting temperature of Cu is 1357.8 K. It can be seen from Fig. 5.10(b) that a large region of few hundreds of nm falls inside the melting depth region. The final measured crater depth of 55 nm as shown in Fig. 5.5(a) could be the result of the melting within the crater followed by the resolidification of part of the melted region. Therefore, the model indicates that the actual material ablation depth is much deeper than the highly excited region near the top surface which leads to plasma emission. From the limited emission

depth and ablation depth observed in the actual experiment it appears that the TTM model predicts target heating to a greater depth than actually occurs. This can be explained by the fact that the initially heated surface material rapidly expands and ablates carrying a significant amount of the deposited energy away from the target and undergoing expansion cooling as it expands.

5.5 Conclusions

The sensitivity of detecting buried layers with single shot femtosecond LIBS has been studied. We have shown that signal strength decreases rapidly as the target species is buried deeper below the surface for any given laser pulse energy. It is evident from our results that the plasma formed at the surface layer exhibits a strong LIBS signature while the deeper melted layer contributes very little to the single shot LIBS signal. Therefore, the emission spectra does not necessarily reflect the actual average depth profile conditions in single shot LIBS. Depth sensitivity as defined by the e-folding fall off of signals versus depth is on the order of 3 nm in the case of actual crater depths of 100's of nm. The two temperature model has been used to estimate the fall off of lattice temperature with depth. While qualitatively predicting the observed behavior, the two temperature model overpredicts the heating of the target since it does not take into account the loss of energy carried away with the ablation of the immediate surface layer. Overall it is shown that femtosecond LIBS leads to high sensitivity detection of thin surface layers aiding in detection of surface contaminants.

Chapter 6

Femtosecond Laser Plasma Plume Characteristics in the Nanojoule Ablation Regime*

In this chapter, a detailed study on laser ablation of chromium with nanojoule energy UV femtosecond pulses under background pressure conditions between 0.3 torr to 700 torr and the corresponding plasma plume behavior at different times after irradiation are described. The ablation focal spot is less than or the order of a micron when 170 nJ of laser pulse energy is used. This low pulse energy leads to short lifetimes of the plasma of the order of 10's of nanoseconds. The plume shape changes with ambient pressure due to the collision with background gas. An axially stretched plume at low pressure changes to a circular and then a radially flattened plume as the pressure increases. In addition, a separation of the ionic and atomic components is observed at lower pressure. These two components move at significantly different velocities as well. The plasma plume expands at almost constant velocity at very

* The main results of this chapter have been published in Ref. [161]. They are reproduced here with permission.

low pressure but exhibits significant deceleration at higher pressure reaching an asymptotic stopping distance. Plume images are also obtained near the ablation threshold pulse energy. The plume characteristics are compared to different models of plume expansion. The results demonstrated in this chapter were published in Ref. [161].

6.1 Introduction

Understanding laser ablation physics and the behavior of plasma plume expansion in the case of ultrashort femtosecond laser pulses is quite important in pulsed laser deposition [191, 192], laser micromachining, laser material processing [193, 194, 195, 196], nanoparticle synthesis[197] and nanoparticle deposition as well as laser induced breakdown spectroscopy (LIBS) [198, 9]. Laser ablation and the evolution of laser ablated plasmas are complex phenomena in the time and space domains. The characteristic parameters of a laser produced plasma change with laser irradiation and ambient pressure conditions. Altering the background gas pressure changes the collision rate and affects the expansion of the plasma plume. In addition to changing the size and shape of a laser produced plasma, lower background pressure enhances the emission signal intensity significantly [46]. Plume dynamics is important in pulsed laser deposition as it determines the growth and quality of a thin film deposited in background gases. In general, lower background pressure helps improve material processing as well. In a study of the ablation plume it is important to measure the different components of a plume (e.g. ionic, atomic and nanoparticle), their behavior and their dependence on different parameters. Various studies related to plasma plume expansion in background gases using nanosecond lasers have been reported [199, 200, 201, 202, 203, 204]. Kagawa et al. [199] first obtained images of plasmas when a Nitrogen laser was focused on the surface of a copper plate under different background pressure conditions. The authors

reported that the diameter of the plasma plume as well as characteristic emission spectra varied with gas pressures. They also identified two distinct plasma regions at low pressure (1 Torr). Femtosecond laser pulses interact with plasmas on a very short time scale and limited spatial scale. The investigation of plasma plumes generated by femtosecond laser pulses has been a topic of significant interest in the last several years. Experiments on the dynamics of the plasma plume created with femtosecond laser pulses have been reported by a number of authors in recent years [205, 206, 207, 208, 209, 210]. Amoruso et al. have carried out investigations on propagation dynamics of the different components of femtosecond plasma plume such as the atomic and nanoparticle plumes [206, 207] and angular distributions of plume components [211]. Canulescu et al. [208] have compared nanosecond and femtosecond ablation plume dynamics. Most of the reported experiments were carried out using laser pulse energies of 10's of microjoules or more. Plasmas generated with much lower incident laser pulse energies will have shorter lifetimes and small propagation lengths. If a very small focal spot size is employed, for example by using a high numerical aperture objective to focus the laser pulses, then the spatial structure of the plasma plume will also be much smaller. Working in the UV wavelength range enables sub micron focal spots and at the same time leads to enhanced absorption of laser pulse energy on most target materials. Such conditions would be optimal for carrying out high precision material processing with ultrafast lasers. Therefore it is important to understand the behavior of plasma plumes generated by low energy, tightly focused UV laser pulses. In the current investigation we study the characteristics of the plasma plume generated by 266 nm femtosecond laser pulses with 26 to 170 nJ energy. A microplasma is produced by such ultrashort femtosecond laser pulses by focusing to submicron focal spots. The evolution and the dynamics of the plasma plume expansion at different background pressures are reported in the following sections.

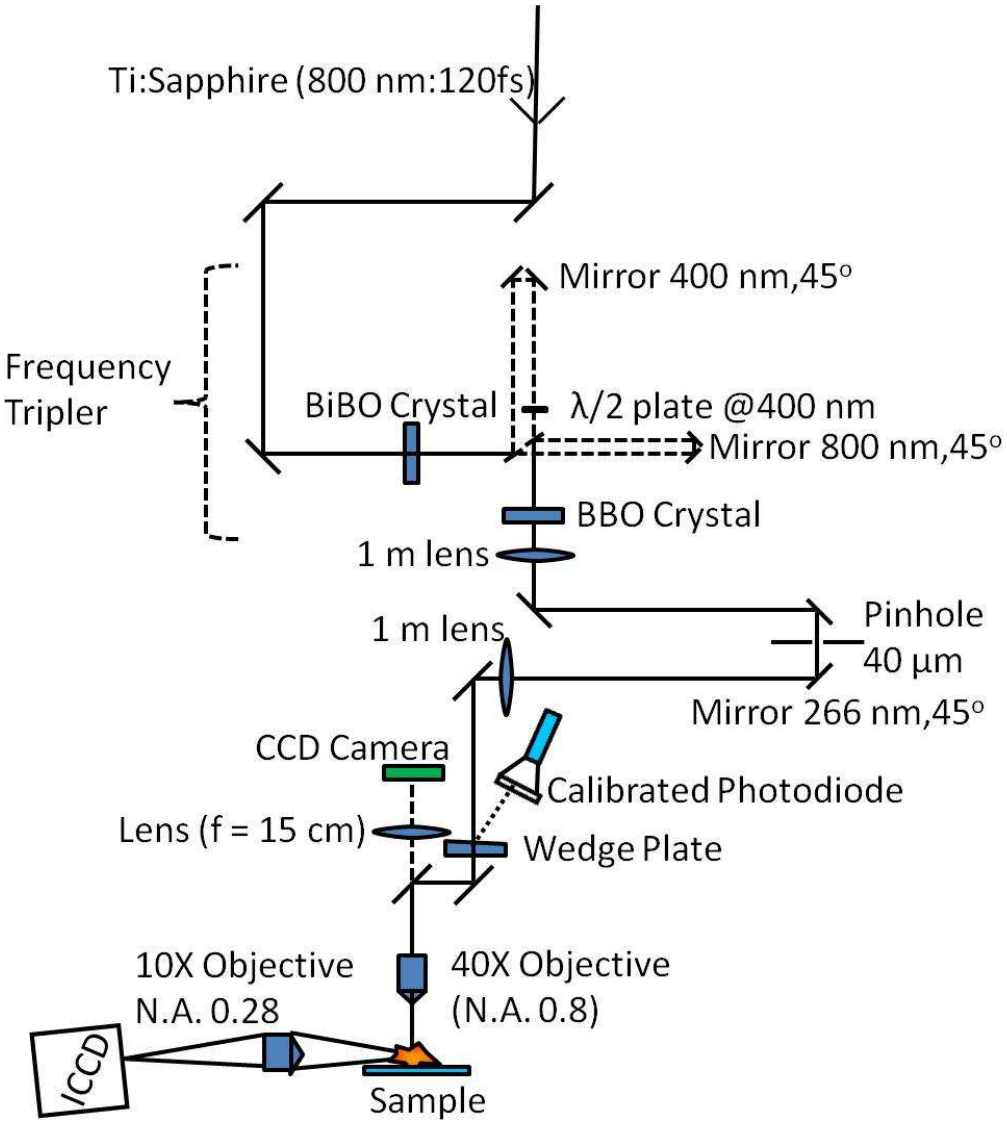

Figure 6.1: Schematic of the experimental set up.

6.2 Experimental Procedure

The experimental setup used for this experiment is shown in Fig. 6.1. The experimental set is similar to what has been used in Chap. 4. In this experiment, the laser beam was focused onto the target sample using a quartz 40X microscope objective (Partec objective, Numerical Aperture 0.8, working distance 0.8 mm) to achieve submicron focal spots. The energy delivered to the sample was measured using a photodiode cross calibrated against a Spectra Physics model 407A power meter and monitored throughout the experiment. A CCD camera (Point Grey Chameleon USB camera) in conjunction with an f = 15 cm achromatic lens viewing through the same 40X objective and through a turning mirror was used as a sample viewing system to make sure that the sample surface was at the focus of the input beam. In order to obtain a side view of the plasma plume, the emitted plasma light was imaged onto an ICCD (Andor iStar ICCD) camera using a 10X microscope objective (Mitutoyo, NA 0.28). The microchannel plate gain of the ICCD camera was set to 200 (out of 255) for all the experiments. The targets were mounted in a commercial 3-D computer controlled precision micro-positioning translation stage (Melles Griot Nanomover). The experiments were performed inside a vacuum chamber with the capability to change the pressure in the system. The gate delay time was set to an accuracy of 0.5 nanosecond relative to the laser pulse. Different gate delays were used to capture plume characteristics at different times. A thin uniform layer of chromium (500 nm) deposited using planar magnetron sputtering on top of a premium silicon wafer was used as the target sample for this experiment, as shown in Fig. 6.2(a).

6.3 Results

A tight focusing objective with very high numerical aperture (N.A.= 0.8) was used to create a micro-ablation region on the target sample. Fig. 6.2(b) shows

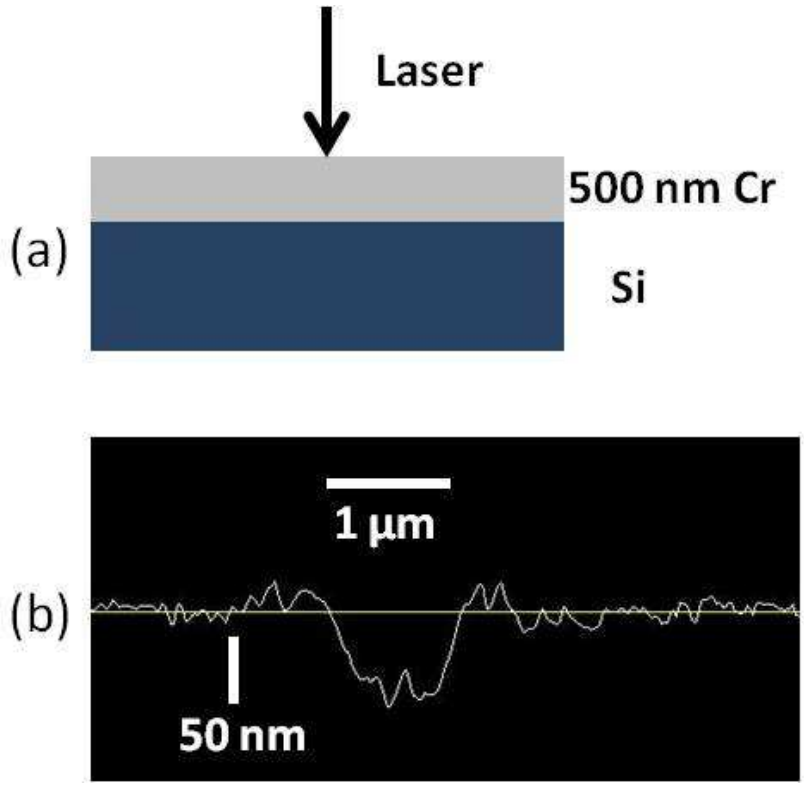

Figure 6.2: (a) Schematic of target sample and (b) AFM lineout scan of the single ablation spot at 170 nJ.

the experimentally observed depth profile of the ablation spot using atomic force microscopy (AFM). This shows that the diameter of the crater was $\sim$ 1 μm and corresponding depth as $\sim$ 65 nm. This single shot ablation crater was created using a 170 nJ laser pulse energy. We employed this energy to explore plasma plume structures and their evolution at different background pressures. This particular energy value was chosen to ensure that we had sufficient emission radiation from the plasma plume to characterize the plasma and at the same time the ablation spot is in the range of a micron or less. We also have carried out measurements with different energy values lower than 170 nJ which will be discussed later in the paper. In order to take snapshots at different times, we have varied the gate delay by steps of 5 ns and accumulate the emission from the plasma over an integration time of 5 ns for each exposure. The reported delay times refer to the time from the laser pulse to the end of this gate window. The emission from a single shot ablation plasma was not sufficient to produce a good resolution image. Therefore we have accumulated 50 single laser shots to produce an image of the plasma plume. Every laser shot was taken on a fresh target surface and the gate time, gate width and all other experimental parameters were the same during this accumulation.

6.3.1 Plume Images

Plasma plume images were taken at various background pressures of air and at different time delays with respect to the laser pulse. The background pressure values used for the experiment were 0.3 torr, 2.3 torr, 5.5 torr, 18.5 torr, 29 torr, 52 torr, 107 torr and at ambient air pressure of 700 torr. Fig. 6.3 shows ICCD images of plume expansion at (a) 2.3 torr, (b) 29 torr and (c) at ambient air pressure with a laser pulse energy of 170 nJ. Each of these images was normalized to its own maximum intensity. For the first image, T = 1 ns, we have accumulated 4 ns of time before laser strikes the material surface and 1 ns after that. All of the images employed a 5 ns of gate width.

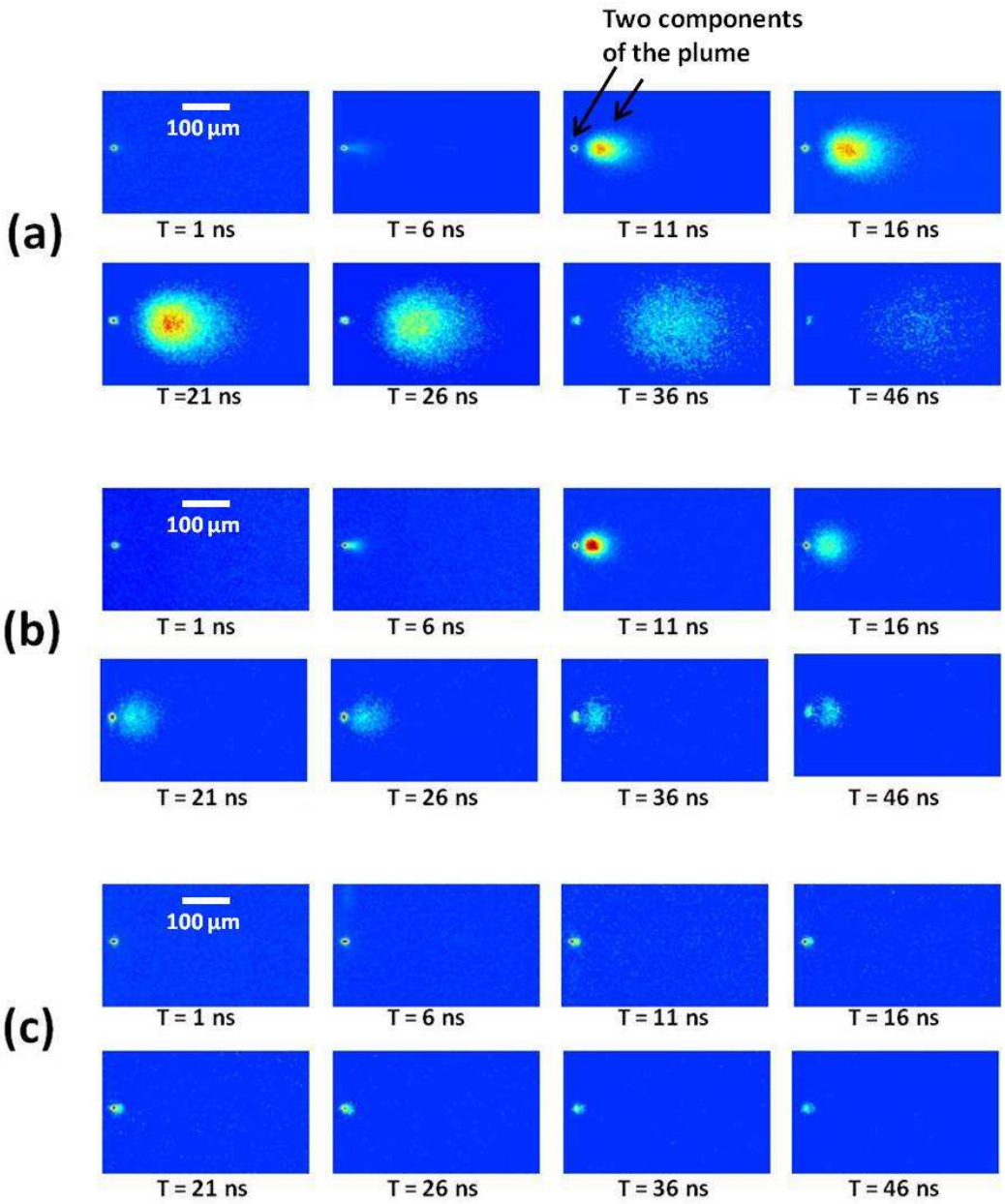

Figure 6.3: Temporal evolution of plasma plume at various background pressure:(a) 2.3 torr, (b) 29 torr and (c) at ambient air pressure. The time T denotes the delay after the laser pulse for the end of the 5 ns integration period.

The shape and size of the plume changes significantly as we move from a low background pressure to a high background pressure environment. A forward directed expanding plasma plume with an elongated shape travels quickly out of the target surface at 2.3 torr. The plasma plume front position reaches $\sim$ 340 μm at 46 ns and then the plume disperses into the background medium. The plume front positions were measured at the location where the intensity falls to 10% of the peak intensity value of any particular plume. At a higher background density of 29 torr the expansion is slowed more quickly by collisions with the background gas species and the plasma plume becomes more spherical in shape. The plume front position does not expand past 85 μm. At ambient air pressure we see a very tiny plume with little expansion. Fig. 6.4 shows images of plasma plume taken in the period of 6 to 11 ns from the onset of laser pulse for various pressures.

All images are normalized to their own maximum intensity. This clearly shows how plasma is confined closer to the target surface at high pressure and the plume shape changes from circular to an elongated one at lower pressures. The boundary between the plume front and the surrounding air can be termed as a contact front. A relatively sharp contact front is visible from 5.5 torr to 107 torr but it blurs and disappears as pressure decreases. The angular distribution of the plasma plume in femtosecond laser ablation process can be described using the relation $S_\theta = S_0 \cos^n(\theta)$ where S_0 defines the particle fluence at the center of the plume and n is a fitting parameter that defines plume anisotropy. We have obtained n = 5.0±0.4 for the case of 107 torr and n = 7.5±0.5 at 5.5 torr using the data shown in Fig. 6.4. This quantitatively describes the change in the plume shape as observed at T = 11 ns when the expansion is already predominantly collisional.

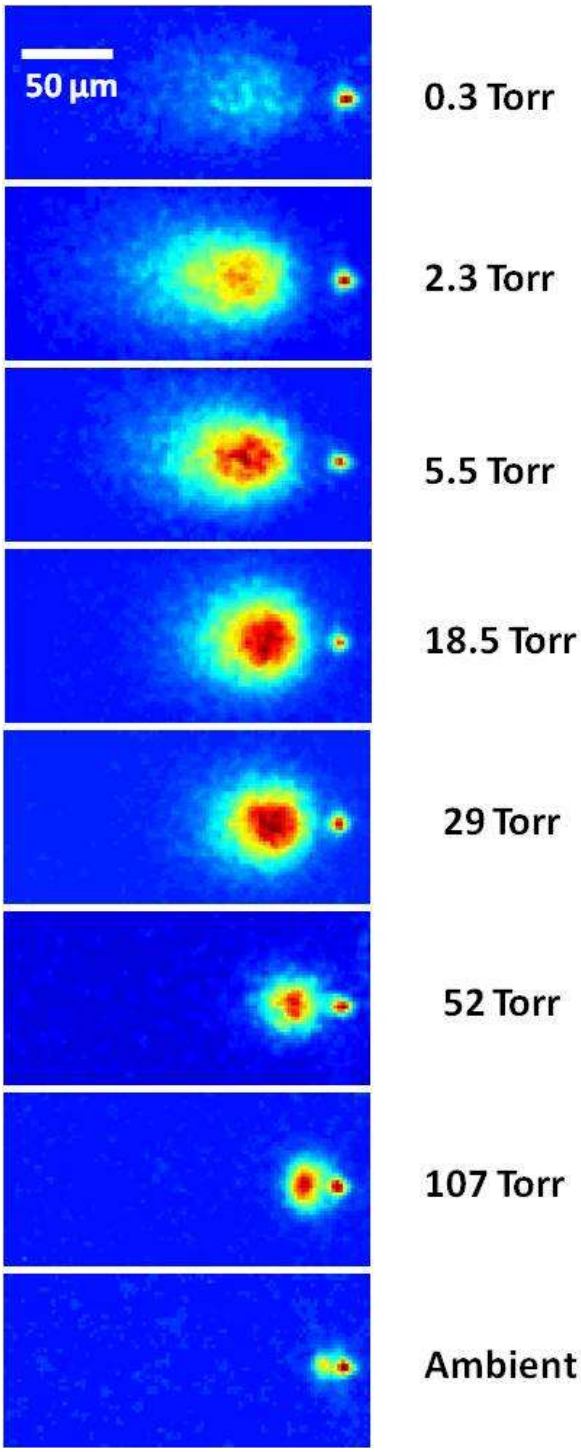

Figure 6.4: Images of plasma plume for an accumulation end time of 11 ns from the onset of the laser pulse for various pressures. The laser enters from the left.

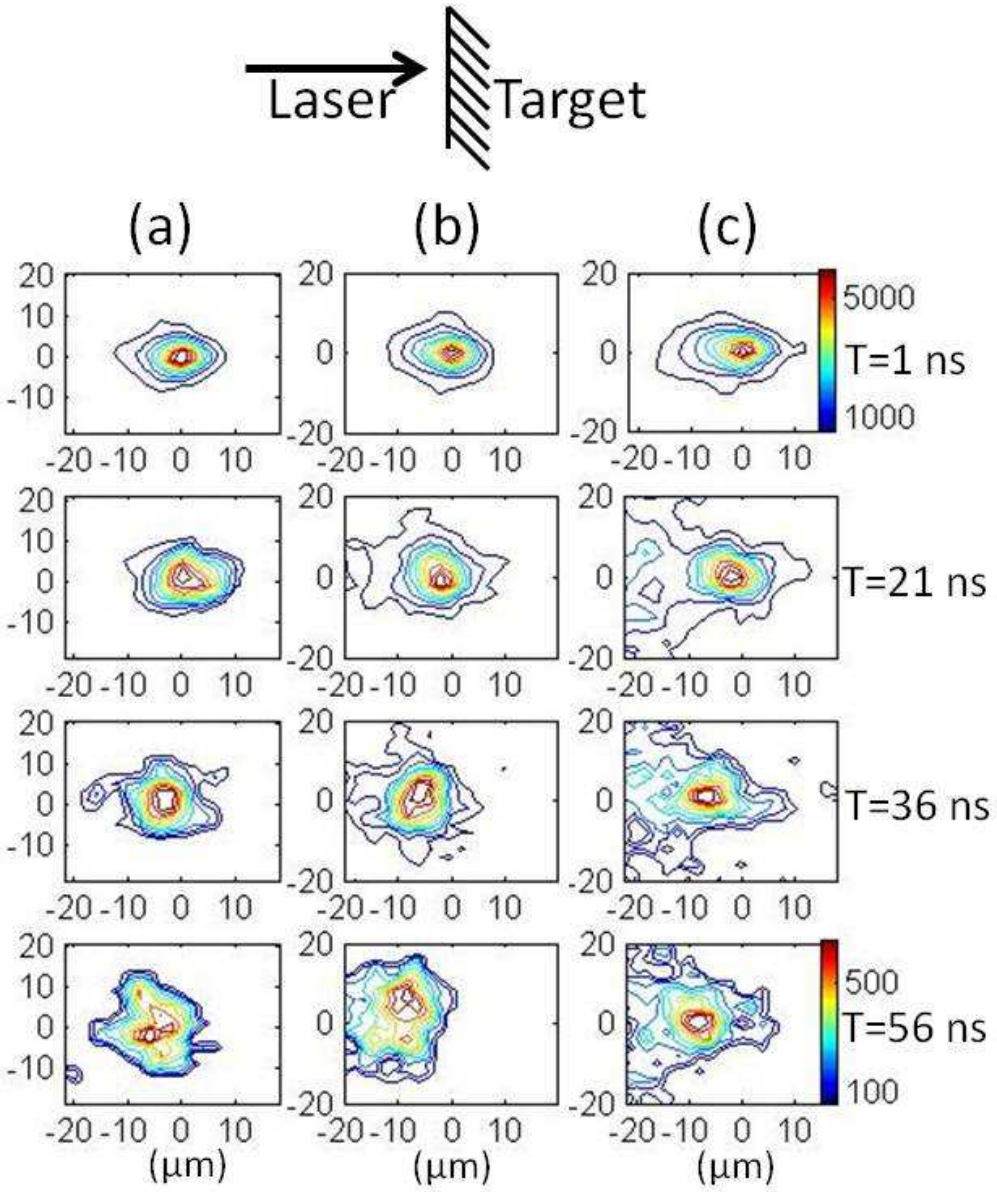

Figure 6.5: Contour plot of the slow component plume at background pressures of (a) 0.3 torr, (b) 18.5 torr and (c) 52 torr. Time T denotes delay after the laser pulse.

6.3.2 Plume Dynamics

Fig. 6.3(a) shows that a component of the plasma plume is visibly separated from the original plume cloud at T = 11 ns which we refer to as plume splitting. Two arrows in Fig. 6.3(a) at T = 11 ns show the two components of the expanding plume. If we analyze Fig. 6.3, splitting of the plasma plume is clearly visible at low pressure (2.3 torr), barely visible at moderate pressure (29 torr) and just barely visible at ambient pressure as can also be seen in Fig. 6.4. This splitting of the plasma plume in two components at low background pressure has been a topic of research using nanosecond [202, 212] and femtosecond [206, 208] laser pulses by a number of authors. Those experiments showed that the first component is the quickly expanding ionic and atomic plume containing ions and atoms and the second component is primarily filled with slow-moving atomic vapor and nanoparticles of the target sample material. Amoruso et al. [213] have shown that the early time expansion ($\tau < 1\mu$s) of a Ni plume at a laser fluence of 0.9 J/cm^2 shows ionic and atomic plume characteristics whereas nanoparticle plume expands at a later time ($\tau > 1\mu$s). They also have shown [206] that the two components of the plume move with a velocity of $\sim 10^4$ and $\sim 10^2$ m/s respectively at low pressure. In our case the plasma lifetime is very small because of low incident energy of our laser pulse. The whole emission process decays away within 60 ns from the time laser strikes the material. Therefore we could not observe temporally different regimes for the evolution of two detached plumes. The slow part of the plume that appears just above the target sample as soon as laser ablation occurs will be called the surface plume in our subsequent discussion. Fig. 6.5 shows the contour plot of this part of the plume at (a) 0.3 torr, (b) 18.5 torr and (c) 52 torr at different times. It can be seen from the figure that the movement of the center of the surface plume is small in the first 21 ns but it reaches 6 μm (0.3 torr) and 8.5 μm (18.5 torr, 52 torr) at 56 ns. The velocity can be calculated as (1.1±0.2) × 10^2 m/s and (1.5±0.3) × 10^2 m/s for pressures of 0.3 torr and 52 torr respectively

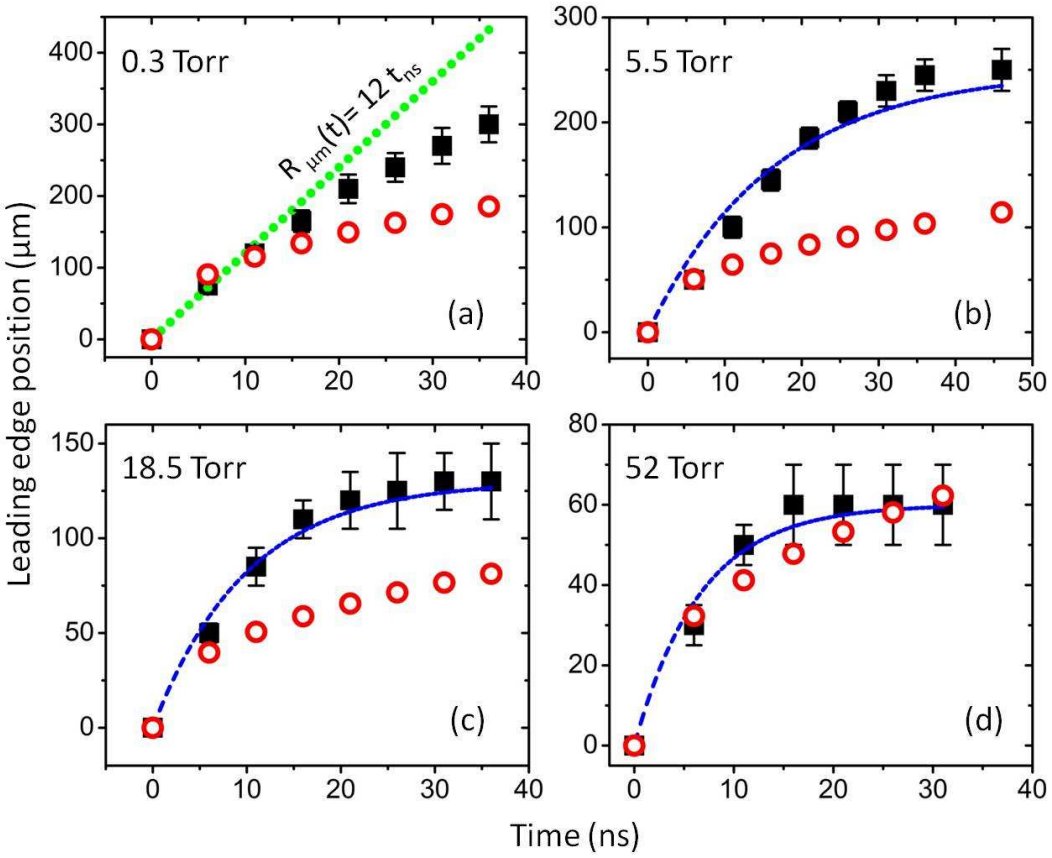

Figure 6.6: Position of the leading front of the chromium plasma plume produced in background gas pressure of (a) 0.3 torr, (b) 5.5 torr, (c) 18.5 torr and (d) 52 torr obtained from the gated ICCD images at different times. Experimental data points (■), linear fit (•), blastwave calculation (○) and drag model fit (–) are shown with different fitting parameters. For the drag model $\beta = 0.06 \pm 0.01$ ns^{-1} at 5.5 torr, $\beta = 0.1 \pm 0.04$ ns^{-1} at 18.5 torr and $\beta = 0.15 \pm 0.06$ ns^{-1} at 52 torr

which matches well with the reported slow component expansion velocity from previous studies. However, at 56 ns the plume may still primarily be in atomic vapor form since it will take some time for the vapor to cool and condense into nanoparticles.

The faster part of the plasma plume region expands and propagates into the background gas very rapidly. Plume propagation can be studied quantitatively by analyzing the position of the plume front as a function of time. The images of the plume clouds were converted into intensity contour plots. The leading

surface of the contour where the intensity has a value of 10% its maximum value was taken as the plume front position. This front basically separates the plume cloud from the surrounding medium. The plots of the position of the leading edge of the plume versus time for different ambient background pressures are shown in Fig. 6.6. Fig. 6.6(a) shows at very low pressure (0.3 torr) the plume expands almost freely in the background gas with an average velocity of 0.83×10^4 m/s. The plume expansion appears to be linear in the early stage of its evolution but the time span of linearity decreases with increasing background gas pressure due to the increasing collisional stopping power at higher pressures, leading to a ballistic expansion time period scaling approximately as the inverse of pressure. At 0.3 torr we can use $\mathrm{R}_{\mu m} = 12\ \mathrm{t}_{ns}$ to fit the initial expansion as shown. Propagation is linear until approximately 15 ns and the velocity of the plume decreases thereafter.

Plume expansion and propagation in a collisional background gas can be described with two models. One is the blastwave model and the other one is the drag model. The Sedov-Taylor point source explosion theory [214, 215] predicts the expansion of a blast wave in background gas and can be used to determine the dependence of the propagation of plasma plume on the background gas pressure. In this model the expansion of the plasma plume generates a strong pressure impulse in the background gas generating a strong shockwave that precedes the plasma. The Sedov-Taylor equation [215] states that the blast wave front position R originating from an instantaneous pulsed release of energy is given in the case of spherical symmetry by

$$R = \lambda_0 \left(\frac{E}{\rho}\right)^{1/5} t^{2/5} \tag{6.1}$$

where λ_0 is a dimensionless constant dependent on the specific heat of the gas with a value close to 1, E is the energy released during the explosion which

can be taken as the absorbed laser pulse energy (taken as half the incident laser energy), ρ is the density of background gas and t is the propagation time for the blast wave. We have used this equation to calculate the plume front position at different background gas pressures as shown in Fig. 6.6 (a), (b), (c) and (d) for 0.3 torr, 5.5 torr, 18.5 torr and 52 torr respectively. It is seen that the blastwave model does fit for the highest density case shown at 52 torr background pressure but becomes progressively worse at lower pressures. This is due to two factors. The first is that the initial expansion of the energetic ions is ballistic until collisions slow down the initial plasma particles and allow them to couple to a pressure wave in the background gas. Secondly, the ideal blast wave solution only assumes instantaneous release of energy in the background gas and does not take into account the mass of the ablated particles and the extra momentum that they couple into the expanding gas. Both these factors lead to an increase in the real expansion velocity of the plasma plume. However, as the background pressure increases the initial ballistic expansion is stopped more quickly and the relative mass injected becomes smaller and smaller relative to the mass of the background gas. Thus the blast wave model becomes more accurate at the higher pressures of around 50 torr.

In the second model [216, 217] the plasma plume expands rapidly in the beginning but slows down thereafter until it reaches a limiting expansion distance which is also known as the stopping distance. The drag force created by the background gas molecules results in deceleration of the plasma plume. The motion of the plasma front towards the stopping distance can be expressed in the form of the drag model [216, 217]

$$R(t) = R_0 \left(1 - e^{-\beta t}\right) \tag{6.2}$$

where $R(t)$ is the distance of the plume edge at time t and R_0 is the stopping

distance. The damping coefficient β indicates the amount of resistance imposed by the background gas to the plasma expansion. Fig. 6.6 shows the R-t plots for the drag model which has been fit to the plume expansion for 5.5 torr (b), 18.5 torr (c) and 52 torr (d). The stopping distances for different pressures were taken from the experimental plume propagation images. The R_0 values were 250±20 μm at 5.5 torr, 130±20 μm at 18.5torr and 60±10 μm at 52 torr. The corresponding β values are 0.06±0.01 ns^{-1} at 5.5 torr, 0.1±0.04 ns^{-1} at 18.5 torr and 0.15±0.06 ns^{-1} at 52 torr. The drag model does not apply at very low pressure and thus we have not tried to fit it for the 0.3 torr case where the plasma moves with a slowly decreasing velocity over the period of observation. By choosing the appropriate coefficients, the drag model fits fairly well for the three higher background pressure cases throughout the plasma plume expansion.

6.3.3 Plume Length

Plume length can also be estimated at different background pressures using an adiabatic expansion model [202, 218] which prescribes a plume length given by the point where the adiabatically expanding plasma plume pressure equals the background gas pressure. The plasma length is then given by

$$L = A\left[(\gamma - 1)E\right]^{1/3\gamma} P_0^{-1/3\gamma} V_i^{(\gamma-1)/3\gamma} \tag{6.3}$$

where γ is the specific heat ratio of the ablation plume species, E is the absorbed laser energy, P_0 is the ambient gas pressure, V_i is the initial heated volume of the plasma and A is a geometric factor. Normally for ns duration pulses V_i is taken as $V_i = \upsilon_0 \tau_{laser}(\pi r^2)$, where υ_0 is the initial expansion velocity, τ_{laser} is the laser pulse width and r is the radius of the spot size respectively.

In the present case we take the initial volume as the conical volume formed by the distance of initial ballistic expansion of the energetic plasma at the

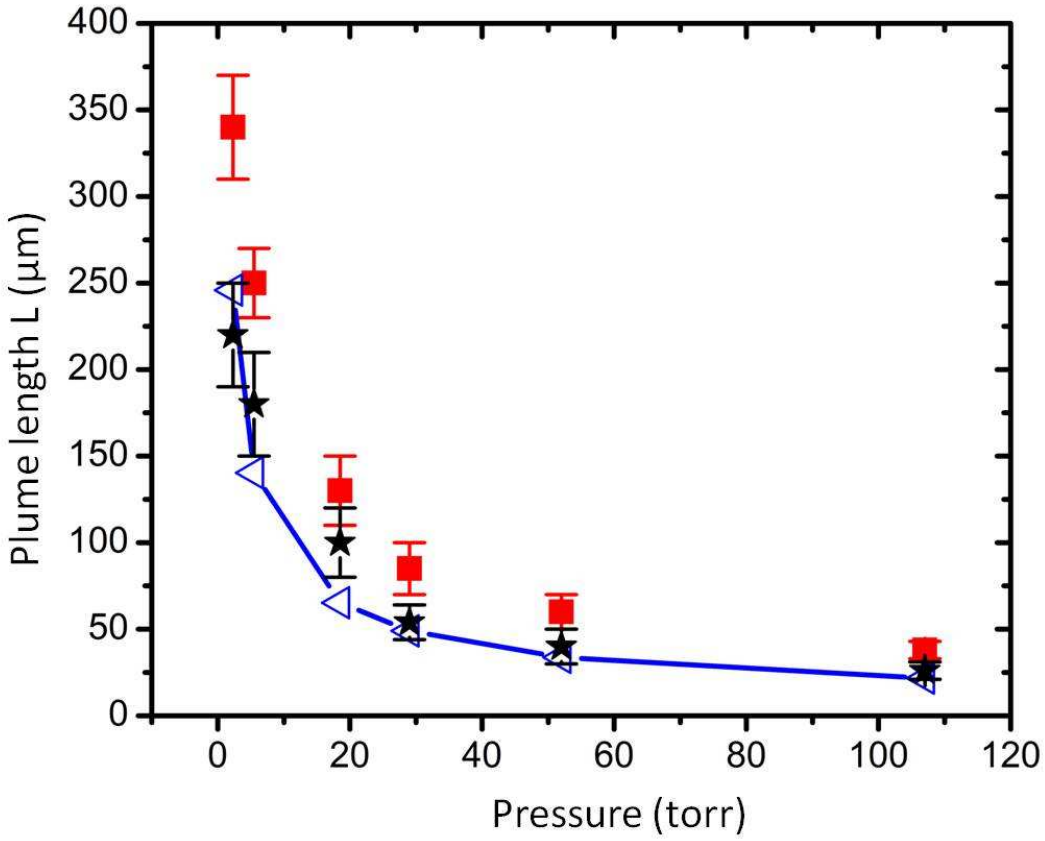

Figure 6.7: Plume length L of the chromium plasma at different ambient pressure. Experimental plume length (■), plume emission length (★) and calculated values (-◁)

measured velocity of 1.2×10^4 m/s with a cone angle of expansion given by the average cone angle of the plasma plume measured for each different background pressure. The duration of the ballistic expansion period is calculated from the case of 0.3 torr background pressure where it was found that the expansion was purely ballistic up to a time of $\sim$ 15 ns. Assuming that the collision time scales inversely with background pressure this expansion time is given for different pressures by $15(\frac{0.3}{P_{torr}})$ ns. To calculate plume expansion angle θ, we have measured the plume images at different times and taken a best fit of the cone half angle (half width at 10% peak intensity) averaged over all images for a particular gas pressure. We obtained values of θ of 27^o, 31^o, 36^o, 39^o, 43^o and 45^o for 2.3 torr, 5.5 torr, 18.5 torr, 29 torr, 52 torr and 107 torr respectively. For a conical plume with a spherical leading surface the geometric factor A can be calculated as [218]

$$A = \left(1 + \frac{1}{tan\theta}\right)\left(\frac{3tan\theta}{\pi + 2\pi tan\theta}\right)^{1/3} \tag{6.4}$$

where θ is the measured cone half angle. The initial energy, E, can be estimated from absorbed laser energy. The starting optical absorption at 266 nm for chromium metal is 41% [219]. However as the chromium metal is ionized by the femtosecond laser pulse the warm dense matter state created will have a different absorption coefficient. Previous reports of absorption show that for femtosecond UV laser pulses, once a plasma is formed, the absorption tends to converge to a value of approximately 50% for different starting materials [184]. Thus, for simplicity we have assumed an absorption coefficient of 50% giving an absorbed energy of 85 nJ per pulse in our experiment for an incident energy of 170 nJ. The specific heat ratio γ was taken as 5/3 for chromium and values of the initial heated volumes V_i were calculated as 3.54×10^{-15} m^3, 3.58×10^{-16} m^3, 1.37×10^{-17} m^3, 4.44×10^{-18} m^3, 1.02×10^{-18} m^3 and 1.35×10^{-19} m^3 for 2.3 torr, 5.5 torr, 18.5 torr, 29 torr, 52 torr and 107

torr respectively. Fig. 6.7 shows the experimental and calculated values of the plume length for different background pressure. Experimental values of plume length are obtained from the ICCD images of the plume. Contour plots of the plume images were analyzed at the time before the plume disperses into the background and the distance measured from the target to the outermost points of the contours where the intensity falls to 10% of its peak intensity value were taken as the plume length [218, 220]. The plume length is essentially same as the plume front position at stagnation point. These values are plotted in Fig. 6.7. In addition, the length of the plasma emission region defined by distance between the 10% intensity points in the axial direction is also plotted. This is termed as plume emission length. It is seen that at lower pressures the total plume length is bigger than predicted from the adiabatic expansion model while the plume emission length is close to the model predictions. This indicates that at lower pressures the plasma is ejected ballistically into the background gas and then starts an adiabatic type expansion after a significant propagation distance when it becomes collisional. This appears to effectively displace the starting point of the adiabatic expansion away from the target surface.

6.3.4 Plume Images Near Threshold

In order to obtain plume images near the threshold ablation regime, we reduced the laser pulse energy until the images disappeared. We have acquired plasma plume evolution images on the ICCD for different delay times, T. The background pressure was kept at 19 torr to make the final plume almost circular with a relatively sharp contact front. The minimum energy was 26 nJ for which the laser plasma plume was still visible at this pressure. Laser pulse energies of 26 nJ, 33 nJ, 44 nJ, 71 nJ and 111 nJ were chosen for the experiment to show how the plasma plume formation and propagation changes with pulse energy. The experimental condition and procedures to obtain images are the same as described earlier. Fig. 6.8 shows the plume images for laser pulse energies of

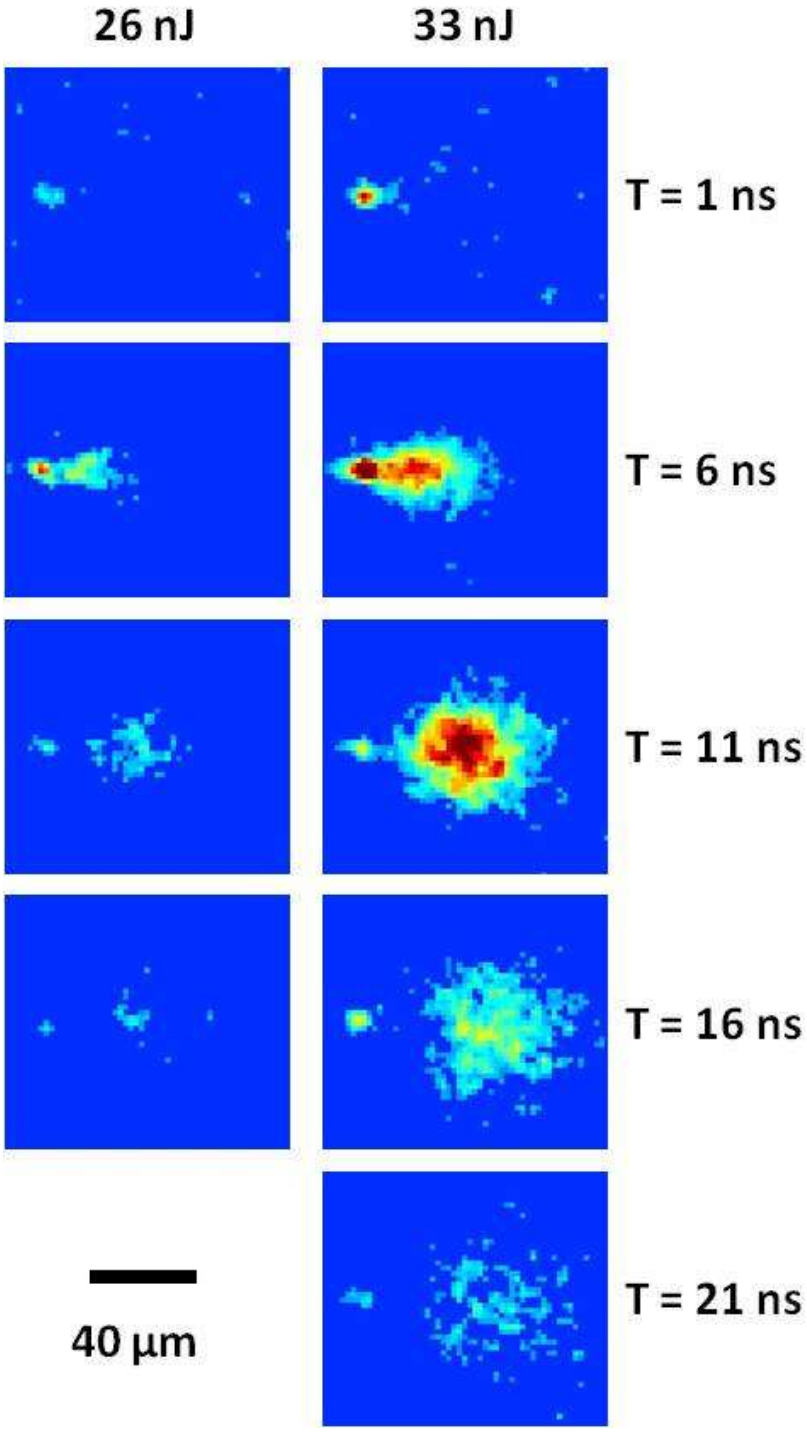

Figure 6.8: Temporal plasma plume expansion at 19 torr background pressure with laser pulse energies of 26 nJ (left) and 33 nJ (right). Time, T, denotes delay after the laser pulse. The laser is incident from the right.

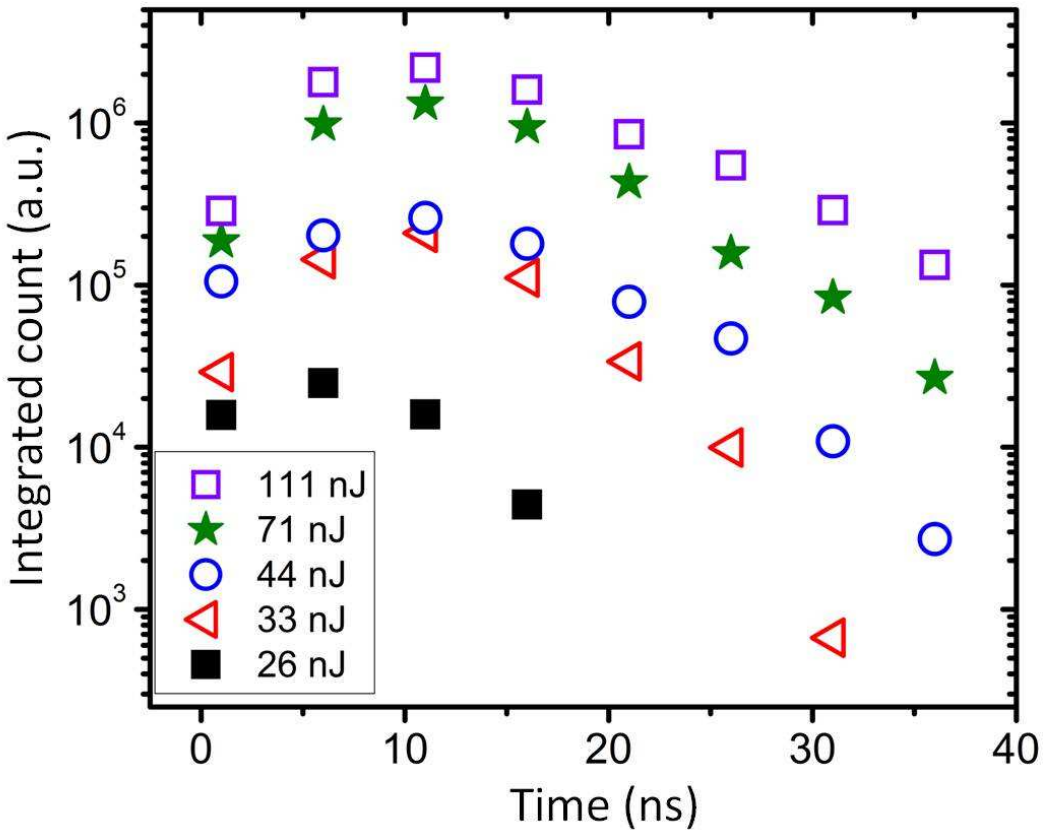

Figure 6.9: Integrated intensity counts for the plume images for different laser pulse energies.

26 nJ and 33 nJ. Each of these images is normalized to its own maximum intensity. An estimated half micron diameter focal spot with 26 nJ of laser pulse energy corresponds to an approximate energy fluence of 13 J/cm^2 which can be taken as the approximate plasma emission threshold value for our experimental parameters. For an incident energy of 26 nJ the plasma plume moves to $\sim$ 50 μm after 11 ns and disperses outwards after that. At 33 nJ, the plume forms a more circular shape and propagates until 16 ns. The distance covered is 80 μm in 16 ns which corresponds to a velocity of the plume of 0.5 $\times$ 10^4 m/s. This is lower than that observed for 170 nJ pulses by approximately a factor of 2 times which is to be expected since the five times lower incident intensity would lead to a colder plasma temperature and lower ion velocity.

Next, we investigated the scaling of integrated emission brightness of the ablation plume as a function of delay time. In order to do this we have integrated the counts for all the pixels of the plume images minus the background dark image counts. The gain of the ICCD was set at 200 which corresponds to approximately 90 counts for one generated photoelectron. Therefore, we have integrated pixels only which are more than 90 counts to make sure that at least one photoelectron was present. Fig. 6.9 shows the plot of integrated intensity versus time for different laser pulse energy. The integrated intensity increases with increasing pulse energy as expected. For 26 nJ, the integrated counts reach a maximum at 6 ns and then decrease rapidly. As the pulse energy increases, the maximum integrated brightness was observed at approximately 11 ns. The lifetime of a plasma plume can be approximated as the time when the integrated counts of the plasma plume image drops to (1/e) of its peak value. Using this we can estimate the single pulse plasma lifetime for 26, 33, 44, 71 and 111 nJ energies as 11.5, 18, 19.5, 20 and 22 ns respectively for the pressure of 19 torr.

6.4 Discussion

In the present study we investigate a new regime of plasma plume expansion for very low incident energies in the nanojoule regime. This regime leads to much smaller plasma volumes with shorter plasma lifetimes than in previous studies. However it is observed that the plasma plume follows the same general behavior as it does for the case of higher incident energies. As shown in the previous section this behavior can be broken into four regimes: (1) ballistic expansion, (2) collisional expansion, (3) stagnation and (4) slow expansion of a surface plume arising from the heated solid target material. The ballistic expansion period is on the order of nanoseconds to subnanosecond in duration, decreasing with increasing pressure as the collision frequency increases with pressure. The collisional regime can be described by two models, either a simple blast wave model or a collisional drag model. The former is applicable if the expansion is dominated by collisions and is not perturbed by excessive mass injection or a long preceding period of ballistic expansion. These criteria are best satisfied in our case for background pressures of around 50 torr where the calculated blast wave expansion agreed well with our measured expansion. The collisional drag model is more general and fits all the expansion cases except the lowest background pressure cases where the ballistic expansion dominates. However, it requires appropriate choices of the damping coefficient and stagnation distance for each background pressure. Finally the stagnation distances can be estimated from the expansion distance at which pressure balance is obtained between the adiabatically expanding plasma plume and the background gas. As shown in Fig. 6.7 good agreement between the measured values and the model is obtained assuming conical expansion and an initial volume given by the ballistic expansion distance. It is then useful to compare these results to previously published results obtained at higher laser pulse energies.

Plume splitting into two distinct components with different velocities has

been observed by various authors for nanosecond and femtosecond laser pulses with higher incident energy (few μJ or more). We do see similar splitting of plasma plumes into two components with different velocities but the low incident energy and small size of the initial plume restricts the observation of the slow moving component to short time durations over which only a modest amount of expansion is observed. Amoruso et. al. [213] has shown that the composition of the two parts of the femtosecond laser plasma plume can be determined by the spectral emission of the relevant components. The fast component shows emission due to the atomic species of the target material whereas, self emission of the slow component shows a structureless, broadband, continuum spectrum which is characteristic of hot nanoparticles produced during the event. It is important to note that the spectra and the evolution of nanoparticles were determined at $\tau > 1$ μs, a much longer timescale than our observed period. Thus, our slow expansion plume corresponds to the expansion of hot dense target species which probably will evolve into the nanoparticle plume observed in these previous studies. Previously reported plasma plume shapes are spherical-like for nanosecond laser produced plasmas, whereas, femtosecond pulses show a preferential forward directed expansion of the plasma along the target normal in a low pressure environment [208, 210]. This can be explained by the generation of high plasma pressure on the surface at the initial time due to the strong over heating [210]. A strong forward directed velocity component is generated with little resistance from the background neutrals at low pressure. At very low pressure (1.5×10^{-4} torr) even nanosecond plasmas exhibit such a directed expansion behavior [203]. We observe similar shape changes in plasma plume with different background pressures.

Al-Shboul et. al. [210] have used 40 fs, 800 nm laser pulses with ~ 6.9 mJ energy to create a plasma plume that expanded to a stopping distance of ~ 4.8 mm in 5 torr background N_2 pressure. In our case the plasma plume has moved a maximum of ~ 250 μm at 5.5 torr background gas pressure where the pulse

energy was $\sim$ 170 nJ. The propagation distance is $\sim$ 19 times smaller whereas the pulse energy is 4×10^4 times smaller in our case compared to theirs. To compare to our result we can assume a similar supersonic expansion velocity of 1.2×10^4 m/s during the first 0.9 ns (using the previous estimate given by the expression $15(\frac{0.3}{P_{torr}})$) of the plasma plume expansion and use the focal spot diameter as 100 μm as reported by them [210] to calculate the initial heated volume in their case. This leads to an initial cylindrical plasma plume volume of 3.39×10^{-13} m^3 which is $\sim$ 950 times greater than in our experiment. From Eq. 6.3, for γ =5/3, we can say $L \propto E^{1/5} V_i^{2/15}$ for a fixed expansion angle. Therefore the ratio of propagation distance can be estimated as 21 times smaller in our case using this equation which is very close to our observed ratio of 19 times.

At low background pressures, past reports have shown that the two components of the laser ablated plasma plume are found to propagate at an average velocities of $\sim$ 0.8 - 2.4 $\times 10^4$ m/s [206, 208, 213, 217, 218] and $\sim$ 1 - 5.2 $\times 10^2$ m/s [206, 213, 221] for fast and slow components respectively for a wide range of pulse energies with nanosecond and femtosecond laser pulses. Although at very low background gas pressure, femtosecond pulses show slightly higher plume propagation velocity than the nanosecond cases e.g. 2×10^4 m/s for fs pulses compared to 1.4×10^4 m/s for ns pulses for Ca(I) species as reported in the literature [208]. In the case of nanojoule laser pulse energies we have observed similar velocity behavior of the two components of the plasma. Amoruso et. al. [222] have used MD simulations coupled with a two-temperature model to study the ablation process due to 300 fs laser pulses. The simulations predicted a most probable velocity of $\approx 1 \times 10^4$ m/s for the fast component and $\approx 3 \times 10^2$ m/s for the slow components of the expanding plasma plume into vacuum. The average velocity of the plume front decreases with increasing background pressure.

The evolution of plume propagation with time has been described by the

blastwave model and drag model in many of the past experiments. A general form of expression of $R \propto t^n$ for the blastwave model has been used in past to compare experimental data in nanosecond [200, 202, 223] and femtosecond [208, 224] laser plasma cases where n $\sim$ 0.4. The pressure value where this model fitted best was reported as $\sim$ 11 torr with $\sim$ 40 mJ, 10 ns (FWHM) laser pulses by Dyer et. al. [200] and 15 torr with $\sim$ 47.5 mJ, 8 ns (FWHM) laser pulses by Mahmood et. al. [203] respectively. In our case, the blastwave model has been used with the exact values of each parameter and assuming an estimated 50% energy absorption. The plasma plume expansion can be temporally divided into different regimes: initial ballistic expansion, collisional expansion and stagnation. For the lowest pressure case of 0.3 torr a predominantly ballistic expansion is observed as would be expected when there is little collisional coupling. For the collisional regime the time span for a pure blast wave expansion is short due to the initial period of ballistic expansion and the fairly rapid onset of stagnation. Therefore deviation from an ideal blast wave solution is expected at the lower background pressures where the ballistic expansion period represents a significant fraction of the overall plume expansion time but at the same time good agreement is observed at a background pressure of 52 torr.

In all but the lowest pressure cases a drag force model can be applied with a good agreement to the measured data. In most cases reported earlier the drag model fits better at all background pressures specifically on or above $\sim$ 10 torr [202, 223]. This model depends on the value of β, the damping coefficient at a particular gas pressure. As β determines the amount of resistance by the background pressure, it changes with different pressure values as shown earlier. From previous studies, various values of β were estimated as 0.0003 ns^{-1}, 0.002 ns^{-1} and 0.04 ns^{-1} for the background pressures of 0.1 torr [216], 1.3 torr [217] and 10 torr [223] respectively. We also have found that β changes from 0.06 ns^{-1} to 0.15 ns^{-1} as background gas pressure changes from 5.5 torr to 52 torr. We

can expect that β scales approximately linearly with the background pressure since it depends on the damping of the expansion in the background gas. Such an approximate scaling is seen from the past references and our β values falls close to these values irrespective of the fact that the references have used high energy nanosecond laser pulses in comparison to our fs, nanojoule pulse. The higher value of this damping coefficient β at higher background pressures would be due to higher resistance exerted by the neutrals of the background gas on the expanding plasma plume. This increased resistance causes confinement of the plasma near the target surface at high pressure.

6.5 Conclusion

In this work, plasma plume characteristics have been investigated in the regime of low incident laser pulse energies appropriate for precision micromachining and high resolution microLIBS. The spatio-temporal evolution of the plasma plume at different ambient pressures show that the plume shape changes from flattened, to spherical to forward directed as the pressure changes from high to a low value. The angular distribution of the plumes has been characterized both in the terms of conical width and best fit cosine power law functions. Splitting of plasma plume into two distinct slow and fast components was observed at pressures of $\sim$ 100 torr and below. These two different components of the plume have been identified as the rapid ion driven expansion plume and the much slower atomic vapor plume which eventually would condense into a nanoparticle cloud as observed in previous experiments at late time. The velocity of the ionic and atomic vapor plumes were 1.2×10^4 m/s and $\sim 1 \times 10^2$ m/s respectively. At pressures of $\sim$ 50 torr a blast wave model fitted the plume expansion fairly well. At lower pressures of 5 to 50 torr an expansion drag model fitted the data fairly well with appropriate choice of the drag coefficient β in the range of 0.06 ns^{-1} to 0.15 ns^{-1}. At very low pressures the

plume propagation is initially almost ballistic with a constant velocity and then slows down in time. The maximum plume length was calculated based on a pressure balance model and compared well to the experimentally obtained values at higher background pressures. At lower pressures it appears that the adiabatic expansion starts from a displaced point in the background plasma leading to a plume emission length which is close to the value predicted by the adiabatic expansion model. Plume images were also studied down to the emission threshold fluence of approximately 13 J/cm^2 and the emission lifetimes found to scale from 11 ns to 22 ns for energies of 26 to 111 nJ respectively.

Overall the behavior could be described well with a combination of models including ballistic expansion, blast wave expansion, collisional drag expansion and pressure stagnation of the expanding plume. The dominant behavior depends on the pulse energy, the background pressure and time of observation. This description is consistent with observations of plume dynamics previously reported for higher laser pulse energies. A more complete understanding of the expansion dynamics would require numerical modeling of the expansion processes over all the above regimes. However, this is left for future work. It is also expected that these results will be useful in application areas of such low energy plasmas such as femtosecond pulsed laser deposition, precise laser micromachining, laser induced breakdown spectroscopy and production of nanoparticles.

Chapter 7

Detection of Buried Layers in Silicon Devices Using LIBS During Hole Drilling*

This chapter investigates blind hole drilling using femtosecond laser pulses with LIBS technique to detect buried layers. The experimental studies were carried out on a series of test samples with thin chromium and copper metallic layers buried under a 10 - 60 μm thick silicon overcoat layer. A short-pulse femtosecond laser was used to generate an access hole through the silicon to the buried metallic layer. A sensitive spectrometer system has been used to measure the spectral emission from the laser induced plasma and determine the material characteristics at each depth. Two different focusing lens systems were used to create either a Gaussian beam profile with small focal spot or a flat top beam profile with larger ablation diameter. The smaller focal spot gives higher drilling rates, whereas, a large uniform intensity flat-top beam profile gives a slower drilling rate with better accuracy. An average drilling rate per shot of the order of 1 μm was obtained for the Gaussian beam profile and

* The main results of this chapter have been published in Ref. [154]. They are reproduced here with permission.

down to 30 nm per shot was achieved with a flat top profile. These numbers also indicate the depth resolution achievable in these two configurations. The results demonstrated in this chapter were published in Ref. [154].

7.1 Introduction

The advantages of ultrashort femtosecond laser pulses for high quality precision micromachining over nanosecond pulse duration lasers [175, 225, 226, 227, 228, 196] are desribed in Chap. 2.3.1. High quality and precise manufacturing of microstructures make these types of lasers an ideal choice for micromachining applications as well as in industrial applications [229, 230, 231].

Hole drilling is one application which has been well established and well documented using femtosecond lasers. In most of the industrial applications we need fast processing speed, efficient drilling and high quality holes. When drilling deep holes into a material, knowledge of removal and redeposition of ablated products from the capillary shaped hole is required. Many process parameters and laser parameters important for hole drilling have been studied in past [232, 233, 234, 235, 236]. Sven Döring et al. [237, 238, 239] have shown the characteristics of hole formation during consecutive stages of the drilling process with different laser parameters. They also have shown the dependence of maximum achievable depth of the holes on pulse energy. Melt dynamics, evolution of hole depth and shape in short pulse laser ablation drilling has been demonstrated by various authors [240, 241, 242]. The influence of polarization on the hole cross section [243], high speed laser percussion drilling [244] and ultra-fast pulse train burst hole drilling [245, 246] have also been studied.

Deep drilling of blind connection holes with femtosecond laser pulses and detection of the material sample layers while drilling is of current importance. Drilling in metals [234], semiconductors [233, 237] and semi transparent or transparent samples [247, 248] has been demonstrated by various authors and

highlight the characteristics of hole evolution. Our experimental aim was to detect emission of a buried layer in a multilayered target sample as a signature of reaching the layer. An example application would be to make electrical contact with a buried metallic conductor layer. The results also demonstrate the capability of depth profile measurement using Laser Induced Breakdown Spectroscopy (LIBS) while drilling deep holes with a short pulse femtosecond laser. Depth profile measurements where spectral information obtained from laser ablation at different depths using LIBS in order to measure the material composition has been demonstrated by several researchers [97, 105]. Metallic layers of micron size thickness or less on top of silicon wafer have been used as a target material in most of the cases.

We focus our work on creating laser drilled holes into silicon with deeply buried metallic layers. Silicon is the building block of most integrated circuits in the electronics and semiconductor industry. It is also one of the main materials of choice for fabrication of Micro Electro Mechanical Structure (MEMS) devices. Availability of cheap high quality material, ability to withstand high temperature and well developed processing techniques make silicon the most popular material for these applications. Hardness of silicon is high and thus suitable for laser machining as well. Semiconductor devices are fabricated of sandwiched layers of different metals or semiconductors. Identification of a metal layer under a thick silicon covering layer or dielectric overcoat layer and establishing a blind connection hole needs precise drilling through these materials and information about the emission characteristics of the materials at different depth. This can be obtained by monitoring spectroscopic signatures of the ablation process and such a smart micromachining approach can benefit the fabrication of microelectronic, microfluidic, flip chip and MEMS devices.

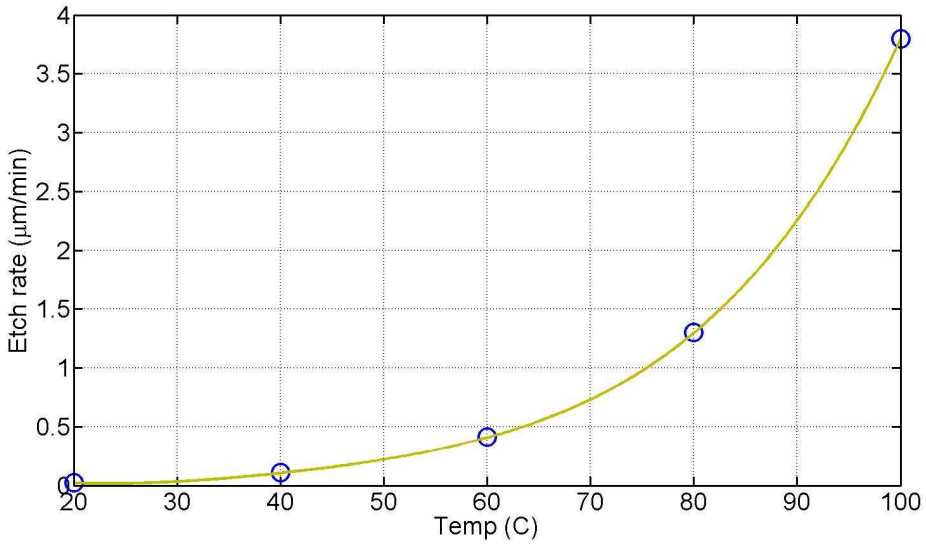

Figure 7.1: Etch rate versus temperature of the etching solution (30% KOH : 70% H_2O) [249].

7.2 Experimental Procedure

Copper is one of the most common conduction materials used in fabrication of microelectronic devices while chromium is often used as a binding layer to deposit other metal layer. Chromium and copper are also widely used as tracer layers for detection using spectral emission coming from a laser induced plasma. We have used these two metals as signature layers under a thick layer of silicon for our studies. A planar magnetron sputtering system has been used to deposit a thin layer of Cr (300 nm) on top of a premium silicon wafer (100 μm thick). Another layer of 150 nm of Cu was deposited on top of chromium. The Cu side of the sample was attached onto a glass slide with super glue (Ethyl 2-cyanoacrylate). The top silicon surface was then etched to the desired thickness with wet-chemical etching using a KOH solution. The etch rate depends on the crystallographic orientation of the silicon, KOH concentration and the etching solution temperature. The estimated etch rate was calculated from the data [249]. We used a concentration of 30% KOH : 70% H_2O as an etching solution. Fig. 7.1 shows the etch rate versus temperature.

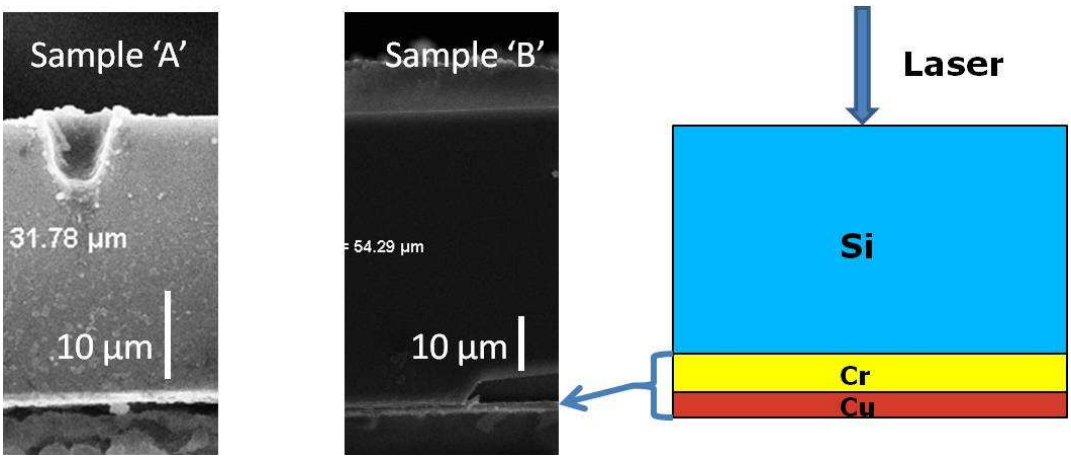

Figure 7.2: Sample A (left), sample B (middle) and schematic (right)

We prepared samples with different etched thickness of silicon by estimating from the etch rate calibration curves and then verified the exact thickness of the silicon layers using SEM measurements. We have used two different samples in this experiment. For sample A, we have inserted the sample into the etching solution for 70 minutes and the temperature of the solution was 76^o C. The expected etch rate of silicon at 76^o is 1.035 µm/min. Thus the estimated thickness etched was 72 µm and thickness left of $\sim$ 28 µm of silicon on top of Cr and Cu layers at the bottom. Sample B was inserted into the etching solution for 60 minutes and the temperature of the solution was 72.5^o C. The expected etch rate of silicon at 72.5^o is 0.844 µm/min. Thus the expected etched thickness was 51 µm and the remaining silicon thickness was $\sim$ 49 µm. SEM measurements of the experimentally etched samples are shown in Fig. 7.2. The measurement confirms remaining silicon thickness of sample A as 32$\pm$2 µm and 54$\pm$3 µm for sample B.

The experimental setup used for this experiment is shown in Fig. 7.3. A Ti:Sapphire (Spectra-Physics Hurricane) laser was used for our study to generate $\sim$ 120 fs (FWHM, assuming a Gaussian pulse shape) pulses at 800 nm with a maximum energy of $\sim$ 600 µJ. The laser pulse was focused onto the target sample using a 10X objective (Mitutoyo, Numerical Aperture 0.28, Working

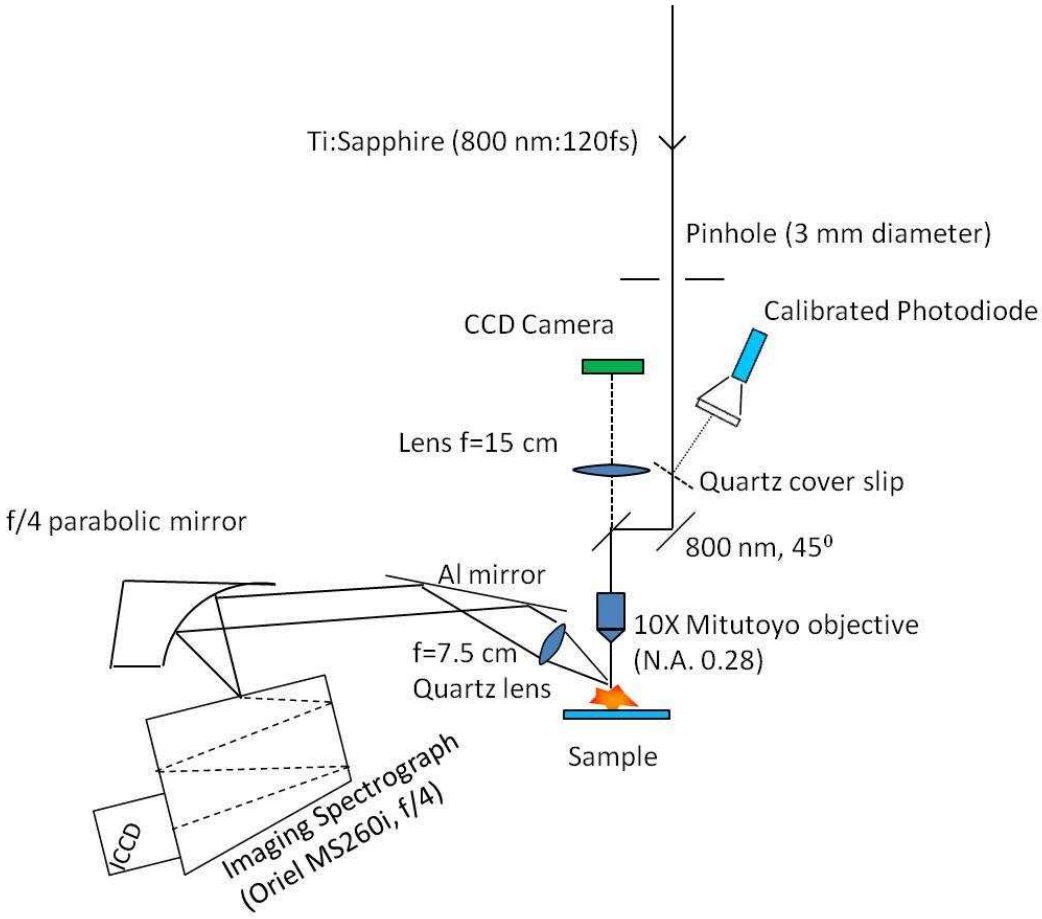

Figure 7.3: Schematic layout of the experimental setup

distance 33.5 mm, Focal length 20 mm). A 3 mm diameter hard aperture was placed in the laser beam well before the objective to obtain a diffraction limited focal spot. The focal spot intensity profile was an Airy function with 4.7±0.4 μm diameter (FWHM) for its central peak. The energy delivered to the sample was measured using a PIN photodiode (EG&G FND100) calibrated against a powermeter (Spectra Physics model 407A) and monitored for every set of experiments. The LIBS plasma emission was collected by a 7.5 cm focal length quartz lens with 2.5 cm diameter aperture and imaged onto the entrance slit of a spectrometer (Newport MS260i) with an f/4 parabolic aluminum mirror. A grating with 1200 lines mm^{-1} was used for spectral measurements. A large 400 μm entrance slit was used for all the experiments reported to capture sufficient emission from the plasma region. Spectra were recorded using a gated intensified CCD camera (Andor iStar ICCD). The targets were mounted in a commercial 3-D computer controlled precision micro-positioning system and translated perpendicular to the laser axis to move to new target positions as required. The image intensifier gate width was set at 200 ns to ensure that all the plasma emission was collected. The gate delay time was optimized and set within a 0.5 nanosecond of the laser pulse. Successive laser shots were taken at one location and the Si, Cr and Cu spectral emission lines emitted from the laser produced plasma were monitored. A CCD camera (Point Grey Chameleon USB camera) in conjunction with an f = 15 cm achromatic lens viewing through the same 10X Mitutoyo objective and through a turning mirror was used as a sample viewing system to make sure that the sample surface was at the focus of the input beam.

Laser drilling starts from the silicon side and then reaches the chromium and copper layers. Buried metal layers were identified by repetitive laser ablation on a single spot and measuring the spectral emission until emission from chromium and copper was observed. An intense silicon line (288.15 nm) appears during the initial ablation period and then after a number of successive shots the

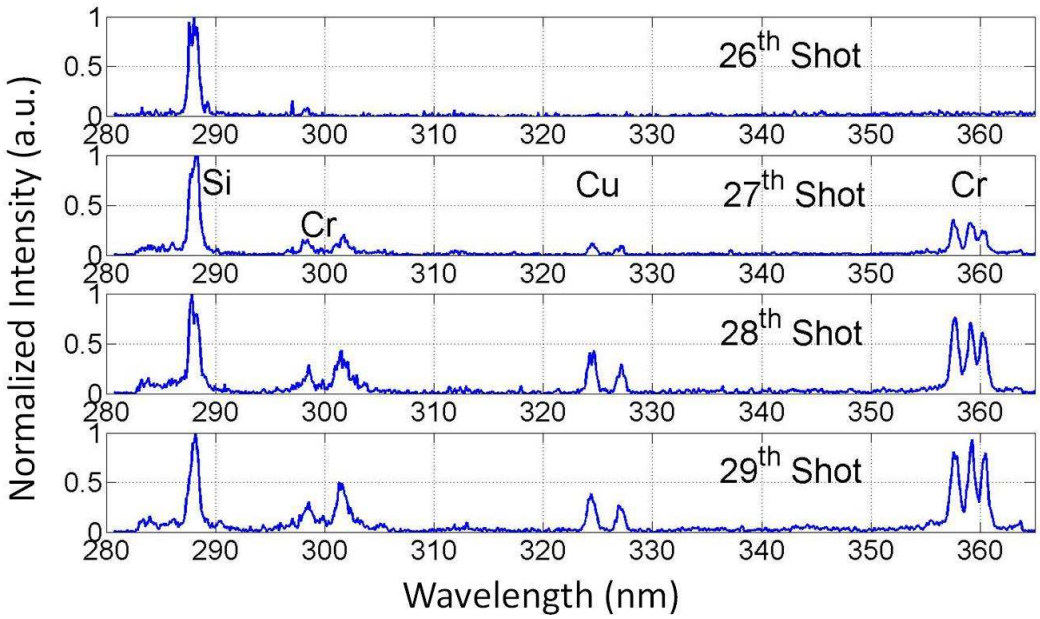

Figure 7.4: Drilling hole through a 32 μm thick Si and spectra obtained at successive laser shots with 16 μJ pulse energy

sudden onset of chromium (357.86 nm, 359.35 nm, 360.53 nm) and copper (324.75 nm, 327.39 nm) emission lines was observed. Average ablation rates were then calculated for different experimental conditions.

7.3 Results and Discussion

We started our experiment with sample A where we have 32 μm of silicon over the Cr/Cu layer. Successive single laser shots with constant laser pulse energy were taken at one location and spectra were recorded for each shot. The same operation was repeated for various laser fluences. The ablation rate near the surface depends on the fluence for fixed pulse duration.

Fig. 7.4 shows the single shot LIBS spectra obtained from laser plasma with laser pulse energy of 16 μJ per pulse. The four consecutive shots represent features from 26^{th} to 29^{th} shot. It is quite evident from the figure that the silicon line dominate until the 26^{th} shot as we do not see any chromium or copper lines. Three distinct peaks of chromium at 357.86 nm, 359.35 nm and 360.53 nm and

two copper lines at 324.75 nm and 327.39 nm appear at the 27^{th} shot. We also see the presence of other two peaks of chromium at 298.64 nm and 301.75 nm as we reach the chromium layer. This confirms that we have drilled 32 μm of Si and entered into the layer of Cr and Cu. Each LIBS spectrum is normalized to the maximum value of the particular spectra. The strength of emission of the Cr and Cu lines increased for a few shots as we continued to ablate deeper into the sample. Thus we see stronger peaks of Cr and Cu in the following shots. The signal observed in these shots is due both to the slower ablation rate in the wings of the laser pulse and to the partial redeposition of material when drilling blind holes in a background atmosphere. The Cr and Cu line signals were subsequently observed to fade to the background level over about 20 shots after the first line signatures were observed. The average ablation rate per pulse has been calculated by dividing the thickness of the Si layer by the number of shots to reach to the buried layer. This gives an average value of 1.18±0.05 μm per pulse for this pulse energy. We only have 300 nm of Cr layer sandwiched in between Si and Cu layers. Since the laser drills through more than a micron in one shot, we could not differentiate between Cr and Cu layers. The average ablation rate must be less than the thickness of the layer to be observed in order to isolate it from the other layers. Different laser pulse energies give different average ablation rates as shown in Fig. 7.5. Cr and Cu lines appear at the same time because of the high ablation rate per shot for each case. Higher numbers of shots were needed at lower fluences with lower average ablation rate to reach the buried metal layer. Increased fluence lowers the number of shots as expected. The average hole sizes ranged from 9 to 11 μm in diameter at the entrance surface for energies of 5.1 μJ to 25.8 μJ/pulse. In these cases, the average ablation rate was calculated using spectroscopic signature of the buried elements present in the sample.

In order to determine the actual average ablation rate in a different manner we have carried out another set of experiments. In this case we took out a small

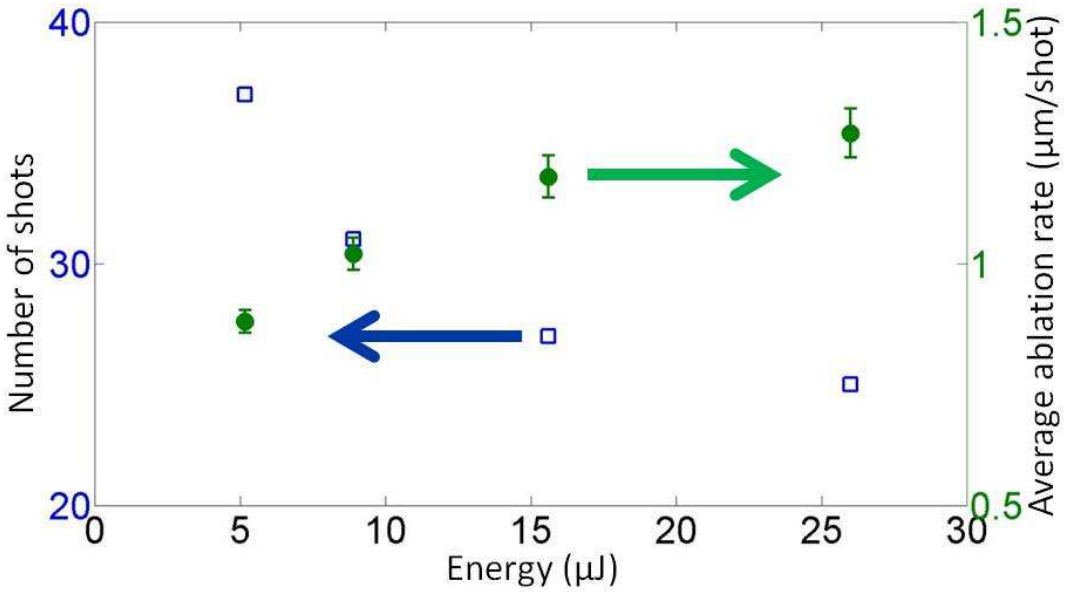

Figure 7.5: Number of shots until the first appearance of the Cr and Cu lines (open squares) and average ablation rates (solid circles) for different energies.

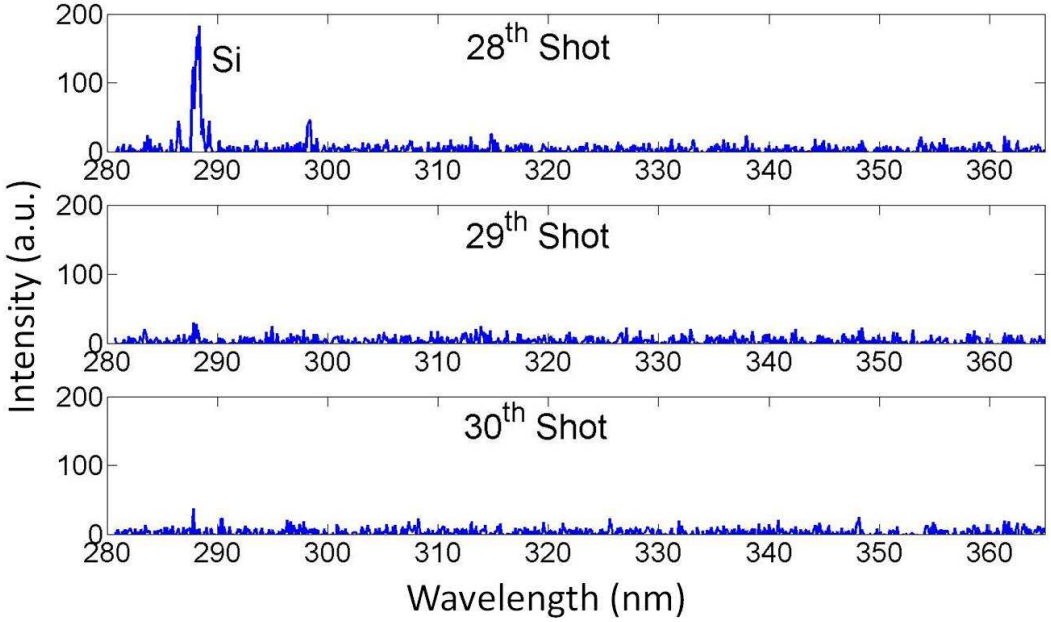

Figure 7.6: Drilling a through hole without any back support using a 32 μm thick Si and spectra obtained at successive laser shots with 9.1 μJ pulse energy

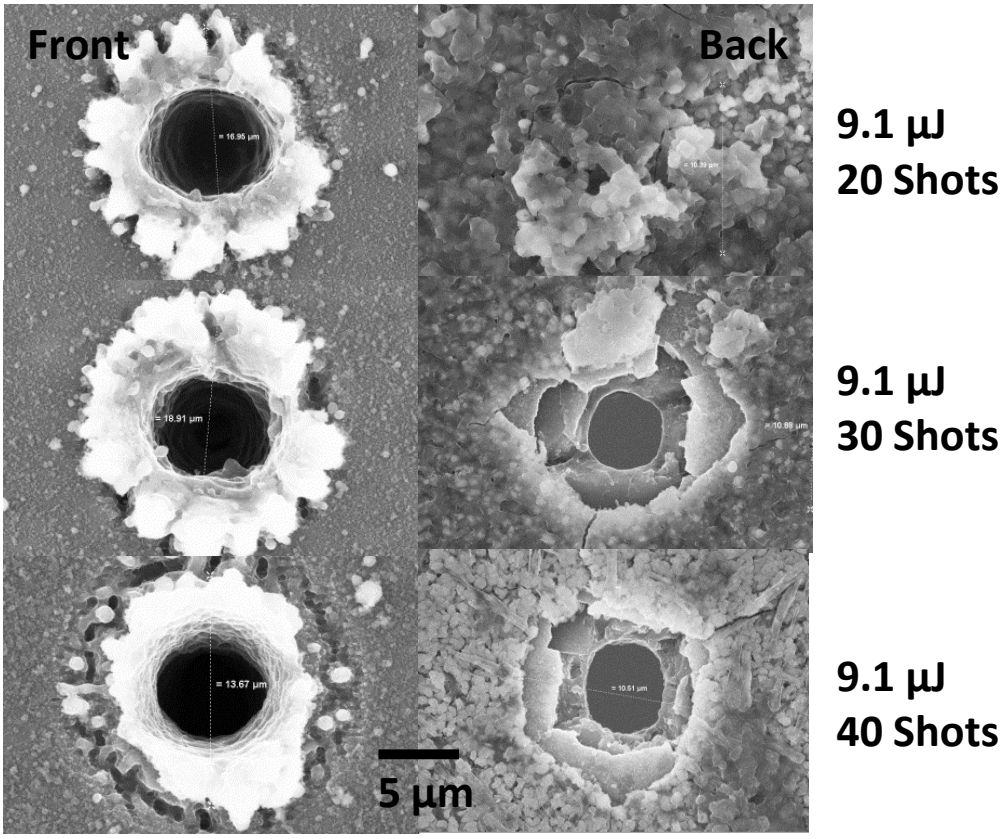

Figure 7.7: Front and the back side images of the target sample after 20, 30 and 40 shots

piece of the target sample from the glass slide so that we can place the sample in free air without any support on its back. Absence of back support would result in a through hole in the sample after repetitive drilling. We compared the number of shots in order to get a through hole with the corresponding number of shots to observe the buried layer spectra. Sample A was used for this experiment. The laser was focused on the silicon side of the sample while drilling. We used three different energies of 5.1 μJ, 9.1 μJ and 25.8 μJ for this case. Fig. 7.6 shows single shot ablation LIBS spectra for 9.1 μJ. We see silicon spectra were available until the 28^{th} shot and then disappear suddenly. We did not see any spectral information thereafter. This indicates that we should see a through hole at 29^{th} shot from the SEM images of the sample. Fig. 7.7 shows front and back side images of the target sample after 20, 30 and 40 shots. The back side of the sample shows a fracture after 20 shots and a through hole was visible after 30 shots. This is consistent with penetration through the sample on the 29^{th} shot.

It is interesting to note that the Cr and Cu line signatures are not seen in these shots which is probably due to two reasons. Firstly, there is a significant shock wave driven into the target as can be seen in the surface damage seen on the backside after 20 shots in the SEM image shown in Fig. 7.7. This shock wave will damage and spallate material from the backside of the target prior to the ablation front reaching the backside. Thus the Cr and Cu layers may already be removed prior to the final breakthrough ablation shot. As can be seen in the SEM backside image of the 30^{th} shot shown in Fig. 7.7, the surface layer has been removed over a region larger than the ablation hole and thus at this point no Cr and Cu could be excited by the laser pulse. The second reason is that the final ablation shot would drive the plasma primarily forward and very little plasma would expand back towards the laser. Thus the signals from the Cr and Cu layer would be significantly weaker and thus perhaps below the background level for this final breakout shot.

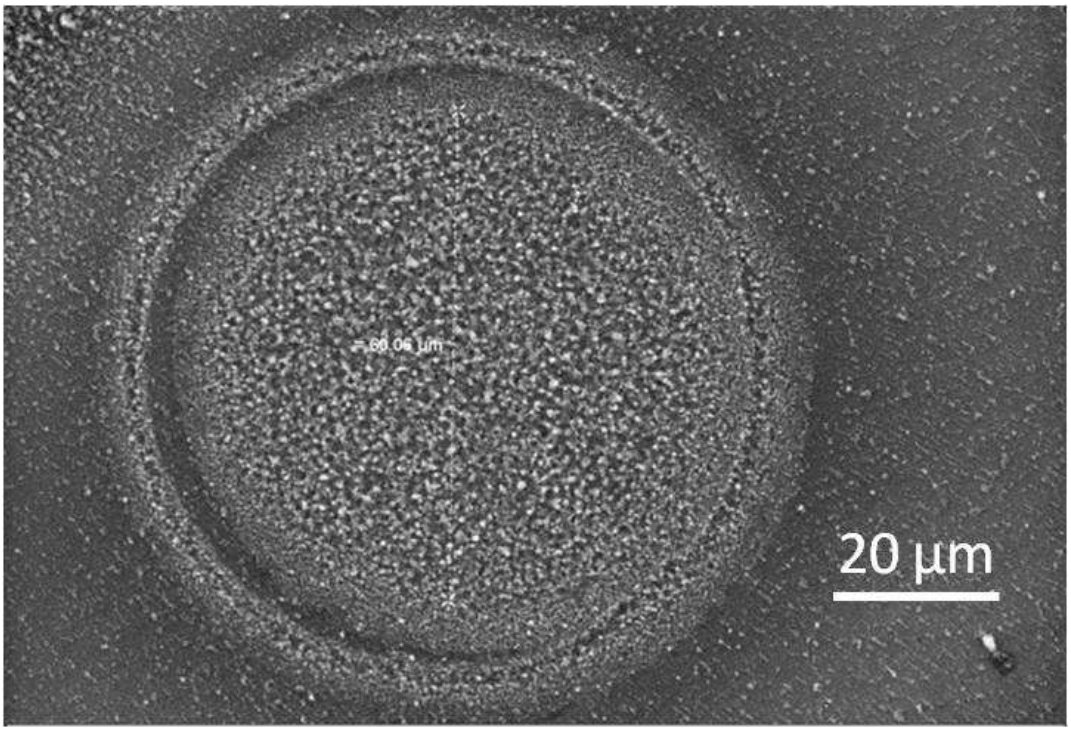

Figure 7.8: SEM image of the single shot ablation crater with the flat-top spot size

There is a trade off between depth resolution per shot and number of laser pulses required. If we want higher resolution, we need to use more shots and the processing will be slower. A lower average ablation rate per shot with more accurate information about the location of a buried layer can be achieved by modifying the laser spot into a lower intensity flat-top spatial profile. We have achieved such a flat-top energy profile and a larger focal spot by imaging the pinhole onto the target surface. In addition to having a lower ablation rate per shot we have a larger surface plasma with a bigger focal spot. Therefore, we expect to still have a reasonable spectral intensity by integrating over the larger emission plasma. In order to obtain sufficient signal to noise ratio from a single shot emission at lower fluence, the larger spot is needed as well. The flat-top spot diameter used was ~ 60 µm as shown Fig. 7.8.

We have used laser pulse energy of 38 µJ in the next set of hole drilling experiments for both sample A and B with fluence of 1.4 J/cm^2. The single

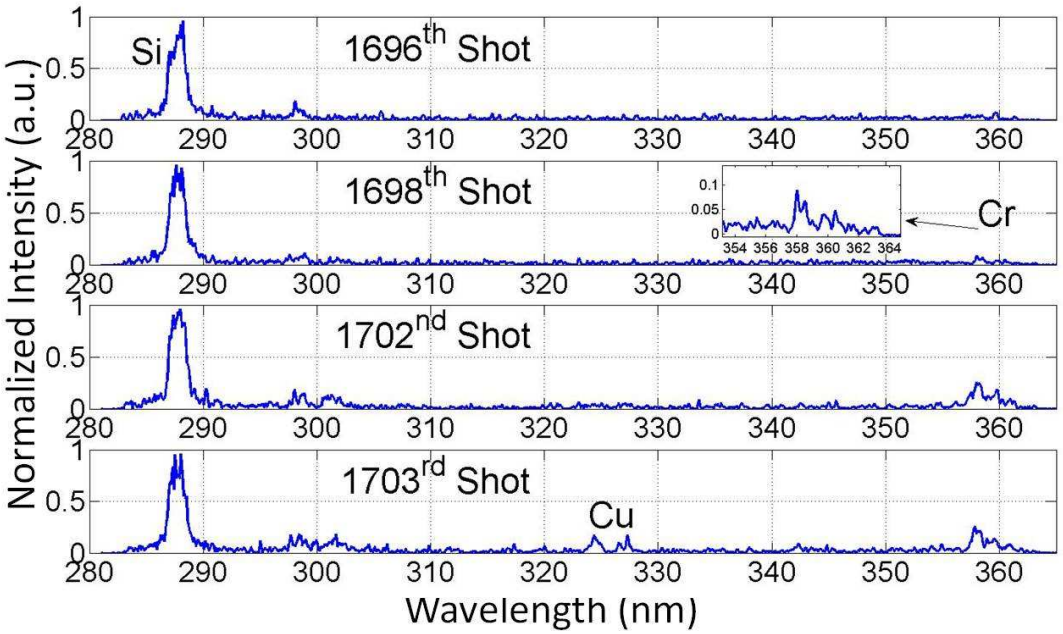

Figure 7.9: Drilling hole through a 54 μm thick Si and spectra obtained from successive laser shots with 38 μJ pulse energy

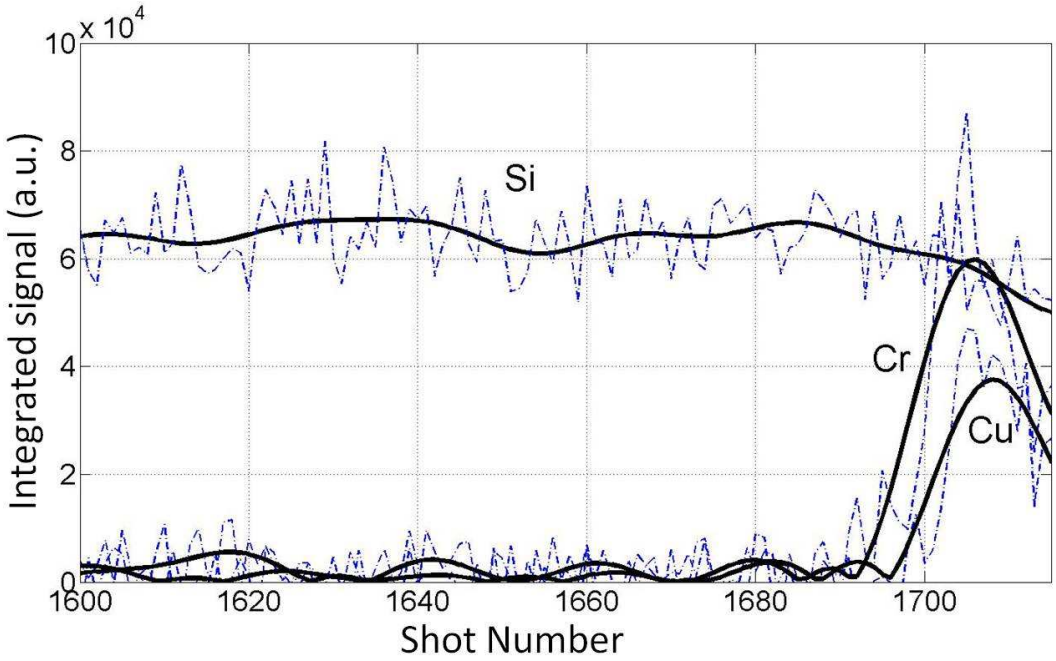

Figure 7.10: Integrated Si, Cr and Cu signals for different shots at different depth of the sample

pulse threshold fluence of silicon in air at 800 nm femtosecond pulses has been measured by several authors. Surface reflectivity changes at very low fluences and the minimum fluence needed to melt silicon without significant topographical surface modification or melt flow define a melting threshold fluence with a corresponding value as 0.27 J/cm^2 [250] to 0.3 J/cm^2 [179]. More energy will be required to ablate material out of the crater. The ablation threshold has been reported as 0.52 J/cm^2 [250]. Hwang et al. have demonstrated two different regimes while estimating ablation threshold fluence of silicon. The low fluence regime ($\leq$ 1.1 J/cm^2) and high fluence regime ($\geq$ 1.1 J/cm^2) with asymptotic thresholds of 0.458 and 0.637 J/cm^2 respectively [251]. Therefore, the fluence of 1.4 J/cm^2 in our case was sufficiently above these thresholds to provide enough emission from the plasma at our low fluence operating regime. LIBS spectra were recorded for each shot as earlier. Fig. 7.9 shows the single shot spectra we obtained for sample B with top silicon layer thickness of 54 μm. Cr signals appears at the 1698^{th} shot and Cu appears at the 1703^{rd} shot. The average ablation depth per shot in silicon which would also be the approximate precision with which is possible to resolve the location of a buried layer is 32 nm in this case. It took 1070 shots to reach the Cr layer for sample A (32 μm Si) at the same pulse energy. The average ablation rate in this case was 30 nm per shot. To demonstrate the transition from silicon to chromium and copper layer, we have integrated the spectral signal obtained for these three materials for each shot and plotted against corresponding shot number. Fig. 7.10 shows the integrated intensity profile curves. The silicon intensity starts dropping down as we reach the chromium layer. The chromium intensity peaks up first and then we reach the copper layer. Cross sectional views of the actual ablation holes for different shot accumulations is presented in Fig. 7.11. We have taken 250, 500, 750, 1000, 1250 and 1500 continuous shots and measured the final depth using SEM imaging. The crater bottom shows a rough surface texture at low fluence as reported earlier [252]. We see similar bumpy struc-

tures at the bottom of the crater. To make comparable depth measurements for all the craters, we have taken the top layer of the uneven surfaces as our reference height for the bottom layer. The depths obtained were 10 μm, 15 μm, 22 μm, 26 μm, 30 μm & 37 μm respectively. Deep drilling of materials show three different phases of drilling as reported in the literature [237, 253]. Higher ablation rates occur in the first phase of the hole depth development from the start of drilling to approximately 200 pulses and reduced hole growth rate occurs in the next phase which typically goes up to 7000 pulses as was previously reported [237]. We see similar behavior for the evolution of the hole depth. The first 250 shots give 40 nm ablation depths per shot which reduces to 21 nm per shot for the next 1250 pulses. The average drilling rate for the deep drilled hole would be around 25 nm per shot. This is lower than the spectroscopically measured ablation rates which correspond to the bottom surface of the ablation front.

The two temperature diffusion model can describe ultrafast laser processing and can be used to calculate the ablation depth per pulse as [254]:

$$L \approx l.\ln(\mathrm{F}/\mathrm{F_{th}}) \tag{7.1}$$

Here F_{th} is the ablation fluence threshold, F the laser fluence and l is the optical penetration depth which is given as 9950 nm at 800 nm laser wavelength [168]. Depending on the different ablation behavior at low and higher fluecnes, the optical penetration depth (l) can be replaced by an effective light penetration depth (l_{eff}). Ablation depth is dependent on laser fluences with both a low and high fluence regimes. The effective penetration depth also varies for these two regimes. In the low fluence regime the value of effective penetration depth of silicon at 800 nm laser pulses has been given as 145 nm [251], 135 nm [255] whereas in the high fluence regime the effective penetration depth has been given by higher values of 322 nm [251], 324 nm [255]. We have worked in two

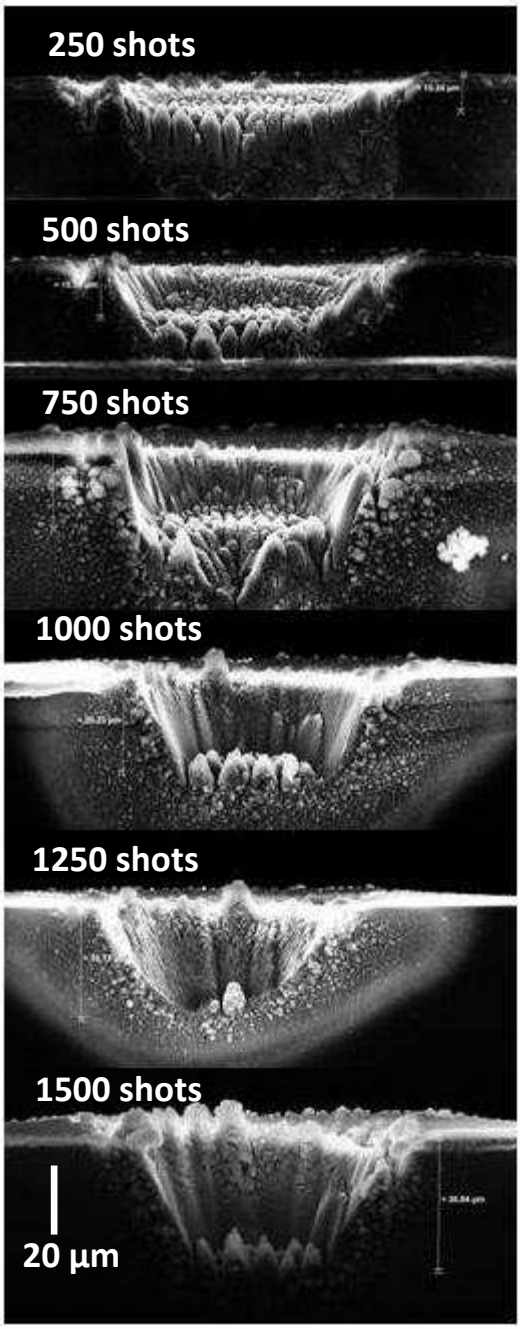

Figure 7.11: Cross sectional view of the ablation hole for different shot accumulations at a fluence of 1.4 J/cm^2

different fluences in this experiment. An airy function laser pulse of 16 μJ with a 9 μm spot diameter leads to a peak fluence of about 42 J/cm^2. The experimental value of average ablation rate was 1.18±0.05 μm per pulse. If we want to calculate the effective penetration depth from Eq. 7.1, we need to know effective ablation threshold fluence of silicon in this regime. The ablation threshold fluence value at high fluence regime was reported as 0.637 J/cm^2 [251]. We get an effective penetration depth of 282 nm if we take the same ablation threshold value to for calculation. This is a lower value than what has been reported in the literature caused by the fact that we take an average ablation depth over many shots instead of a single shot ablation depth. The other reported values were measured with single shot ablation. In the low fluence regime 38 μJ of pulse energy was distributed over a flat-top spot diameter of 60 μm. Therefore the fluence was 1.4 J/cm^2 and the average ablation rate was 30 nm per pulse. Different ablation threshold fluences for silicon in this low fluence regime are reported in literature. Korfiatis et al. have done numerical modeling to estimate the single shot ablation threshold value for silicon. Their calculated value was $\sim$ 0.52 J/cm^2 [256] at 800 nm with 120 fs laser pulses. The experimental values with similar experimental parameters resulted in 0.458 J/cm^2 [251] and 0.52 J/cm^2 [250]. We can take an average ablation threshold value of 0.5 J/cm^2 to calculate the ablation depth. The other important factor in this near ablation threshold is two photon absorption. Thus, we need to take the two photon absorption co-efficient (β) into account while calculating the ablation depth. Inclusion of two photon absorption leads to the following equation for intensity versus depth:

$$\frac{dI(x)}{dx} = \alpha.I(x) + \beta.I(x)^2 \tag{7.2}$$

where I(x) is the laser pulse intensity at depth x which decreases as we go deeper into the sample, α is the linear absorption coefficient and β is the two

photon absorption coefficient. Integrating this equation will give the depth versus intensity which then can be used to define the ablation depth, $L_{ablation}$, where the intensity equals the value of the ablation threshold intensity, I_{th}:

$$L_{ablation} = \frac{1}{\alpha} \ln \left\{ \frac{\mathrm{I}.(\alpha + \beta.\mathrm{I_{th}})}{\mathrm{I_{th}}.(\alpha + \beta.\mathrm{I})} \right\} \tag{7.3}$$

To obtain the threshold intensity we have to multiply external threshold intensity by a factor of (1-R) (i.e. corrected for the reduction due to reflection upon entering the sample), where R = 0.34 [168] is the normal incident surface reflectivity. If we use the ablation threshold fluence of 0.5 J/cm^2 this corresponds to a threshold intensity inside the sample of 4.17×10^{12} W/cm^2 for a 120 fs pulse. Then for an incident fluence of 1.4 J/cm^2 corresponding to an incident laser intensity of 1.17×10^{13} W/cm^2, using α^{-1} as 9950 nm and $\beta = 50 \times 10^{-9}$ cm/W [257] we get the value of single shot ablation depth as 46 nm. This value is quite close to what we have achieved from our experiment. Our experimentally measured value of average ablation depth per shot in the first 250 shots is 40 nm.

Next, we have calculated the total approximate ablated volume from the crater for the two fluence regimes to determine the ablation efficiency. Ablation efficiency is known as the removal volume per unit pulse energy. We needed 27 shots to drill 32 μm of silicon with 16 μJ laser pulses. The crater shape would be cylindrical with a curved bottom due to the airy function shape of the incident laser pulse. Taking the diamater of the hole as 9 μm, the volume could be calculated as 2028 μm^3. Dividing this by the number of shots and incident energy, we get an ablation efficiency for silicon at the high fluence regime as 4.7 μm^3/μJ. In the second experiment we needed 1700 shots to drill 54 μm of silicon with 38 μJ laser pulses. A 60 μm diameter crater would lead to a volume of 1.53×10^5 μm^3. The ablation efficiency in this case was 2.3 μm^3/μJ. Similar experimental parameters were used to ablate silicon at 800 nm

with 120 fs (FWHM) laser pulses in the energy range of 0.1 to 10 μJ. A best fit of the data of crater volumes at different pulse energies was used to calculate the approximate ablation efficiency of silicon as 3 $\mu m^3/\mu J$ [90]. Single shot ablation efficiency of materials change with the incident laser fluences. The ablation efficiency peaks at around 10 J/cm^2 and decreases on both higher and lower fluences [251, 255]. Single shot ablation efficiency of silicon with femtosecond laser pulses at 800 nm at $\sim$ 1.4 J/cm^2 give approximately 5 $\mu m^3/\mu J$ [251, 255]. This value increases to $\sim$ 9 $\mu m^3/\mu J$ [255] and $\sim$ 13 $\mu m^3/\mu J$ [251] at 42 J/cm^2. Ablation efficiency in our case is an average value over a large number of shots and therefore lesser than the reported values. Although the actual value of ablation efficiency is lower in our case, it increases twice the value at higher fluences than at lower fluences which is similar in trend to the earlier reported investigations.

7.4 Conclusions

The effectiveness of using femtosecond laser pulses and LIBS to carry out hole drilling through silicon along with spectroscopic material identification has been studied. We have shown that clear detection of a submicron buried layer inside a semiconductor material can be obtained with LIBS assisted precision hole drilling. Information about the depth of a buried layer inside thick semiconductor can be beneficial for the semiconductor and MEMS industries especially when trying to reach buried electrical conductor layers. There is a trade-off between resolution and processing speed when carrying out such drilling. A small ablation focal spot was created by focusing the truncated center part of the Gaussian laser pulses to obtain a high drilling rate of approximately 1 μm per pulse whereas a lower intensity flat top profile was used for lower rate drilling and better accuracy. A depth resolution of 30 nm was demonstrated for high precision determination of chromium and copper layer depths under

a thick silicon layer. Highly textured surfaces appear at the bottom of the ablated crater at low fluences and thus the value represents the leading edge of the ablation front reaching the metallic layer. In both cases the material removal efficiency were measured as 2.3 to 4.7 $\mu m^3/\mu J$ for the low and high fluence regimes respectively.

Chapter 8

High Resolution Scanning Microanalysis on Material Surfaces Using UV Femtosecond Laser Induced Breakdown Spectroscopy

The application of LIBS on lateral resolution is discussed in this chapter. Femtosecond lasers together with high resolution optics have given us the ability to achieve submicron ablation spots which can play an important role in specific micromachining applications. Light emitted from the plasma at the sample surface created by a focused femtosecond laser pulse can also be used in LIBS and allow us to characterize the chemical composition of the target surface with micron-level lateral resolution. The spatial resolution using LIBS has often been defined by measuring the FWHM of the crater size. We study the application of low energy femtosecond 266 nm laser pulses with very low energies of 10's of nanojoules. We have investigated spatial resolution using the detection of thin strips of chromium on silicon substrates and compared the

actual width of the chromium versus the experimentally obtained width using LIBS detection. The variation of signal levels for low pulse energies is investigated on Chromium surfaces. A spatial resolution of $\sim$1 μm was obtained for detection of chromium from the emission measured.

8.1 Introduction

The applications of LIBS in the regime of microanalysis are described in Chap. 2.4. Ultrashort laser pulses have the potential to produce a microplasma with a sub-micron ablation spot on the surface of a target material. Since lateral diffusion of heat from the ablated laser spot is small on the time scale of the interaction. Thus, femtosecond laser ablation is one prospective approach for lateral microanalysis with resolution on the micron scale. Material characterization and mapping can be performed by capturing and analyzing the emitted light from the laser produced micro-plasma which is known as microLIBS or μLIBS [90]. This technique can give information about the constituents on the surface of the target sample provided that one has sufficiently strong line emission and efficient light collection systems. Typically high resolution optical systems with large effective light collection efficiency and short wavelength lasers are required to achieve this goal. Working in the UV wavelength range enables much smaller sub micron focal spots and at the same time leads to enhanced absorption of laser pulse energy on most target materials including our target material chromium strips.

Material processing at the submicron level has been an important issue in the fabrication of miniature technology devices [258]. Pronko et al [259] first demonstrated machining of submicron holes using a femtosecond laser at 800 nm. They could achieve central ablation spot regions with a width as small as 300 nm. Fabrication of two and three dimensional high precision nanostructures on metal layers and transparent materials of the order of several

hundred nanometers have also been demonstrated with femtosecond laser pulses [260]. The spatial resolution using laser ablation is limited by the diffraction to the order of the laser wavelength. Different techniques have been demonstrated to allow reduction of the interaction region well below a wavelength. Recently nanogratings with sub 100 nm periodic nanostructures on materials have been been demonstrated by various groups [261, 262]. In addition, near field imaging applied to processing of crystalline silicon in the femtosecond pulse duration regime can even go down to a FWHM crater diameter of 27 nm as reported by Zorba et al [263].

To determine the elemental characteristics from the distinct emission lines and verify the materials involved in the laser-matter interaction, efficient collection of emission from the laser induced plasma created by a sub-micron crater is needed. Such emission may be very weak from these tiny craters and it has been observed that the threshold for LIBS is generally higher than that for ablation since ablation can occur without significantly populating the upper emission levels. Chap. 2.4.2 described a detailed survey on the past work done in this domain. The smallest ever reported single pulse ablated crater diameter width (FWHM) with LIBS signature was 450 nm [137]. Although the width of the crater gives an approximate size of the lateral analytical resolution obtainable with single shot LIBS emission, the droplet ejection from the crater, redeposition of the ejected particles in crater vicinity and shoulders of the crater can introduce some spread of the material and lead to a larger effective resolution size for LIBS scanning microanalysis. Therefore, it is important to carry out an investigation with a real sample with known lateral width and measure the width by means of LIBS signature. The limitation to the extent we can measure the lateral material width accurately will define the actual spatial resolution for real life samples. In this experiment we have scanned thin strip of chromium surfaces by UV femtosecond laser pulses and evaluated single shot emission spectra to obtain a spatial resolution of $\sim$1 μm.

8.2 Experimental

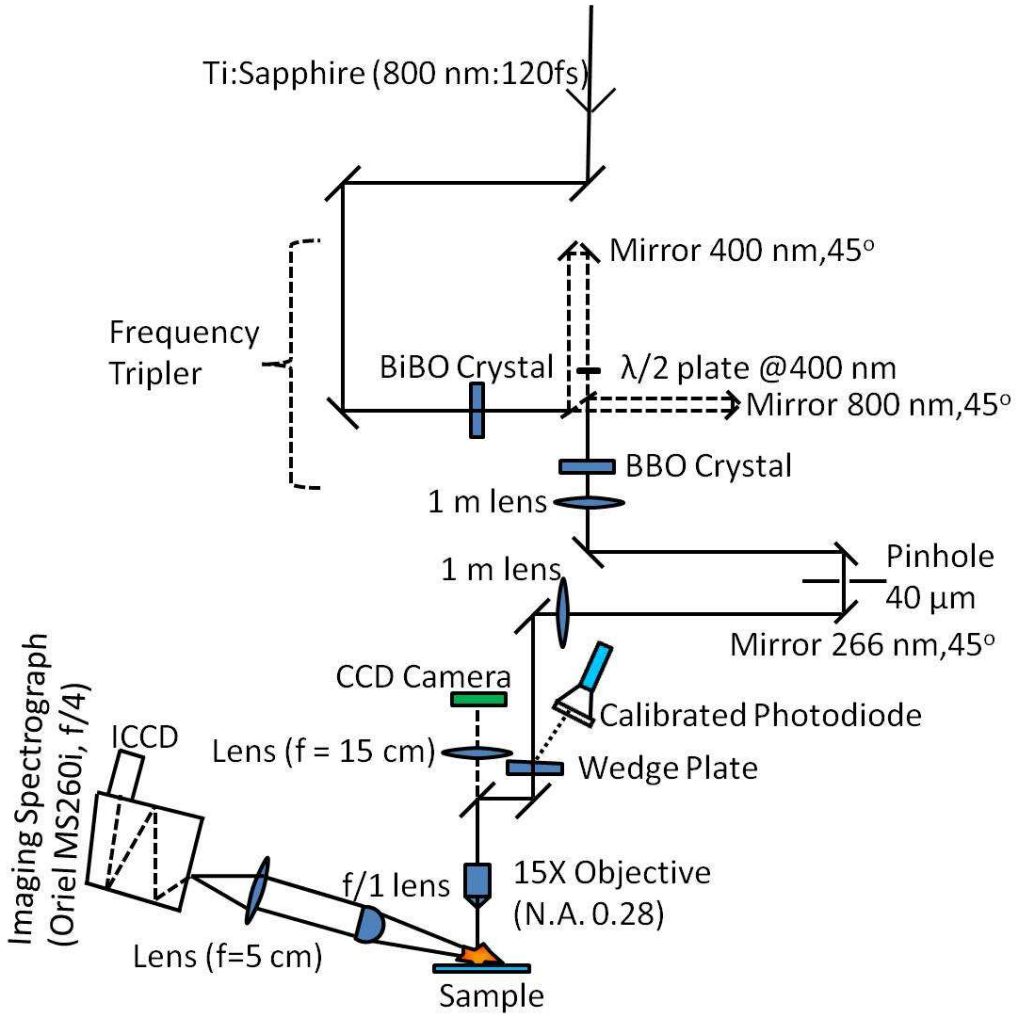

Figure 8.1: Schematic layout of the experimental setup

The experimental setup used for this experiment is shown in Fig. 8.1. The setup is similar as described in Chap. 4. The beam was focused onto the target sample using a 15X Schwarzschild objective (Reflective objective, Numerical Aperture 0.28, Working distance 24.5 mm). The effective spot size was estimated to be $\sim$ 570 mn (FWHM) as shown in Fig. 8.2.

Energy delivered to the sample was calibrated using a photodiode cross calibrated against a Spectra Physics model 407A powermeter and monitored for every setting of pulse energy in the experiments. The LIBS plasma emission

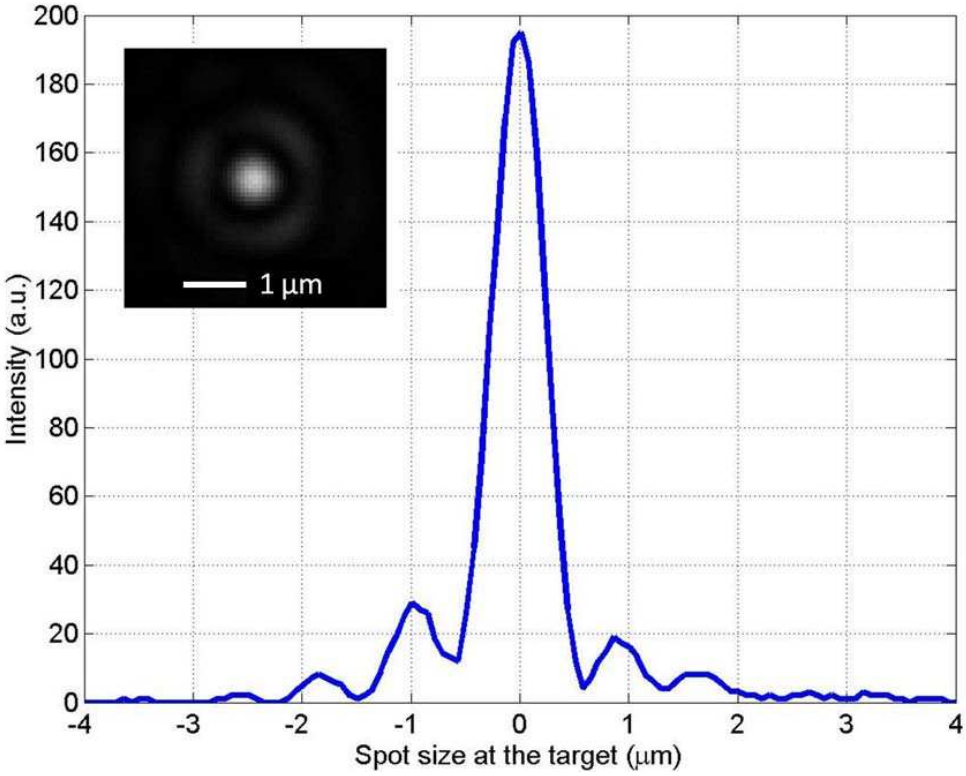

Figure 8.2: Intensity profile of the laser spot focused through a 15X Schwarzschild objective, which is measured with a UV 40X objective with N.A.=0.8. The inset image shows the actual spot image.

was collected by an f/1 aspheric lens (diameter 1 cm) and imaged onto the entrance slit of the spectrometer (MS260i) with a quartz lens of focal length 5 cm. A grating with 1200 lines mm^{-1} and a 1 mm wide entrance slit were used for the experiments reported. A large entrance slit was employed to capture a large fraction of the emission from the plasma region. Spectra were recorded using a gated intensified CCD camera (Andor iStar ICCD). The targets were mounted on a commercial 2-D computer controlled precision micro-positioning stage (Physik Instrument M-111.1DG PI stage) which translated perpendicular to the laser axis. The minimum incremental motion could be set as small as 50 nm. Therefore, the velocity of the stage could be controlled precisely and we were able to control the separation between two consecutive single shot laser pulses. The gate delay time was optimized for this nano Joule energy

regime which was set within a 0.5 nanosecond of the laser pulse. The observed lifetime for the plasma emission for this low energy regime is $\sim$ 5 ns. 50 ns gate width was employed to ensure that all the plasma emission was collected. A CCD camera (Point Grey Chameleon USB camera) in conjunction with an f = 15 cm achromatic lens viewing through the same Schwarzschild objective and through a turning mirror was used as a sample viewing system to make sure that the sample surface was at the focus of the input beam. We have used two different target samples for this work. For the first, a thin uniform layer of chromium (250 nm) was deposited on top of a premium Silicon wafer using a planar magnetron sputtering system. For the second target, a special mask was designed with which we could create chromium lines of varying widths of 1.5 μm to 10 μm on top of a pure silicon wafer. Our goal was to measure the LIBS spectra during the sharp transition from silicon to chromium and investigate the spatial resolution when analyzing these different chromium line widths.

8.3 Results and Discussion

We have used a thin chromium film sample to examine the ablation spot size and measured the crater size for very low laser pulse energies. Fig. 8.3 shows an SEM image of the ablation crater on the target sample at a laser pulse energy of 8 nJ. The internal crater diameter width at this low energy was approximately 700 nm as shown.

The plasma emission intensity depends on the size of the plasma at the surface [155] and reducing the surface area to a submicron level results in difficulty in acquiring sufficient emission spectra from the tiny plasma. The amount of detectable LIBS signal increases with the laser pulse energy as it generates a larger plasma but affects the lateral resolution by increasing the crater size. A study was carried out by varying the laser pulse energies from high to low values for obtaining spectral signature at minimum possible laser

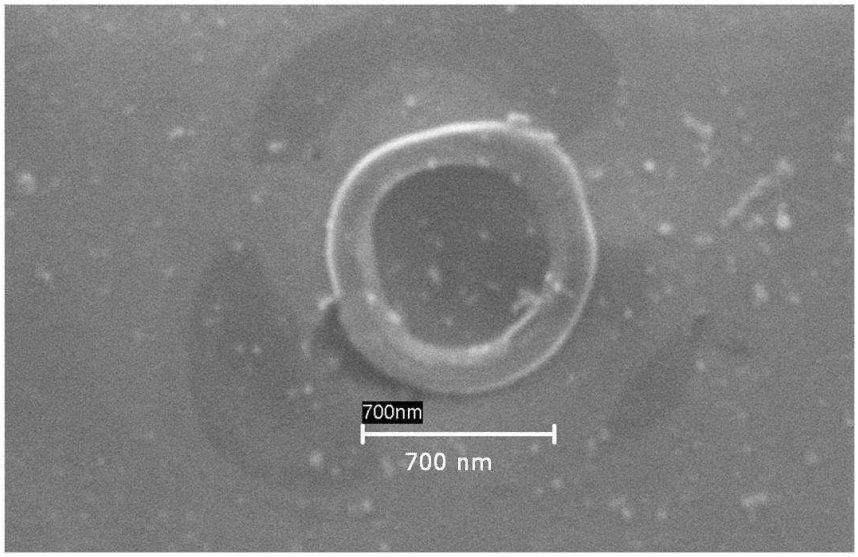

Figure 8.3: SEM image of ablated crater with incident laser pulse energy of 8 nJ.

pulse energy. LIBS signals were obtained with a minimum value of 27 nJ pulse energy. The crater width at this pulse energy was $\sim$ 950 nm. We also have varied the gate time delay at these pulse energies to study the spectral emission decay behavior with time. Laser energies of 27 nJ, 32 nJ, 47 nJ and 58 nJ were delivered onto a 250 nm thin film of chromium. For each energy, four different time delays, 0 ns, 1 ns, 2.5 ns and 4.5 ns were used, where time of 0 ns refers the onset time of the femtosecond laser pulse. For each time delay 100 shots were taken at each energy level. The shot to shot distance on target was 5 μm to avoid overlapping damage spots. The gate width was set to 50 ns. The signal detected by the ICCD detector over the wavelength range between 356 nm to 362 nm was integrated for each shot series in order to accumulate all chromium lines at 357.86 nm, 359.35 nm and 360.53 nm. The emission signal intensities for different gate delays and different incident energies are shown in Fig. 8.4. The emission intensity increases with pulse energy as expected. The signal intensity drops to (1/e) of its peak value within $\sim$3 ns at these pulse energies. Next, we have used our micro-LIBS setup to demonstrate the spatial resolution. A Si-Cr-Si pattern sample has been used for this experiment. The pattern has different Cr line widths on Si wafer. We have chosen a very thin

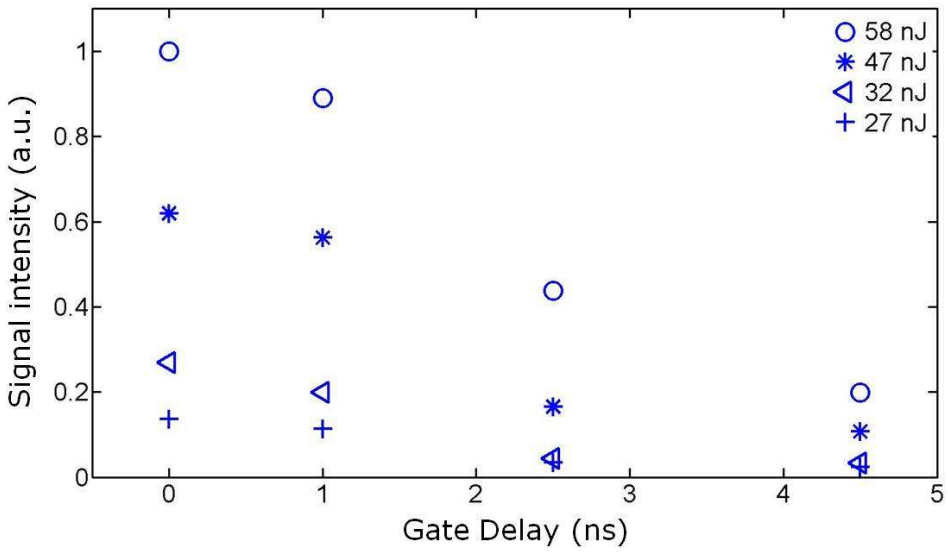

Figure 8.4: Integrated emission signal intensity versus gate delay at different laser pulse energies.

1.5 μm wide Cr line in this case. Fig. 8.5(a) shows a typical 1.5 μm wide chromium thin film measured by SEM.

In order to determine the width of the Cr patterns through LIBS signal measurements, a pulse energy of 27 nJ was used to scan across the pattern surface. The Cr emission lines between 356 nm and 362 nm were detected for each shot. The ablation was done on Si first, then Cr, and Si again at the end. Two different shot to shot distances of 250 nm and 500 nm were employed for this experiment to scan across the 1.5 μm Cr line. Four shot and two shot averages were taken for these two cases respectively to obtain one averaged data point for every micron of lateral motion. Fig. 8.5(b) shows a 1.5 μm wide Cr line after ablation with 250 nm step size. A typical single shot spectrum containing the chromium lines is shown in Fig. 8.6. The integrated spectral signal from 356 nm to 362 nm was calculated at each data point, i.e for every micron of translation. The experimental results are shown in Fig. 8.7. It can be seen that in the cases of 250 nm and 500 nm step sizes, the chromium signals appeared at the seventh sample point and continued to be visible until the tenth sample position. This gives a total 3μm Cr width for our target

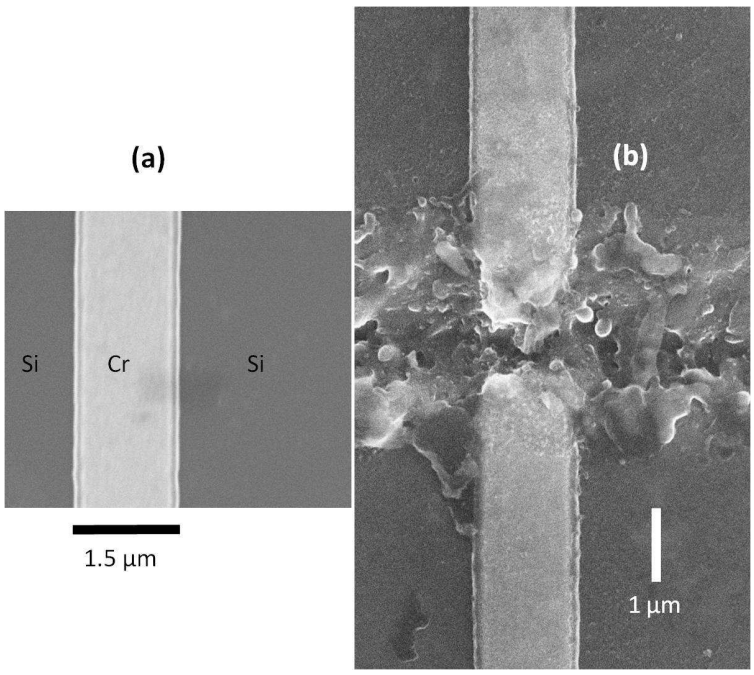

Figure 8.5: (a) SEM image of 1.5 μm Cr line fabricated on a Si wafer. (b) SEM image of 1.5 μm Cr line after scanning laser pulses with 250 nm step size across the line with 27 nJ pulse energy.

sample. A few smaller peaks of Cr emission near the strong Cr signals could be the contribution from the Cr signal of redeposited Cr particles on the Si wafer near the Cr film. Fig. 8.7 shows that the distance over which transition from 'no signal' to 'Cr signal' occurs within ∼1 μm and we can effectively measure the 1.5 μm Cr width as 3 μm giving an effective lateral resolution of ∼ 1 μm.

In order to test the signal stability, another experiment was done on the 10 μm wide Cr line using the same laser pulse energy. Similar shot to shot distances of 250 nm and 500 nm were taken and the results of the scanning using 4 shot and 2 shot averages were compared respectively. The experimental results are shown in Fig. 8.8. In this case the Cr signal appeared from 7th sample position to 18th sample position for both step sizes. Therefore we get an effective 11 μm Cr width whereas the actual Cr width was 10 μm again giving a spatial resolution of ∼ 1 μm. In both of these measurements for either a narrow or a wide Cr thin film sample, we have achieved a resolution of the

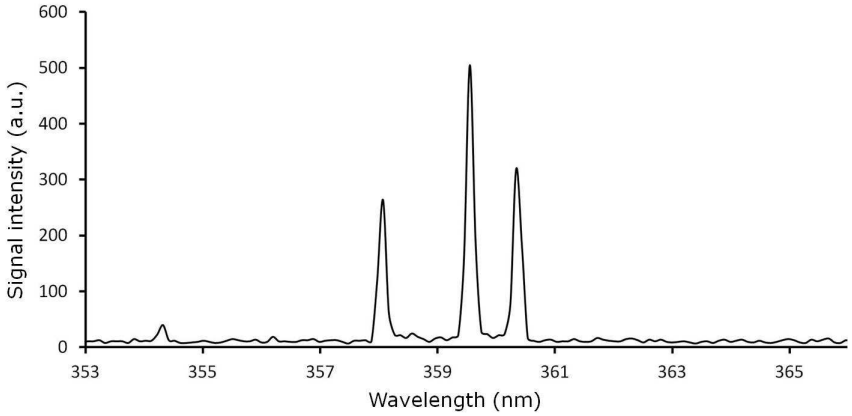

Figure 8.6: Single shot chromium spectra from the target using laser pulse energy of 27 nJ.

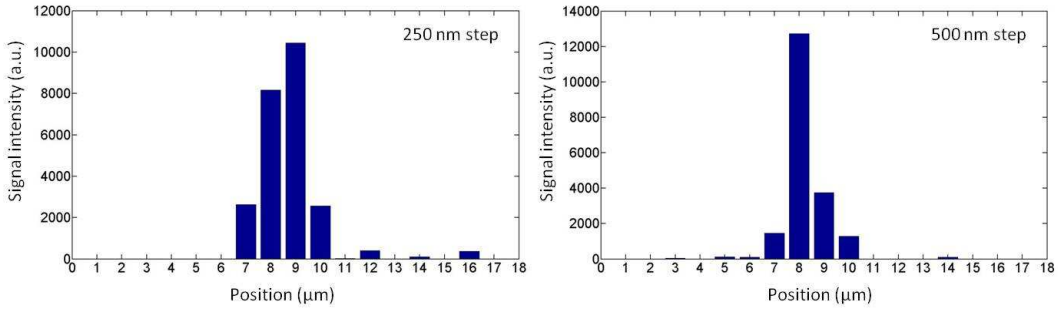

Figure 8.7: Integrated Cr signals from a test pattern with 1.5 μm wide Cr line scanned with different shot to shot distances. The average of 4 shots and 2 shots are taken for 250 nm (left) and 500 nm step size (right) respectively.

order of 1 μm. The results indicate that the real lateral resolution measurement

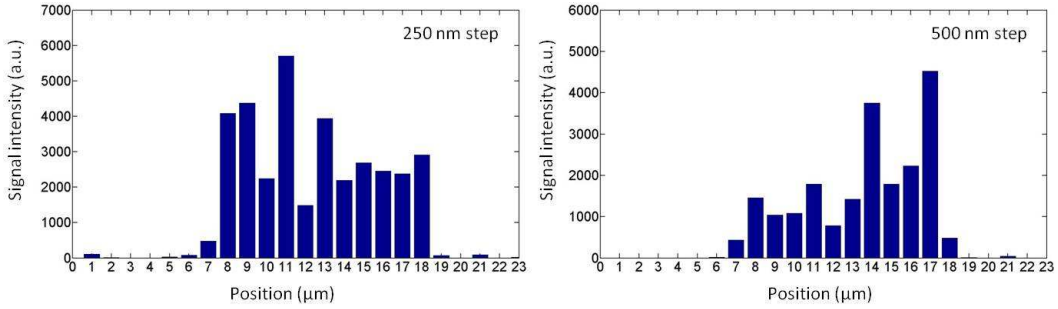

Figure 8.8: Integrated Cr signals from a test pattern with 10 μm wide Cr line scanned with different shot to shot distances. The average of 4 shots and 2 shots are taken for 250 nm (left) and 500 nm step size (right) respectively.

from LIBS spectra is of the order of the spot size. The resolution we get is of the order of a micron which is basically the limit of the measurements by

using an ablation spot size of $\sim$ 1 μm. It is expected that smaller spots at higher intensity may yield higher resolution but will require strict control of the sample position in the axial direction to maintain the sample at focus.

8.4 Conclusions

The effectiveness of using femtosecond 266 nm pulses to carry out high resolution μLIBS has been studied. A long working distance reflective objective was used to produce a micron size ablation spot. The emission signal could be detected from chromium surfaces with 27 nJ incident laser pulse energy. The resolution of our LIBS setup with 266 nm fs pulses was investigated by scanning over thin lines of Cr coated onto a Si substrate. A lateral resolution of the order of $\sim$1 μm was achieved in these measurements. Multishot averaging was used to achieve this resolution in order to reduce the shot to shot variation. To better utilize the advantage of 266 nm femtosecond pulses, future studies should be carried out with smaller diffraction limited spots created by larger numerical aperture focusing objectives along with precisely aligned light collection systems.

Chapter 9

Summary and Conclusions

9.1 Summary and Contributions of the Thesis

The thesis has focused on addressing some important issues in relation to surface microanalysis using LIBS. Two of the main areas of LIBS microanalysis are depth and lateral analysis which have been examined extensively in past. We have extended those areas by presenting new concepts and introducing new approaches in these fields through this thesis. The idea of depth sensitivity which quantifies single shot ablation sensitivity versus depth has been introduced. For femtosecond pulses it has been demonstrated by experiment and clarified by a two temperature model that the plasma formed at the surface layer gives the maximum contribution to the emission spectra, whereas, deeper ablated layers contributed very little to the spectral emission. The depth sensitive emission region was of the order of 3 nm where the actual crater depth was on the order of 100 nm. using multishot ablation buried metallic layers under several microns of silicon semiconductor were detected using LIBS while carrying out precise hole drilling. Drilling rates of 1 μm per shot for Gaussian and 30 nm per shot for flat top beam profiles were achieved. Material removal efficiencies under low and high fluence regimes were calculated. To determine lateral resolution we have prepared thin chromium lines on silicon

wafer and scanned across the lines. The lateral resolution was determined by how accurately we could measure the Cr line-width using LIBS in comparison to the exact thickness of the line. We have achieved ~ 1 μm resolution with our measurements. The applications of very low energy pulses in the nanojoule regime and advantages of short wavelength pulses were demonstrated in this thesis.

In order to explain the physical mechanism behind very low energy laser-matter interactions and related processes, we have explored plasma plume behavior at different background pressures. The angular distribution of the plumes, plume splitting, expansion characteristics of the plume components and plume lengths were analyzed. Plume emission length was introduced in this context. The expansion properties were compared to blast wave and drag models. Plume images near the emission threshold fluences were measured. Chromium thin film ablation characteristics was studied with single shot UV femtosecondand pulses and ablation threshold was calculated. The absorbed single shot ablation threshold fluence was 46 ± 5 mJ/cm^2, whereas a TTM model simulation using similar experimental parameters predicted 31.6 mJ/cm^2 indicating the need for more complete models of the laser plasma interaction.

Within the course of my thesis research work, we have provided a set of results spanning the range from academic to applied LIBS microanalysis research. The specific achievements were:

- The single shot ablation threshold for a 500 nm chromium thin film has been studied using 266 nm, 170 fs laser pulses. Reflectivity of the sample was determined including scattering loss. TTM model was used for comparison. The results were published in Ref. [150].

- The sensitivity depth using single shot LIBS, a new concept in the realm of LIBS depth profiling, has been introduced. A qualitative comparison using TTM model was described. The results were published in Ref.

[155].

- Detailed femtosecond laser plasma plume characteristics have been investigated in the nanojoule ablation regime for the fist time. The spatio-temporal evolution of the plume was explained and compared with analytical models. The results will be useful in application areas of low energy pulsed laser deposition, micromachining, LIBS and production of nanoparticles. The results were published in Ref. [161].

- Femtosecond pulses have been used in the past for either deep hole drilling or LIBS depth profiling. The combination of these two processes has been studied. Theoretical predictions of ablation depths per pulse were compared with experiment. The results were published in Ref. [154].

- Study of lateral resolution using the LIBS technique has been described. A micron order resolution was achieved while scanning UV femtosecond laser pulses across the surface of thin chromium strips on silicon.

9.2 Directions for Future Work

Any new experimental or theoretical study open up avenues to explore new areas and extend the limit of achievement. Laser induced material ablation and the characterization of material constituents using LIBS depends on several experimental parameters such as the laser pulse duration, wavelength, pulse energy, background environment, focusing & collection optics, detector response, target material properties and the spatio-temporal evolution of the plasma. Therefore the scaling of LIBS sensitivity with different parameters will be a complex function. Generally it is expected that better and more consistent coupling to the target species will be obtained with shorter wavelengths where absorption is higher and with shorter, femtosecond duration pulses, where consistent multi photon and tunnel ionization are obtained.

The LIBS work described in the thesis suggests directions for possible future work as outlined below.

9.2.1 Extension of Lateral Resolution

- Lateral resolution increases with decreasing plasma size and therefore, the photon emission. Quantification of the number of photons liberated and the number of photons acquired by the detector will help determine the suitable conditions for best signal collection. One aim would be to collect all the possible photons coming out from the laser induced plasma effectively by adopting very large solid angle light collection conditions.

- An important way to enhance emission is to work under a low pressure environment as shown by Yalcin et al. [46] and others [100, 264, 265]. The plasma stretches out at low pressure and tight depth of focus (DOF) objectives does not image the extended plasma effectively. The plasma may deposit a coating on the objective wall as well. We have worked with an objective with very small working distance. Therefore, the objective

was unable to collect all the possible emissions at low pressures. A long working distance UV objective is desired such as 80X Mitutoyo Plan UV Infinity-Corrected Objective which offers 0.55 nuerical aperture and 10 mm working distance. Another option for plasma characterization using a small DOF objective is to vary the position of the imaging objective that images plasma light onto the slit. Different axial positions between the sample and the focusing objective can be imaged by this procedure although the plasma generation will be same. We have tried this procedure but a detail investigation is needed. The advantage of a large numerical aperture objective is that we can collect the light at large angles with high N.A (f/# $\simeq$ 1) objectives.

- Another way to enhance the emission intensity is to use external magnetic field for magnetic confinement of the plasma [266, 267]. Shen et. al. [267] have shown 6-8 times enhancement for Cu signals using 0.8 T external magnetic field in a transverse direction with respect to plume expansion. Zheng and Jiang [268] have shown that external magnetic field helps cleaning the debris around the ablated spots in femtosecond laser micromachining. Thus external magnetic field could enhance the lateral resolution. We have initiated some experimental work by applying 0.3 T but no distinctive features between with and without magnetic field could be established. Rai et. al. [269] have shown that the value of plasma β (ratio of particle pressure to magnetic pressure) should also be considered while working on LIBS with external magnetic field. An extensive work on plume imaging at different magnetic fields and corresponding LIBS signals would be a good exploration.

9.2.2 Depth Profiling Studies

- Mixing of layers because of melting of different existing materials in a layered sample causes degradation of resolution in LIBS depth profiling. A layered target consisting of a low melting point material integrated with a high melting point material such as tungsten (melting point 3695 K) can be prepared and an investigation could be done to inspect the contribution of layer mixing. TiW can be used in this case which is also known as a diffusion barrier between thin films [270].

- We have seen that a small part of the top layer of the sample produces emission spectra. Study of signal strengths and shot number for a fixed total energy can be done. This would show how, for example, 10 single shots of pulse energy E_1 at one location would compare to one single shot with 10 times E_1 pulse energy.

- Experiments on depth sensitivity for different target materials can be carried out to establish the material dependence on depth sensitivity.

- Experiments for single shot depth sensitivity could be carried out for different pulse lengths up to nanosecond pulses where additional plasma plume heating should occur.

- We have demonstrated deep drill hole along with LIBS to reach a buried layer. A study could be carried out to fill the deep hole channel with metal so that we could make an electrical contact with the buried metallic conductor layer from the semiconductor surface. This would have potential application in the MEMS industry.

9.2.3 LIBS Modeling

- Spatial and temporal evolution of the expanding laser produced plasma can be modeled using established hydrodynamic simulation codes MEDUSA

and MULTI. The electron density, electron velocity, electron temperature, pressure as a function of space and time and space for any experimental setup can be obtained. A 3D version of the MULTI code is now available [271]. These codes can be used to compare experimental observations presented in this thesis specifically with the evolution of micro plasma plume at low pulse energies.

9.2.4 Plasma Reflectivity Measurements

- Absorption of femtosecond UV laser pulses at full interaction intensities with various materials used in this thesis can be carried out to find out the exact energy absorption behavior. An wavelength scaling can also be done in this regard.

9.3 Conclusion

In conclusion, the thesis helps in understanding laser-matter interactions for femtosecond pulses at very low energies and advances LIBS microanalysis research into the micron lateral, nanometer depth, and nanojoule energy range. Many of the results and techniques developed in this work are not just limited to LIBS but also help in understanding other laser assisted material characterization and processing procedures.

Bibliography

[1] D. A. Cremers and L. J. Radziemski, editors. *Handbook of Laser-Induced Breakdown Spectroscopy*. Wiley, 1 edition, 2006.

[2] J. P. Singh and S. N. Thakur, editors. *Laser-Induced Breakdown Spectroscopy*. Elsevier Science, 1 edition, 2007.

[3] A. K. Pathak, R. Kumar, V. K. Singh, R. Agrawal, S. Rai, and A. K. Rai. Assessment of libs for spectrochemical analysis:a review. *Applied Spectroscopy Reviews*, 47:14–40, 2012.

[4] F. J. Fortes, J. Moros, P. Lucena, L. M. Cabalín, and J. J. Laserna. Laser-induced breakdown spectroscopy. *Anal. Chem.*, 85:640–669, 2013.

[5] G. Arca, A. Ciucci, V. Palleschi, S. Rastelli, and E. Tognoni. Trace element analysis in water by the laser induced breakdown spectroscopy technique. *Appl. Spectrosc.*, 51(8):1102–1105, 1997.

[6] N. L. Lanza, R. C. Wiens, S. M. Clegg, A. M. Ollila, S. D. Humphries, H. E. Newsom, J. E. Barefield, and ChemCam Team. Calibrating the chemcam laser-induced breakdown spectroscopy instrument for carbonate minerals on mars. *Appl. Opt.*, 49(13):C211–C217, 2010.

[7] L. J. Radziemski, T. R. Loree, D. A. Cremers, and N. M. Hoffman. Time-resolved laser- induced breakdown spectrometry of aerosols. *Anal. Chem.*, 55:1246–1252, 1983.

[8] I. V. Cravetchi, M. Taschuk, Y. Y. Tsui, and R. Fedosejevs. Scanning microanalysis of al alloys by laser-induced breakdown spectroscopy. *Spectrochimica Acta Part B*, 59:1439–1450, 2004.

[9] Igor V. Cravetchi, Mike T. Taschuk, Ying Y. Tsui, and Robert Fedosejevs. Evaluation of femtosecond libs for spectrochemical microanalysis of aluminium alloys. *Anal. Bioanal. Chem.*, 385:287–294, 2006.

[10] L. M. Cabalín, A. González, V. Lazic, and J. Laserna. Deep ablation and depth profiling by laser-induced breakdown spectroscopy (libs) employing multi-pulse laser excitation: Application to galvanized steel. *Appl. Spectrosc.*, 65(7):797–805, 2011.

[11] Vassilia Zorba, Xianglei Mao, and Richard E. Russo. Optical far- and near-field femtosecond laser ablation of si for nanoscale chemical analysis. *Anal. Bioanal. Chem.*, 396:173–180, 2010.

[12] D. A. Cremers and L. J. Radziemski. Detection of chlorine and fluorine in air by laser-induced breakdown spectrometry. *Anal. Chem.*, 55 (8): 12521256, 1983.

[13] V. Dikshit, F. Y. Yueh, J. P. Singh, D. L. McIntyre, J. C. Jain, and N. Melikechi. Laser induced breakdown spectroscopy: A potential tool for atmospheric carbon dioxide measurement. *Spectrochimica Acta Part B*, 68:65–70, 2012.

[14] S. Nakamura, Y. Ito, K. Sone, H. Hiraga, and K.I. Kaneko. Determination of an iron suspension in water by laser-induced breakdown spectroscopy with two sequential laser pulses. *Anal. Chem.*, 68:2981–2986, 1996.

[15] F. Y. Yueh, R. C. Sharma, J. P. Singh, and H. Zhang. Evaluation of potential of laser induced breakdown spectroscopy for detection of trace element in liquid. *J. Air Waste Manag. Assoc.*, 52:13071315, 2002.

[16] M. Baudelet, J. Yu, M. Bossu, J. Jovelet, Jean-Pierre Wolf, T. Amodeo, E. Fréjafon, and P. Laloi. Discrimination of microbiological samples using femtosecond laser-induced breakdown spectroscopy. *Appl. Phys. Lett.*, 89: 163903(1–3), 2006.

[17] A. Kumar, F. Y. Yueh, J. P. Singh, and S. Burgess. Characterization of malignant tissue cells by laser-induced breakdown spectroscopy. *Appl. Opt.*, 43 (28):53995403, 2004.

[18] V. K. Singh, V. Singh, A. K. Rai, S. N. Thakur, P. K. Rai, and J. P. Singh. Quantitative analysis of gallstones using laser-induced breakdown spectroscopy. *Appl. Opt.*, 47(31):G38–G47, 2008.

[19] R. Agrawal, A. K. Pathak, A.K. Rai, and G. K. Rai. Classification of milk of different origin using libs. *Asian J. Spectros.*, pages 141–146, 2010.

[20] M. T. Taschuk, Y. Y. Tsui, and R. Fedosejevs. Detection and mapping of latent fingerprints by laser induced breakdown spectroscopy. *Appl. Spectrosc.*, 60:1322–1327, 2006.

[21] J. L. Gottfried, F. C. De Lucia, C. A. Munson Jr., and A. W. Miziolek. Standoff detection of chemical and biological threats using laser induced breakdown spectroscopy. *Appl. Spectros.*, 62 (4):353363, 2008.

[22] C. M. Bridge J. Powell K. L. Steele and M. E. Sigman. Forensic comparative glass analysis by laser-induced breakdown spectroscopy. *Spectrochimica Acta Part B*, 62 (12):14191425., 2007.

[23] R. Gaudiuso, M. DellAglio, O. De Pascale, G. S. Senesi, and A. De Giacomo. Laser induced breakdown spectroscopy for elemental analysis in environmental, cultural heritage and space applications: A review of methods and results. *Sensors*, 10:7434–7468, 2010.

[24] J. H. Scholtena, J. M Teulea, V. Zafiropulosb, and R. M. A Heeren. Controlled laser cleaning of painted artworks using accurate beam manipulation and on-line libs-detection. *J. Cultural Heritage*, 1(1):S215–S220, 2000.

[25] H. Balzer, M. Hoehne, R. Noll, and V. Sturm. New approach to online monitoring of the al depth profile of the hot-dip galvanised sheet steel using libs. *Anal. Bioanal. Chem.*, 385:234–239, 2006.

[26] R. Noll, H. Bette, A. Brysch, M. Kraushaar, I. Mönch, L. Peter, and V. Sturm. Laser-induced breakdown spectrometry applications for production control and quality assurance in the steel industry. *Spectrochimica Acta Part B*, 56(6):637–649, 2001.

[27] H. Balzer, M. Hoehne, V. Sturm, and R. Noll. Online coating thickness measurement and depth profiling of zinc coated sheet steel by laser-induced breakdown spectroscopy. *Spectrochimica Acta Part B*, 60:1172–1178, 2005.

[28] K. Meissner, T. Lippert, A. Wokaun, and D. Guenther. Analysis of trace metals in comparison of laser-induced breakdown spectroscopy with la-icp-ms. *Thin Solid Films*, 453-454:316–322, 2004.

[29] G. Abdellatif and H. Imam. A study of the laser plasma parameters at different laser wavelengths. *Spectrochimica Acta Part B*, 57(7):11551165, 2002.

[30] Q. Ma, V. Motto-Ros, F. Laye, J. Yu, W. Lei, X. Bai, L. Zheng, and H. Zeng. Ultraviolet versus infrared: Effects of ablation laser wavelength on the expansion of laser-induced plasma into one-atmosphere argon gas. *J. Appl. Phys.*, 111:053301(1–11), 2012.

[31] R. Fantoni, L. Caneve, F. Colao, L. Fornarini, V. Lazic, and

V. Spizzichino. *Advances in Spectroscopy for Lasers and Sensing*, chapter Laser Induced Breakdown Spectroscopy (LIBS):The process, applications to artwork and environment, pages 229–254. Springer, 2006.

[32] W. Koechner, editor. *Solid-state laser engineering*. Springer, 6 edition, 2006.

[33] E. L. Gurevich and R. Hergenrö. Femtosecond laser- induced breakdown spectroscopy: Physics, applications, and perspectives. *Appl. Spectrosc.*, 61(10):233A242A, 2007.

[34] V. Margetic, A. Pakulev, A. Stockhaus, M. Bolshov, K. Niemax, and R. Hergenröder. A comparison of nanosecond and femtosecond laser-induced plasma spectroscopy of brass samples. *Spectrochimica Acta Part B*, 55:1771–1785, 2000.

[35] J. F. Y. Gravel, F. R. Doucet, P. Bouchard, and M. Sabsabi. Evaluation of a compact high power pulsed fiber laser source for laser-induced breakdown spectroscopy. *J. Anal. At. Spectrom.*, 26:1354–1361, 2011.

[36] J. R. Buckley, F. W. Wise, F. Ö. Ilday, and T. Sosnowski. Femtosecond fiber lasers with pulse energies above 10 nj. *Opt. Lett.*, 30(14):1888–1890, 2005.

[37] Ph. Rohwetter, J. Yu, G. Méjean, K. Stelmaszczyk, E. Salmon, J. Kasparian, J.-P. Wolf, and L. Wöste. Remote libs with ultrashort pulses: characteristics in picosecond and femtosecond regimes. *J. Anal. At. Spectrom.*, 19:437–444, 2004.

[38] A. W. Miziolek, V. Palleschi, and I. Schechter, editors. *Laser-Induced Breakdown Spectroscopy (LIBS) - Fundamentals and Applications*. Cambridge University Press, 2006.

[39] V. Detalle, R. Héon, M. Sabsabi, and L. St-Onge. An evaluation of a commercial chelle spectrometer with intensified charge-coupled device detector for materials analysis by laser-induced plasma spectroscopy. *Spectrochimica Acta Part B*, 56(6):1011–1025, 2001.

[40] C. Haisch, U. Panne, and R. Niessner. Combination of an intensified charge coupled device with an echelle spectrograph for analysis of colloidal material by laserinduced plasma spectroscopy. *Spectrochimica Acta Part B*, 53(12):1657–1667, 1998.

[41] C. D. Tran. Acousto-optic devices: Optical elements for spectroscopy. *Anal. Chem.*, 64(20):971A981A, 1992.

[42] C. C. Hoyt and D. M. Benson. Merging spectroscopy and digital imaging enhances cell research. *Photon. Spectra*, 26(11):92, 1992.

[43] R. A. Myers, A. M. Karger, and D. W. Hahn. Geiger photodiode array for compact, lightweight laser-induced breakdown spectroscopy instrumentation. *Appl. Opt.*, 42(30):6072–6077, 2003.

[44] James R. Janesick, editor. *Scientific Charge-Coupled Devices*. SPIE, 2001.

[45] M. Sabsabi, R. Héon, and L. St-Onge. Critical evaluation of gated ccd detectors for laser-induced breakdown spectroscopy analysis. *Spectrochimica Acta Part B*, 60:1211–1216, 2005.

[46] S. Yalcin, Y. Y. Tsui, and R. Fedosejevs. Pressure dependence of emission intensity in femtosecond laser-induced breakdown spectroscopy. *J. Anal. At. Spectrom.*, 19:1295–1301, 2004.

[47] Y. Iida. Effects of atmosphere on laser vaporization and excitation processes of solid samples. *Spectrochimica Acta Part B*, 45(12):1353–1367, 1990.

[48] L. Peter and R. Noll. Material ablation and plasma state for single and collinear double pulse interacting with iron samples at ambient gas pressures below 1 bar. *Appl. Phys. B*, 86:159–167, 2007.

[49] S. Bashir, N. Farid, K. Mahmood, and M.S. Rafique. Influence of ambient gas and its pressure on the laser-induced breakdown spectroscopy and the surface morphology of laser-ablated cd. *Appl. Phys. A*, 107:203–212, 2012.

[50] J. C. Miller and R.F. Haglund, editors. *Laser Ablation and Desorption*. Elsevier, 30 edition, 1997.

[51] N. Bloembergen. Laser-induced electric breakdown in solids. *IEEE J. Quantum Electron.*, 10(3):376–386, 1974.

[52] T. Hertel, E. Knoesel, M. Wolf, and G. Ertl. Ultrafast electron dynamics at cu(111): Response of an electron gas to optical excitation. *Phys. Rev. Lett.*, 76(3):535–538, 1996.

[53] W. S. Farm, R. Storz, H. W. K. Tom, and J. Bokor. Electron thermalization in gold. *Phys. Rev. B*, 46(20):13592–13595, 1992.

[54] R. Stoian, D. Ashkenasi, A. Rosenfeld, and E. E. B. Campbell. Coulomb explosion in ultrashort pulsed laser ablation of al_2o_3. *Phys. Rev. B*, 62(19):13167–13173, 2000.

[55] L. Poth and Jr. A. W. Castleman. Molecular dynamics simulation of coulomb explosion processes. *J. Phys. Chem. A*, 102(23):4075–4081, 1998.

[56] P. Lorazo, L. J. Lewis, and M. Meunier. Short-pulse laser ablation of solids: From phase explosion to fragmentation. *Phys. Rev. Lett.*, 91(22): 225502(1–4), 2003.

[57] J. H. Yoo, O. V. Borisov, X. Mao, and R. E. Russo. Existence of phase explosion during laser ablation and its effects on inductively coupled plasma-mass spectroscopy. *Anal. Chem.*, 73:2288–2293, 2001.

[58] J. F. Kephart, R. P. Godwin, and G. H. McCall. Bremsstrahlung emission from laser-produced plasmas. *Appl. Phys. Lett.*, 25:108–109, 1974.

[59] Hans R. Griem, editor. *Spectral Line Broadening by Plasmas*. Academic Press, 39 edition, 1974.

[60] H. R. Griem. Validity of local thermal equilibrium in plasma spectroscopy. *Phys. Rev.*, 131(3):1170–1176, 1963.

[61] M. E. Fermann, A. Galvanauskas, and G. Sucha, editors. *Ultrafast Lasers: Technology and Applications*. M. Dekker, 2005.

[62] S. Nolte, B. N. Chichkov, H. Welling, Y. Shani, K. Lieberman, and H. Terkel. Nanostructuring with spatially localized femtosecond laser pulses. *Opt. Lett.*, 24(13):914–916, 1999.

[63] A. P. Joglekar, H. Liu, G.J. Spooner, E. Meyhöfer, G. Mourou, and A. J. Hunt. A study of the deterministic character of optical damage by femtosecond laser pulses and applications to nanomachining. *Appl. Phys. B*, 77(1):25–30, 2003.

[64] A. Chimmalgi, C. P. Grigoropoulos, and K. Komvopoulos. Surface nanostructuring by nano-/femtosecond laser-assisted scanning force microscopy. *J. Appl. Phys.*, 97:104319(1–12), 2005.

[65] R. Osellame, G. Cerullo, and R. Ramponi, editors. *Femtosecond Laser Micromachining*. Springer-Verlag, 2012.

[66] R. Schaeffer, editor. *Fundamentals of Laser Micromachining*. CRC Press, 2012.

[67] S. Singh, M. Argument, Y. Y. Tsui, and R. Fedosejevs. Effect of ambient air pressure on debris redeposition during laser ablation of glass. *J. Appl. Phys.*, 98:113520(1–7), 2005.

[68] Michael M. Mielke, Timothy Booth, Michael Greenberg, David M. Gaudiosi, Carolyn Martinez, Steven P. Sapers, Robert Cline, and Ramanujapuram. A. Srinivas. Applications of ultrafast lasers in microfabrication. *Journal of Laser Micro/Nanoengineering*, 8(2):115–123, 2013.

[69] K. Saito, K. Takatani, T. Sakka, and Y. H. Ogata. Observation of the light emitting region produced by pulsed laser irradiation to a solidliquid interface. *Appl. Surf. Sci.*, 197-198:56–60, 2002.

[70] M. E. Shaheen, J. E. Gagnon, and B. J. Fryer. Femtosecond laser ablation of brass in air and liquid media. *J. Appl. Phys.*, 113:213106(1–5), 2013.

[71] L. S. Jiao, E.Y.K. Ng, and H.Y. Zheng. Refining femtosecond laser induced periodical surface structures with liquid assist. *Appl. Surf. Sci.*, 264:52–55, 2013.

[72] D. N. Patel, Ravi Pratap Singh, and Raj K. Thareja. Craters and nanostructures with laser ablation of metal/metalalloy in air and liquid. *Appl. Surf. Sci.*, 288:550–557, 2014.

[73] Hong-Bo Sun and Satoshi Kawata. Two-photon photopolymerization and 3d lithographic microfabrication. *Adv. Polym. Sci.*, 170:169–273, 2004.

[74] Y. Liao, J. Song, En Li, Y. Luo, Y. Shen, D. Chen, Y. Cheng, Z. Xu, K. Sugioka, and K. Midorikawa. Rapid prototyping of three-dimensional microfluidic mixers in glass by femtosecond laser direct writing. *Lab. Chip.*, 12:746–749, 2012.

[75] K. Chen and Y. L. Yao. Process optimisation in pulsed laser micromachining with applications in medical device manufacturing. *Int. J. Adv. Manuf. Technol.*, 16:243–249, 2000.

[76] N. Shen, D. Datta, C. B. Schaffer, P. LeDuc, D. E. Ingber, and E. Mazur.

Ablation of cytoskeletal filaments and mitochondria in cells using a femtosecond laser nanoscissor. *Mech. Chem. Biosyst.*, 2:17–25, 2005.

[77] M. Kamata, M. Obara, R. R. Gattass, L. R. Cerami, and E. Mazur. Optical vibration sensor fabricated by femtosecond laser micromachining. *Appl. Phys. Lett.*, 87(5):051106(1–3), 2005.

[78] Ik-Bu Sohn, Y. Kim, and Young-Chul Noh. Microstructuring of optical fibers using a femtosecond laser. *J. Opt. Soc. Korea*, 13(1):33–36, 2009.

[79] Wataru Watanabe, Takayuki Tamaki, and Kazuyoshi Itoh. *Femtosecond Laser Micromachining*, chapter Ultrashort Laser Welding and Joining, pages 467–477. Springer-Verlag, 2012.

[80] R. Haight, D. Hayden, P. Longo, T. Neary, and A. Wagner. Mars: Femtosecond laser mask advanced repair system in manufacturing. *J. Vac. Sci. Technol., B*, 17:3137–3143, 1999.

[81] Pandora Psyllaki and Roland Oltra. Preliminary study on the laser cleaning of stainless steels after high temperature oxidation. *Mater. Sci. Eng. A*, 282:145–152, 2000.

[82] F. Morin, Y. Zaouter, C. Hoenninger, E. Mottay, B. Dunne, R. De Almeida, and J. Aguerre. Thin film cigs solar cell scribing with a femtosecond high energy and high average power fiber amplifier. In *Advanced Solid-State Lasers Congress, G. Huber and P. Moulton, eds.*, 2013.

[83] M. J. Navas and A. M. Jimënez. Thermal lens spectrometry as analytical tool. *Crit. Rev. Anal. Chem.*, 2:77–88, 2003.

[84] G. C. Turk, J. C. Travis, and J. R. DeVoe. Laser enhanced ionization spectrometry in analytical flames. *Anal. Chem.*, 51(12):1890–1896, 1979.

[85] Y. H. Wong, R. L. Thomas, and G. F. Hawkins. Surface and subsurface structure of solids by laser photoacoustic spectroscopy. *Appl. Phys. Lett.*, 32:538–539, 1978.

[86] R. E. Russo, X. Mao, J. J. Gonzalez, and S. S. Mao. Femtosecond laser ablation icp-ms. *J. Anal. At. Spectrom.*, 17:1072–1075, 2002.

[87] P. J. Hendra and P. M. Stratton. Laser-raman spectroscopy. *Chem. Rev., 1969, 69 (3),*, 69(3):325–344, 1969.

[88] J. L. Kinsey. Laser-induced fluoroscence. *Ann. Rev. Phys. Chern.*, 28: 349–372, 1977.

[89] E. D. Hinkley. High resolution infrared spectroscopy with a tunable diode laser. *Appl Phys Lett.*, 16(9):351–354, 1970.

[90] M. T. Taschuk. PhD thesis, University of Alberta, 2007.

[91] G. L. Long and J. D. Winefordner. Limit of detection: a closer look at the iupac definition. *Anal. Chem.*, 55:712–724, 1983.

[92] C. Geertsen, J.L. Lacour, P. Mauchien, and L. Pierrard. Evaluation of laser ablation optical emission spectrometry for microanalysis in aluminium samples. *Spectrochimica Acta Part B*, 51:1403–1416, 1996.

[93] J. O. Cáceres, J. T. López, H. H. Telle, and A. G. Ure na. Quantitative analysis of trace metal ions in ice using laser-induced breakdown spectroscopy. *Spectrochimica Acta Part B*, 56:831–838, 2001.

[94] G. W. Rieger, M. Taschuk, Y. Y. Tsui, and R. Fedosejevs. Laser-induced breakdown spectroscopy for microanalysis using submillijoule uv laser pulses. *Appl. Spectros.*, 56(6):689–698, 2002.

[95] Y. Talmi, H. P. Seiper, and L. M. Bankenberg. Laser microprobe elemental determinations with an optical multichannel detector system. *Anal. Chimica Acta*, 127:71–85, 1981.

[96] C. J. Lorenzen, C. Carlhoff, U. Hahn, and M. Jogwich. Applications of laser-induced emission spectral analysis for industrial process and quality control. *J. Anal. At. Spectrom.*, 7(6):1029–1035, 1992.

[97] D. R. Anderson, C. W. McLeod, T. English, and A. T. Smith. Depth profile studies using laser-induced plasma emission spectrometry. *Appl. Spectrosc.*, 49(6):691–701, 1995.

[98] J. M. Vadillo and J. J. Laserna. Depth-resolved analysis of multilayered samples by laser-induced breakdown spectrometry. *J. Anal. At. Spectrom.*, 12:859–862, 1997.

[99] J. M. Vadillo, C. C. García, S. Palanco, and J. J. Laserna. Nanometric range depth-resolved analysis of coated-steels using laser-induced breakdown spectrometry with a 308 nm collimated beam. *J. Anal. At. Spectrom.*, 13:793–797, 1998.

[100] J. M. Vadillo, J. M. Fernández Romero, C. Rodríguez, and J. J. Laserna. Depth-resolved analysis by laser-induced breakdown spectrometry at reduced pressure. *Surf. Interface Anal.*, 26:995–1000, 1998.

[101] M. Milán, P. Lucena, L. M. Cabalín, and J. J. Laserna. Depth profiling of phosphorus in photonic-grade silicon using laser-induced breakdown spectrometry. *Appl. Spectros.*, 52(3):444–448, 1998.

[102] C. C. García, M. Corral, J. M. Vadillo, and J. J. Laserna. Angle-resolved laser-induced breakdown spectrometry for depth profling of coated materials. *Appl. Spectrosc.*, 54(7):1027–1031, 2000.

[103] M. P. Mateo, J. M. Vadillo, and J. J. Laserna. Irradiance-dependent depth profiling of layered materials using laser-induced plasma spectrometry. *J. Anal. At. Spectrom.*, 16:1317–1321, 2001.

[104] H. Häkkänen, J. Houni, S. Kaski, and J. E. I. Korppi-Tommola. Analysis of paper by laser-induced plasma spectroscopy. *Spectrochimica Acta Part B*, 56:737–742, 2001.

[105] V. Margetic, M. Bolshov, A. Stockhaus, K. Niemax, and R. Hergenröder. Depth profiling of multi-layer samples using femtosecond laser ablation. *J. Anal. At. Spectrom.*, 16:616–621, 2001.

[106] H. Von Bergmann M. A. Harith A. H. Galmed, A. K. Kassem. A study of using femtosecond libs in analyzing metallic thin filmsemiconductor interface. *Appl Phys B*, 102:197204, 2011.

[107] A. De Bonisa, B. De Filippo, A. Galasso, A. Santagata, A. Smaldone, and R. Teghila. Comparison of the performances of nanosecond and femtosecondlaser induced breakdown spectroscopy for depth profiling of anartificially corroded bronze. *Appl.Surf. Sci.*, 302:275–279, 2014.

[108] V. Zorba, J. Syzdek, X. Mao, R. E. Russo, and R. Kostecki. Ultrafast laser induced breakdown spectroscopy of electrode/electrolyte interfaces. *Appl. Phys. Lett.*, 100:234101(1–5), 2012.

[109] A. Nevin, G. Spoto, and D. Anglos. Laser spectroscopies for elemental and molecular analysis in art and archaeology. *Appl. Phys. A*, 106(2): 339–361, 2012.

[110] P. Pouli, K. Melessanaki, A. Giakoumaki, V. Argyropoulos, and D. Anglos. Measuring the thickness of protective coatings on historic metal objects using nanosecond and femtosecond laser induced breakdown spec-

troscopy depth profiling. *Spectrochimica Acta Part B*, 60:1163–1171, 2005.

[111] E. A. Kaszewska, M. Sylwestrzak, J. Marczak, W. Skrzeczanowski, M. Iwanicka, E. Szmit-Naud, D. Anglos, and P. Targowski. Depth-resolved multilayer pigment identification in paintings: Combined use of laser-induced breakdown spectroscopy (libs) and optical coherence tomography (oct). *Appl. Spectrosc.*, 67(8):960–972, 2013.

[112] D. G. Papazoglou, V. Papadakis, and D. Anglos. In situ interferometric depth and topography monitoring in libs elemental profiling of multi-layer structures. *J. Anal. At. Spectrom.*, 19:483–488, 2004.

[113] A. Giakoumaki, I. Osticioli, and D. Anglos. Spectroscopic analysis using a hybrid libs-raman system. *Appl. Phys. A*, 83:537–541, 2006.

[114] L. Caneve, A. Diamanti, F. Grimaldi, G. Palleschi, V. Spizzichino, and F. Valentini. Analysis of fresco by laser induced breakdown spectroscopy. *Spectrochimica Acta Part B*, 65:702–706, 2010.

[115] A. Erdema, A. ilingiro glu, A. Giakoumaki, M. Castanys, E. Kartsonaki, C. Fotakis, and D. Anglos. Characterization of iron age pottery from eastern turkey by laser- induced breakdown spectroscopy (libs). *J. Archaeol. Sci.*, 35:2486–2494, 2008.

[116] M. Abdelhamid, S. Grassini, E. Angelini, G. M. Ingo, and M. A. Harith. Depth profiling of coated metallic artifacts adopting laser-induced breakdown spectrometry. *Spectrochimica Acta Part B*, 65:695–701, 2010.

[117] A. Staicu, I. Apostol, A. Pascu, I. Iordache, V. Damian, and M. L. Pascu. Laser induced breakdown spectroscopy stratigraphic characterization of multilayered painted surfaces. *Spectrochimica Acta Part B*, 74-75:151–155, 2012.

[118] Ann M. Ollila et al. Trace element geochemistry (li, ba, sr, and rb) using curiositys chemcam: Early results for gale crater from bradbury landing site to rocknest. *J. Geo. Res.: Planets*, 119:255–285, 2014.

[119] A. A. Bolshakov, J. H. Yoo, J. J. Gonzalez, C. Liu, and R. E. Russo. Direct real-time determination of compositional profiles in structured materials using laser ablation instruments: Libs and la-icp-ms. *Applied Industrial Optics: Spectroscopy, Imaging and Metrology (Proceedings)*, pages 1–3, 2012.

[120] A. E. Siegman, editor. *Lasers*. Technology & Engineering, 1986.

[121] T. Kim, C. T. Lin, and Y. Yoon. Compositional mapping by laser-induced breakdown spectroscopy. *J. Phys. Chem. B*, 102:4284–4287, 1998.

[122] J. M. Vadillo, S. Palanco, M. D. Romero, and J. J. Laserna. Applications of laser-induced breakdown spectrometry (libs) in surface analysis. *Fresenius J. Anal. Chem.*, 255:909–912, 1996.

[123] D. Romero and J. J. Laserna. Surface and tomographic distribution of carbon impurities in photonic-grade silicon using laser-induced breakdown spectrometry. *J. Anal. At. Spectrom.*, 13:557–560, 1998.

[124] P. Lucena and J. J. Laserna. Three-dimensional distribution analysis of platinum, palladium and rhodium in auto catalytic converters using imaging-mode laser-induced breakdown spectrometry. *Spectrochimica Acta Part B*, 56:177–185, 2001.

[125] P. Lucena, J. M. Vadillo, and J. J. Laserna. Spatial distribution of catalytically active elements and deactivants in dieselengine automobile converters by laser-induced plasma spectroscopy. *J. Anal. At. Spectrom.*, 17: 548–551, 2002.

[126] M. Mateo, L. Cabalín, J. Baena, and J. Laserna. Surface interaction and chemical imaging in plasma spectrometry induced with a line-focused laser beam. *Spectrochimica Acta Part B*, 57:601–608, 2002.

[127] I. V. Cravetchi, M. Taschuk, G. W. Rieger, Y. Y. Tsui, and R. Fedosejevs. Spectrochemical microanalysis of aluminum alloys by laser-induced breakdown spectroscopy: identification of precipitates. *Appl. Opt.*, 42(30):6138–6147, 2003.

[128] H. Bette and R. Noll. High speed laser-induced breakdown spectrometry for scanning microanalysis. *J. Phys. D: Appl. Phys.*, 37:1281–1288, 2004.

[129] V. Pi non, M .P. Mateo, and G. Nicolas. Laser-induced breakdown spectroscopy for chemical mapping of material. *Appl. Spectrosc. Rev.*, 48: 357–383, 2013.

[130] A. Assion, M. Wollenhaupt, L. Haag, F. Mayorov, C. Sarpe-Tudoran, M. Winter, U. Kutschera, and T. Baumert. Femtosecond laser-induced-breakdown spectrometry for ca^{2+} analysis of biological samples with high spatial resolution. *Appl. Phys. B*, 77:391–397, 2003.

[131] D. Menut, P. Fichet, J. L. Lacour, A. Rivoallan, and P. Mauchien. Micro-laser-induced breakdown spectroscopy technique: a powerful method for performing quantitative surface mapping on conductive and nonconductive samples. *Appl. Opt.*, 42(30):6063–6071, 2003.

[132] W. Wessel, A. Brueckner-Foit, J. Mildner, L. Englert, L. Haag, A. Horn, M. Wollenhaupt, and T. Baumert. Use of femtosecond laser-induced breakdown spectroscopy (fs-libs) for micro-crack analysis on the surface. *Eng. Fract. Mech.*, 77:1874–1883, 2010.

[133] Yuan Lu, Vassilia Zorba, Xianglei Mao, Ronger Zheng, and Richard E. Russo. Uv fsns double-pulse laser induced breakdown spectroscopy for

high spatial resolution chemical analysis. *J. Anal. At. Spectrom.*, 28: 743–748, 2013.

[134] Jutta Mildner, Cristian Sarpe, Nadine Götte, Matthias Wollenhaupt, and Thomas Baumert. Emission signal enhancement of laser ablation of metals (aluminumand titanium) by time delayed femtosecond double pulses fromfemtoseconds to nanoseconds. *Appl. Surf. Sci.*, 302:291–298, 2014.

[135] D. Kossakovski and J. L. Beauchamp. Topographical and chemical microanalysis of surfaces with a scanning probe microscope and laser-induced breakdown spectroscopy. *Anal. Chem.*, 72:4731–4737, 2000.

[136] David J Hwang, Hojeong Jeon, Costas P Grigoropoulos, Jong Yoo, and Richard E Russo. Femtosecond laser ablation induced plasma characteristics from submicron craters in thin metal film. *Appl. Phys. Lett.*, 91: 251118(1–3), 2007.

[137] V. Zorba, X. Mao, and R. E. Russo. Ultrafast laser induced breakdown spectroscopy for high spatial resolution chemical analysis. *Spectrochimica Acta Part B*, 66:189–192, 2011.

[138] S. M. Angel, D. N. Stratis, K. L. Eland, T. Lai, M. A. Berg, and D. M. Gold. Libs using dual- and ultra-short laser pulses. *J. Anal. Chem.*, 369: 320–327, 2001.

[139] V. N. Rai, F. Y. Yueh, and J. P. Singh. Time-dependent single and double pulse laser-induced breakdown spectroscopy of chromium in liquid. *Appl. Opt.*, 47(31):G21–G29, 2008.

[140] S. L. Lui, Y. Godwal, M. T. Taschuk, Y. Y. Tsui, and R. Fedosejevs. Detection of lead in water using laser-induced breakdown spectroscopy and laser-induced fluorescence. *Anal. Chem.*, 80:1995–2000, 2008.

[141] A. Bogaerts, Z. Chen, and D. Autrique. Double pulse laser ablation and laser induced breakdown spectroscopy: A modeling investigation. *Spectrochimica Acta Part B*, 63(7):746–754, 2008.

[142] G. Cristoforetti, S. Legnaioli, V. Palleschi, A. Salvetti, and E. Tognoni. Effect of target composition on the emission enhancement observed in double-pulse laser-induced breakdown spectroscopy. *Spectrochimica Acta Part B*, 63(2):312–323, 2008.

[143] R. C. Wiens, S. K. Sharma, J. Thompson, A. Misra, and P. G. Lucey. Joint analyses by laser-induced breakdown spectroscopy (libs) and raman spectroscopy at stand-off distances. *Spectrochimica Acta Part A*, 61(10): 2324–2334, 2005.

[144] P. Yaroshchyk, R. J. S. Morrison, D. Body, and B. L. Chadwick. Quantitative determination of wear metals in engine oils using libs: The use of paper substrates and a comparison between single- and double-pulse libs. *Spectrochimica Acta Part B*, 60(11):1482–1485, 2005.

[145] N. E. Schmidt and S. R. Goode. Analysis of aqueous solutions by laser-induced breakdown spectroscopy of ion exchange membranes. *Appl. Spectros.*, 56(3):370–374, 2002.

[146] Z. Chen, H. Li, F. Zhao, and R. Li. Fast and sensitive trace metal analysis in aqueous solutions by laser-induced breakdown spectroscopy using wood slice substrates. *Spectrochimica Acta Part B*, 63:64–68, 2008.

[147] Z. Chen, H. Li, F. Zhao, and R. Li. Ultra-sensitive trace metal analysis of water by laser-induced breakdown spectroscopy after electrical-deposition of the analytes on an aluminium surface. *J. Anal. At. Spectrom.*, 23:871–875, 2008.

[148] D. W. Hahn and N. Omenetto. Laser-induced breakdown spectroscopy

(libs), part ii: Review of instrumental and methodological approaches to material analysis and applications to different fields. *Appl. Spectros.*, 66(4):347–419, 2012.

[149] C. G. Sansonetti, M. L. Salit, and J. Reader. Wavelengths of spectral lines in mercury pencil lamps. *Appl. Opt.*, 35(1):74–77, 1996.

[150] S. P. Banerjee and R. Fedosejevs. Single shot ablation threshold of chromium using uv femtosecond laser pulses. *Appl. Phys. A*, DOI: 10.1007/s00339-014-8577-y, 2014.

[151] J. Békési, J.-H. Klein-Wiele, and P. Simon. Efficient submicron processing of metals with femtosecond uv pulses. *Appl. Phys. A*, 76:355–357, 2003.

[152] J. A. Sue and T.P. Chang. Friction and wear behavior of titanium nitride, zirconium nitride and chromium nitride coatings at elevated temperatures. *Surf. Coat. Tech.*, 76-77:61–69, 1995.

[153] Viviana Mulloni and Fondazione B. Kessler. *"Chromium in MEMS Technology" in book "Chromium: Environmental, Medical and Materials Studies"*. Nova Publishers, 2011.

[154] S. P. Banerjee, Z. Chen, I. Utkin, and R. Fedosejevs. Detection of buried layers in silicon devices using libs during hole drilling with femtosecond laser pulses. *Appl. Phys. A*, 111:791–798, 2013.

[155] S.P. Banerjee and R. Fedosejevs. Single shot depth sensitivity using femtosecond laser induced breakdown spectroscopy. *Spectrochimica Acta Part B*, 92:34–41, 2014.

[156] J. H. Weaver and H. P. R. Frederikse. *CRC Handbook of Chemistry and Physics*, chapter Optical Properties of selected elements, pages 12–135. CRC Press, Boca Raton, Florida, 2004.

[157] Jaegu Kim and Suckjoo Na. Metal thin film ablation with femtosecond pulsed laser. *Opt. Laser Tech.*, 39:1443–1448, 2007.

[158] S. Preuss, A. Demchuk, and M. Stuke. Sub-picosecond uv laser ablation of metals. *Appl. Phys. A*, 61:33–37, 1995.

[159] S. Preuss, E. Matthias, and M. Stuke. Sub-picosecond uv-laser ablation of ni films: Strong fluence reduction and thickness-independent removal. *Appl. Phys. A*, 59:79–82, 1994.

[160] S. Preuss, M. Späth, Y. Zhang, and M. Stuke. Time resolved dynamics of subpicosecond laser ablation. *Appl. Phys. Lett.*, 62:3049–3051, 1993.

[161] S. P. Banerjee, Zhijiang Chen, and R. Fedosejevs. Femtosecond laser plasma plume characteristics in the nanojoule ablation regime. *J. Appl. Phys.*, 113:183101(1–10), 2013.

[162] S. E. Kirkwood, A. C. Van Popta, Y. Y. Tsui, and R. Fedosejevs. Single and multiple shot near-infrared femtosecond laser pulse ablation thresholds of copper. *Appl. Phys. A*, 81:729–735, 2005.

[163] Jeppe Byskov-Nielsen, Juha-Matti Savolainen, Martin Snogdahl Christensen, and Peter Balling. Ultra-short pulse laser ablation of metals: threshold fluence, incubation coefficient and ablation rates. *Appl Phys A*, 101:97–101, 2010.

[164] J. M. Liu. Simple technique for measurements of pulsed gaussian-beam spot sizes. *Opt. Lett.*, 7(5):196–198, 1982.

[165] A. Rosenfeld and E. E. B. Campbell. Picosecond uv-laser ablation of au and ni films. *Appl. Surf. Sci.*, 96-98:439–442, 1996.

[166] J. Ihlemann, A. Scholl, H. Schmidt, and B. Woltf-Rottke. *Appl. Phys. A*, 60:411–417, 1995.

[167] L.M. Cabalín and J.J. Laserna. Experimental determination of laser induced breakdown thresholds of metals under nanosecond q-switched laser operation. *Spectrochimica Acta Part B*, 53:723–730, 1998.

[168] E. D. Palik, editor. *Handbook of Optical Constants of Solids*. Academic Press, 1 edition, 1985.

[169] David R. Lide, editor. *CRC Handbook of Chemistry and Physics*. CRC Press, 87 edition, 2006.

[170] Yau-Ming Lai and Nai-Ho Cheung. Pulsed laser induced damage threshold studies of thin aluminum films on quartz: Simultaneous monitoring of optical and acoustic signals. *Rev. Sci. Inst.*, 64:1606–1610, 1993.

[171] S. Petzoldt, J. Reif, and E. Matthias. Laser plasma threshold of metals. *Appl. Surf. Sci.*, 96-98:199–204, 1996.

[172] A. Lisfi, M. Guyot, R. Krishnan, and V. Cagan. Measurement and calculation of the fe_2o_3 ablation depth. *Appl. Surf. Sci.*, 96-98:66–70, 1996.

[173] J. Jandeleit, G. Urbasch, H. D. Hoffmann, H.-G. Treusch, and E.W. Kreutz. Picosecond laser ablation of thin copper films. *Appl. Phys. A*, 63:117–121, 1996.

[174] Yong Jee, Michael F. Becker, and Rodger M. Walser. Laser-induced damage on single-crystal metal surfaces. *J. Opt. Soc. Am. B*, 5(3):648–659, 1988.

[175] C. Momma, S. Nolte, B. N. Chichkov, F. V. Alvensleben, and A. Tünnermann. Precise laser ablation with ultrashort pulses. *Appl. Surf. Sci.*, 109/110:15–19, 1997.

[176] S. I. Anisimov, B. L. Kapeliovich, and T. L. Perel'man. Electron emission from metal surfaces exposed to ultrashort laser pulses. *Sov. Phys.-JETP*, 39(2):375–377, 1974.

[177] P. B. Corkum, F. Brunel, N. K. Sherman, and T. Srinivasan-Rao. Thermal response of metals to ultrashort-pulse laser excitation. *Phys. Rev. Lett.*, 61(25):2886–2889, 1988.

[178] V. Schmidt, W. Husinsky, and G. Betz. Ultrashort laser ablation of metals: pumpprobe experiments, the role of ballistic electrons and the two-temperature model. *Appl. Surf. Sci.*, 197-198:145–155, 2002.

[179] S. E. Kirkwood. PhD thesis, University of Alberta, 2007.

[180] C. Kittel, editor. *Introduction to Solid State Physics*. John Wiley & Sons, 7 edition, 1996.

[181] Mischa Bonn, Daniel N. Denzler, Stephan Funk, Martin Wolf, S.-Svante Wellershoff, and Julius Hohlfeld. Ultrafast electron dynamics at metal surfaces: Competition between electron-phonon coupling and hot-electron transport. *Phys. Rev. B*, 61(2):1101–1105, 2000.

[182] Sergei I Anisimov and Baerbel Rethfeld. Theory of ultrashort laser pulse interaction with a metal. In *Nonresonant Laser-Matter Interaction*, pages 192–203. International Society for Optics and Photonics, 1997.

[183] C. Schäfer, H. M. Urbassek, and L. V. Zhigilei. Metal ablation by picosecond laser pulses: A hybrid simulation. *Phys. Rev. B*, 66:115404(1–8), 2002.

[184] R. Fedosejevs, R. Ottmann, R. Sigel, G. Kühnle, S. Szatmári, and F. P. Schäfer. Absorption of subpicosecond ultraviolet laser pulses in high-density plasma. *Appl. Phys. B*, 50:79–99, 1990.

[185] S. E. Kirkwood, Y. Y. Tsui, R. Fedosejevs, A. V. Brantov, and V. Yu. Bychenkov. Experimental and theoretical study of absorption of femtosecond laser pulses in interaction with solid copper targets. *Phys. Rev. B*, 79:144120(1–7), 2009.

[186] M. T. Taschuk, S. E. Kirkwood, Y. Y. Tsui, and R. Fedosejevs. Quantitative emission from femtosecond microplasmas for laserinduced breakdown spectroscopy. *Journal of Physics: Conference Series*, 59:328–332, 2007.

[187] K. Novotný, T. Vaculovič, M. Galiová, V. Otruba, V. Kanický, J. Kaiser, M. Liška, O. Samek, R. Malina, and K. Páleníková. The use of zinc and iron emission lines in the depth profile analysis of zinc-coated steel. *Appl. Surf. Sci.*, 253:3834–3842, 2007.

[188] Brian T Fisher, Howard A Johnsen, Steven G Buckley, and David W Hahn. Temporal gating for the optimization of laser-induced breakdown spectroscopy detection and analysis of toxic metals. *Appl. Spectrosc.*, 55 (10):1312–1319, 2001.

[189] M. T. Taschuk, Y. Godwal, Y. Y. Tsui, R. Fedosejevs, M. Tripathy, and B. Kearton. Views and criticism : Absolute characterization of laser-induced breakdown spectroscopy detection systems. *Spectrochimica Acta Part B*, 63:525–535, 2008.

[190] H. R. B. Orlande, M. N. Özisik, and D. Y. Tzou. Inverse analysis for estimating the electronphonon coupling factor in thin metal films. *J. Appl. Phys.*, 78:1843–1849, 1995.

[191] E. Millon, O. Albert, J. C. Loulergue, J. Etchepare, D. Hulin, W. Seiler, and J. Perrière. Growth of heteroepitaxial zno thin films by femtosecond pulsed-laser deposition. *J. Appl. Phys.*, 88:6937–6939, 2000.

[192] A. A. Melaibari and Pal Molian. Pulsed laser deposition to synthesize the bridge structure of artificial nacre: Comparison of nano- and femtosecond lasers. *J. Appl. Phys.*, 112:104303(1–10), 2012.

[193] R. R. Gattass and E. Mazur. Femtosecond laser micromachining in transparent materials. *Nat. Photon.*, 2:219–225, 2008.

[194] G. D. Valle, R. Osellame, and P. Laporta. Micromachining of photonic devices by femtosecond laser pulses. *J. Opt. A: Pure Appl. Opt.*, 11: 013001(1–18), 2009.

[195] S. E. Kirkwood, M. T. Taschuk, Y. Y. Tsui, and R. Fedosejevs. Nanomilling surfaces using near-threshold femtosecond laser pulses. *Journal of Physics: Conference Series*, 59:591–594, 2007.

[196] R. Fedosejsvs, Y. Tsui, Z. Chen, and S. Banerjee. *Nano-fabrication Techniques and Principles*, chapter Laser Nanopatterning, pages 301–319. Springer-Verlag/Wien, 1 edition, 2012.

[197] B. Tan and K. Venkatakrishnan. Synthesis of fibrous nanoparticle aggregates by femtosecond laser ablation in air. *Opt. Express*, 17(2):1064–1069, 2009.

[198] D. W. Hahn and N. Omenetto. Laser-induced breakdown spectroscopy (libs), part i: Review of basic diagnostics and plasma particle interactions: Still-challenging issues within the analytical plasma community. *Appl. Spectrosc.*, 64(12):335–366, 2010.

[199] K. Kagawa and S. Yokoi. Application of the N_2 laser to laser microprobe spectrochemical analysis*. *Spectrochim. Acta. pt. B*, 37(9):789–795, 1982.

[200] P. E. Dyer and J. Sidhu. Spectroscopic and fast photographic studies of excimer laser polymer ablation. *J. Appl. Phys.*, 64(9):4657–4663, 1988.

[201] D. B. Geohegan and A. A. Puretzky. Dynamics of laser ablation plume penetration through low pressure background gases. *Appl. Phys. Lett.*, 67(2):197–199, 1995.

[202] S. S. Harilal, C. V. Bindhu, M. S. Tillack, F. Najmabadi, and A. C. Gaeris. Internal structure and expansion dynamics of laser ablation plumes into ambient gases. *J. Appl. Phys.*, 93(5):2380–2388, 2003.

[203] S. Mahmood, R. S. Rawat, M. Zakaullah, J. J. Lin, S. V. Springham, T. L. Tan, and P. Lee. Investigation of plume expansion dynamics and estimation of ablation parameters of laser ablated fe plasma. *J. Phys.D : Appl. Phy.*, 42:135504(1–10), 2009.

[204] M. Cirisan, J. M. Jouvard, L. Lavisse, L. Hallo, and R. Oltra. Laser plasma plume structure and dynamics in the ambient air: The early stage of expansion. *J. Appl. Phys.*, 109:103301(1–17), 2011.

[205] S. Yalcin, Y. Y Tsui, and R. Fedosejevs. Images of femtosecond laser plasma plume expansion into background air. *IEEE Transaction on Plasma Science*, 33(2):482–483, 2005.

[206] S. Amoruso, R. Bruzzese, X. Wang, and J. Xia. Propagation of a femtosecond pulsed laser ablation plume into a background atmosphere. *Appl. Phys. Lett.*, 92:041503(1–3), 2008.

[207] T. Donnelly, J. G. Lunney, S. Amoruso, R. Bruzzese, X. Wang, and X. Ni. Dynamics of the plumes produced by ultrafast laser ablation of metals. *J. Appl. Phys.*, 108:043309(1–13), 2010.

[208] S. Canulescu, E. Papadopoulou, D. Anglos, T. Lippert, M. J. Montenegro, S. Georgiou, M. Döbeli, and A.Wokaun. Nanosecond and femtosecond ablation of $La_{0.6}Ca_{0.4}CoO_3$: a comparison between plume dynamics and composition of the films. *Appl. Phys. A*, 105:167–176, 2011.

[209] Z. Wu, X. Zhu, and N. Zhang. Time-resolved shadowgraphic study of femtosecond laser ablation of aluminum under different ambient air pressures. *J. Appl. Phys.*, 109:053113(1–8), 2011.

[210] K. F. Al-Shboul, S. S. Harilal, and A. Hassanein. Spatio-temporal mapping of ablated species in ultrafast laser-produced graphite plasmas. *Appl. Phys. Lett.*, 100:221106(1–4), 2012.

[211] T. Donnelly, J. G. Lunney, S. Amoruso, R. Bruzzese, X. Wang, and X. Ni. Angular distributions of plume components in ultrafast laser ablation of metal targets. *Appl. Phys. A*, 100:569–574, 2010.

[212] R. F. Wood, J. N. Leboeuf, K. R. Chen, D. B. Geohegan, and A. A. Puretzky. Dynamics of plume propagation, splitting, and nanoparticle formation during pulsed-laser ablation. *Appl. Surf. Sci.*, 127129:151–158, 1998.

[213] S. Amoruso, R. Bruzzese, C. Pagano, and X. Wang. Features of plasma plume evolution and material removal efficiency during femtosecond laser ablation of nickel in high vacuum. *Appl. Phys. A*, 89:1017–1024, 2007.

[214] Sir G. Taylor. The Formation of a Blast Wave by a Very Intense Explosion. I. theoretical discussion. In *Proc. R. Soc. London. A*, volume 201, pages 159–174, 1950.

[215] L. I. Sedov. *Similarity and Dimensional Methods in Mechanics*. CRC Press, Boca Raton, 10 edition, 1993.

[216] D. B. Geohegan. Fast intensified ccd photography of $YBa_2Cu_3O_{7-x}$ laser ablation in vacuum and ambient oxygen. *Appl. Phys. Lett.*, 60(22):2732–2734, 1992.

[217] S. S. Harilal, C. V. Bindhu, M. S. Tillack, F. Najmabadi, and A. C. Gaeris. Plume splitting and sharpening in laser-produced aluminium plasma. *J. Phys. D: Appl. Phys.*, 35:2935–2938, 2002.

[218] P. E. Dyer, A. Issa, and P. H. Key. Dynamics of excimer laser ablation of superconductors in an oxygen environment. *Appl. Phys. Lett.*, 57(2): 186–188, 1990.

[219] J. H. Weaver and H. P. R. Frederikse. *CRC Handbook of Chemistry and*

Physics, chapter Optical Properties of Selected Elements. CRC Press, Boca Raton, Florida, 74th and subsequent printings edition, 1999.

[220] V. Berardi, S. Amoruso, N. Spinelli, M. Armenante, R. Velotta, F. Fuso, M. Allegrini, and E. Arimondo. Diagnostics of $YBa_2Cu_3O_{7-\delta}$ laser plume by timeofflight mass spectrometry. *J. Appl. Phys.*, 76(12):8077–8087, 1994.

[221] S. Noël, J. Hermann, and T. Itina. Investigation of nanoparticle generation during femtosecond laser ablation of metals. *Appl. Surf. Sci.*, 253: 6310–6315, 2007.

[222] S. Amoruso, R. Bruzzese, X. Wang, N. N. Nedialkov, and P. A. Atanasov. Femtosecond laser ablation of nickel in vacuum. *J. Phys. D: Appl. Phys.*, 40:331–340, 2007.

[223] A. K. Sharma and R. K. Thareja. Plume dynamics of laser-produced aluminum plasma in ambient nitrogen. *Appl. Surf. Sci.*, 243:68–75, 2005.

[224] N. Zhang, X. Zhua, J. Yang, X. Wang, and M. Wang. Time-resolved shadowgraphs of material ejection in intense femtosecond laser ablation of aluminum. *Phys. Rev. Lett.*, 99:167602(1–4), 2007.

[225] B. C. Stuart, M.D. Feit, S. Herman, A. M. Rubenchik, B. W. Shore, and M. D. Perry. Optical ablation by high-power short-pulse lasers. *J. Opt. Soc. Am. B*, 13(2):459–468, 1996.

[226] D. Breitling, A. Ruf, and F. Dausinger. Fundamental aspects in machining of metals with short and ultrashort laser pulses. In *Photon Processing in Microelectronics and Photonics III, Proc. of SPIE*, volume 5339, pages 49–63, 2004.

[227] K. H. Leitz, B. Redlingshöfer, Y. Reg, A. Otto, and M. Schmidt. Metal

ablation with short and ultrashort laser pulses. *Phys. Procedia*, 12:230–238, 2011.

[228] T. Deshi. Method and apparatus for via drilling and selective material removal using an ultrafast pulse laser, Patent No. : US 7528342B2, May 5, 2009.

[229] J. Konig and T. Bauer. Fundamentals and industrial applications of ultrashort pulsed lasers at bosch. In *Frontiers in Ultrafast Optics: Biomedical, Scientific, and Industrial Applications XI, Proc. of SPIE*, volume 7925, pages 792510(1–6), 2011.

[230] M. E. Fermann, A. Galvanauskas, and G. Sucha, editors. *Ultrafast Lasers: Technology and Applications*. New York:Dekker, 2003.

[231] A. Zoubir, L. Shah, K. Richardson, and M. Richardson. Practical uses of femtosecond laser micro-materials processing. *Appl. Phys. A*, 77:311–315, 2003.

[232] C. S. Nielsen and P. Balling. Deep drilling of metals with ultrashort laser pulses: A two-stage process. *J. Appl. Phys.*, 99:093101(1–4), 2006.

[233] L. Jiao, E. Y. K. Ng, L. M. Wee, and H. Zheng. Parametric study of femtosecond pulses laser hole drilling of silicon wafer. *Adv. Mater. Res.*, 74:273–277, 2009.

[234] G. Kamlage, T. Bauer, A. Ostendorf, and B. N. Chichkov. Deep drilling of metals by femtosecond laser pulses. *Appl. Phys. A*, 77:307–310, 2003.

[235] X. Zhu, D. M. Villeneuve, A. Yu. Naumov, S. Nikumb, and P. B. Corkum. Experimental study of drilling sub-10 μm holes in thin metal foils with femtosecond laser pulses. *Appl. Surf. Sci.*, 152:138–148, 1999.

[236] A. E. Wynne and B. C. Stuart. Rate dependence of short-pulse laser ablation of metals in air and vacuum. *Appl. Phys. A*, 76:373–378, 2003.

[237] S. Döring, S. Richter, A. Tünnermann, and S. Nolte. Evolution of hole depth and shape in ultrashort pulse deep drilling in silicon. *Appl. Phys. A*, 105:69–74, 2011.

[238] S. Döring, S. Richter, S. Nolte, and A. Tünnermann. In situ imaging of hole shape evolution in ultrashort pulse laser drilling. *Opt. Express*, 18 (19):20395–20400, 2010.

[239] S. Döring, S. Richter, A. Tünnermann, and S. Nolte. Influence of pulse duration on the hole formation during short and ultrashort pulse laser deep drilling. In *Frontiers in Ultrafast Optics: Biomedical, Scientific, and Industrial Applications XII, Proc. of SPIE*, volume 8247, pages 824717(1–9), 2012.

[240] A. Luft, U. Franz, A. Emsermann, and J. Kaspar. A study of thermal and mechanical effects on materials induced by pulsed laser drilling. *Appl. Phys. A*, 63:93–101, 1996.

[241] A. Michalowski, D. Walter, F. Dausinger, and T. Graf. Melt dynamics and hole formation during drilling with ultrashort pulses. *J. Laser Micro/Nanoengineering*, 3(3):211–215, 2008.

[242] T. V. Kononenko, S. M. Klimentov, S. V. Garnov, V. I. Konov, D. Breitling, C. Föhl, A. Ruf, J. Radtke, and F. Dausinger. Hole formation process in laser deep drilling with short and ultrashort pulses. In *Second International Symposium on Laser Precision Microfabrication, Proc. of SPIE*, volume 4426, pages 108–112, 2002.

[243] S. Nolte, C. Momma, G. Kamlage, A. Ostendorf, C. Fallnich, F. V. Alvensleben, and H. Welling. Polarization effects in ultrashort-pulse laser drilling. *Appl. Phys. A*, 68:563–567, 1999.

[244] A. Ancona, F. Röser, K. Rademaker, J. Limpert, S. Nolte, and A. Tünnermann. High speed laser drilling of metals using a high repetition rate, high average power ultrafast fiber cpa system. *Opt. Express*, 16(12): 8958–8968, 2008.

[245] J. Dean, P. Forrester, M. Bercx, D. Graper, L. McKinney, F. Frank, M. Nantel, and R. Marjoribanks. Optical coherence and beamspread in ultrafast-laser pulsetrain-burst hole drilling. In *Photonics North 2006, edited by Pierre Mathieu, Proc. of SPIE*, volume 6343, pages 63432A(1–12), 2006.

[246] P. R. Herman, R. Marjoribanks, and A. Oettl. Burst-Ultrafast Laser Machining Method, Patent No. : US 6552301B2, April 22, 2003.

[247] L. Shah, J. Tawney, M. Richardson, and K. Richardson. Femtosecond laser deep drill hole drilling of silicate glasses in air. *Appl. Surf. Sci.*, 183: 151–164, 2001.

[248] X. Zhao and Y. C. Shin. Femtosecond laser drilling of high-aspect ratio microchannels in glass. *Appl. Phys. A*, 104:713–719, 2001.

[249] Wet Chemical Etching and Cleaning of Silicon. Report. *Virginia Semiconductor Inc.*, 2003.

[250] J. Bonse, K. W. Brzezinka, and A. J. Meixner. Modifying single-crystalline silicon by femtosecond laser pulses: an analysis by micro raman spectroscopy, scanning laser microscopy and atomic force microscopy. *Appl. Surf. Sci.*, 221:215–230, 2004.

[251] D. J. Hwang, C. P. Grigoropoulos, and T. Y. Choi. Efficiency of silicon micromachining by femtosecond laser pulses in ambient air. *J. Appl. Phys.*, 99:083101(1–6), 2006.

[252] P. S. Banks, M. D. Fiet, A. M. Rubenchik, B. C. Stuart, and M. D. Perry. Material effects in ultra-short pulse laser drilling of metals. *Appl. Phys. A*, 69(suppl.):S377–S380, 1999.

[253] A. Ruf, P. Berger, F. Dausinger, and H. Hügel. Analytical investigations on geometrical influences on laser drilling. *J. Phys. D: Appl. Phys.*, 34: 2918–2915, 2001.

[254] S. Nolte, C. Momma, H. Jacobs, A. Tünnermann, B. N. Chichkov, B. Wellegehausen, and H. Welling. Ablation of metals by ultrashort laser pulses. *J. Opt. Soc. Am. B*, 14(10):2716–2722, 1997.

[255] S. Lee, D. Yang, and S. Nikumb. Femtosecond laser micromilling of si wafers. *Appl. Surf. Sci.*, 254:2996–3005, 2008.

[256] D. P. Korfiatis, K. A. Th. Thoma, and J. C. Vardaxoglou. Numerical modeling of ultrashort-pulse laser ablation of silicon. *Appl. Surf. Sci.*, 255:7605–7609, 2009.

[257] K. Sokolowski-Tinten and D. von der Linde. Generation of dense electron-hole plasmas in silicon. *Phys. Rev. B*, 61(4):2643–2650, 2000.

[258] Robert Fedosejevs, Ying Tsui, Zhijiang Chen, and Shyama Banerjee. *Nanofabrication*, chapter Laser Nanopatterning, pages 301–319. Springer-Verlag/Wien, 2012.

[259] P. P. Pronko, S. K. Dutta, J. Squier, J. V. Rudd, D. Du, and G. Mourou. Machining of sub-micron holes using a femtosecond laser at 800 nm. *Opt. Commun.*, 114:106–110, 1995.

[260] F. Korte, J. Serbin, J. Koch, A. Egbert, C. Fallnich, A. Ostendorf, and B. N. Chichkov. Towards nanostructuring with femtosecond laser pulses. *Appl. Phys. A*, 77:229–235, 2003.

[261] Jan-Hendrik Klein-Wiele and Peter Simon. Sub-100nm pattern generation by laser direct writing using a confinement layer. *Opt. Exp.*, 21(7): 9017–9023, 2013.

[262] Andrey A Ionin, Sergey I Kudryashov, Sergey V Makarov, Leonid V Seleznev, Dmitry V Sinitsyn, Alexander E Ligachev, Evgene V Golosov, and Yury R Kolobov. Sub-100 nanometer transverse gratings written by femtosecond laser pulses on a titanium surface. *Laser Phys. Lett.*, 10: 056004(1–5), 2013.

[263] V. Zorba, X. Mao, and R. E. Russo. Laser wavelength effects in ultrafast near-field laser nanostructuring of si. *Appl. Phys. Lett.*, 95:041110(1–3), 2009.

[264] M. P. Mateo, V. Pi non, D. Anglos, and G. Nicolas. Effect of ambient conditions on ultraviolet femtosecond pulse laser induced breakdown spectra. *Spectrochimica Acta Part B*, 74-75:18–23, 2012.

[265] A. Nakimana, H. Tao, X. Gao, Z. Hao, and J. Lin. Effects of ambient conditions on femtosecond laser-induced breakdown spectroscopy of Al. *J. Phys. D: Appl. Phys.*, 46:285204(1–6), 2013.

[266] V. N. Rai, J. P. Singh, F. Y. Yueh, and R. L. Cook. Study of optical emission from laser-produced plasma expanding across an external magnetic field. *Laser Part. Beams*, 21(1):65–71, 2003.

[267] X. K. Shen, Y. F. Lu, T. Gebre, H. Ling, and Y. X. Han. Optical emission in magnetically confined laser-induced breakdown spectroscopy. *J. Appl. Phys.*, 100:053303(1–7), 2006.

[268] H. Y. Zheng and Z. W. Jiang. Femtosecond laser micromachining of silicon with an external electric field. *J. Micromech. Microeng.*, 20:017001(1–4), 2010.

[269] V. N. Rai, A. K. Rai, F. Y. Yueh, and J. P. Singh. Optical emission from laser-induced breakdown plasma of solid and liquid samples in the presence of a magnetic field. *Appl. Opt.*, 42(12):2085–2093, 2003.

[270] S. Q. Wang, S. Suthar, C. Hoeflich, and B. J. Burrow. Diffusion barrier properties of TiW between si and cu. *J. Appl. Phys.*, 73:2301–2320, 1993.

[271] R. Ramis. Hydrodynamic analysis of laser-driven cylindrical implosions. *Phys. Plasmas*, 20:082705(1–14), 2013.